Flow and Solute Transport in Random Cylinder Arrays: a Model for Emergent Aquatic Plant Canopies

by

Yukie Tanino

Submitted to the Department of Civil and Environmental Engineering
in partial fulfillment of the requirements for the degree of

Doctor of Philosophy in Environmental Fluid Mechanics

at the

MASSACHUSETTS INSTITUTE OF TECHNOLOGY

September 2008

Author .....
Department of Civil and Environmental Engineering
August 11, 2008

Certified by .....
Heidi M. Nepf
Professor of Environmental Fluid Mechanics
Thesis Supervisor

Accepted by .....
Daniele Veneziano
Chairman, Departmental Committee for Graduate Students

Flow and Solute Transport in Random Cylinder Arrays: a Model for Emergent Aquatic Plant Canopies

by

Yukie Tanino

Submitted to the Department of Civil and Environmental Engineering
on August 11, 2008, in partial fulfillment of the
requirements for the degree of
Doctor of Philosophy in Environmental Fluid Mechanics

Abstract

With wetlands constituting about 6% of earth's land surface, aquatic vegetation plays a significant role in defining mean flow patterns and in the transport of dissolved and particulate material in the environment. However, the dependence of the hydrodynamic and transport processes on fundamental properties of an aquatic plant canopy has not been investigated systematically over the wide range of conditions that are observed in the field. A laboratory investigation was conducted to describe flow and solute transport in idealized emergent plant canopies. This thesis presents laboratory measurements of the mean drag, turbulence structure and intensity, and lateral dispersion of passive solute in arrays of randomly-distributed cylinders, a model for emergent, rigid aquatic plants.

Mean drag per cylinder length normalized by the mean interstitial fluid velocity and viscosity increases linearly with cylinder Reynolds number. In contrast to the dependence previously reported for sparse arrays at Reynolds numbers greater than 1000, the drag coefficient increases with increasing cylinder density in intermediate and high cylinder densities.

In dense arrays, turbulent eddies are constrained by the interstitial pore size such that the integral length scale is equal to the mean surface-to-surface distance between a cylinder in the array and its nearest neighbor. The classic scale model for mean turbulence intensity, which is a function of the inertial contribution to the drag coefficient, the solid volume fraction, and the integral length scale of turbulence normalized by d, is then confirmed with our laboratory measurements.

Our laboratory experiments demonstrate that $K_{yy}/(\langle\overline{u}\rangle d)$, the asymptotic (Fickian) lateral dispersion coefficient normalized by the mean interstitial fluid velocity, $\langle\overline{u}\rangle$, and d, is independent of Reynolds number at sufficiently high Reynolds number. Although previous models predict that asymptotic lateral dispersion increases monotonically with cylinder density, laboratory measurements reveal that lateral dispersion at high Reynolds number exhibits three distinct regimes. In particular, an intermediate regime in which $K_{yy}/(\langle\overline{u}\rangle d)$ decreases with increasing cylinder density is observed. A scale model for turbulent diffusion is developed with the assumption that

only turbulent eddies with integral length scale greater than d contribute significantly to net lateral dispersion. The observed dependence of asymptotic dispersion on cylinder density is accurately described by a linear superposition of this turbulent diffusion model and existing models for dispersion due to the spatially-heterogeneous velocity field that arises from the presence of the cylinders. Finally, laboratory measurements support the conjecture that $K_{yy}/(\langle\overline{u}\rangle d)$ is not strongly dependent on Reynolds number in dense arrays at any Re_d. However, the distance required to achieve asymptotic dispersion is shown to depend strongly on the Reynolds number.

Thesis Supervisor: Heidi M. Nepf
Title: Professor of Environmental Fluid Mechanics

Acknowledgments

First and foremost, I would like to thank my thesis supervisor and academic advisor, Heidi M. Nepf, for her time, guidance, and support. Heidi's ability to accommodate students with very different personalities and research styles has truly been remarkable. I would also like to thank the other two members of my thesis committee, Eric Adams and Roman Stocker, for their insights and advice.

I would like to thank the environmental fluid mechanics graduate students for their questions, comments, and feedback. In particular, Brian White and Anne Lightbody provided valuable insights from both their research and their job search experience. Brian also provided unpublished ADV measurements from his Master's thesis (White, 2002). The efforts of Aaron Chow in troubleshooting the lasers that were used in my LIF experiments were invaluable. David Gonzalez-Rodriguez contributed the approach employed in the theoretical analysis of the nearest-neighbor separation of randomly-distributed cylinders presented in Appendix D.

Two undergraduate students, Lucy L. Wu and Sheung Yan Sueann Lee, collected some of the laboratory measurements of cylinder drag in Chapter 2.

Finally, I am grateful to Andy Gallant at the MIT Central Machine Shop who, in addition to coordinating the construction of the flume used in my LIF experiments, kindly offered technical assistance many times throughout my graduate research.

This thesis is based on work supported by the National Science Foundation grants EAR-0509658, EAR-6895392, and EAR-0309188. Any opinions, conclusions, or recommendations expressed in this material are those of the author and do not necessarily reflect the views of the National Science Foundation. In addition, I was supported by the Martin Family Society Fellowship for Sustainability in the spring of 2007.

Contents

List of Figures

List of Tables

Chapter 1

Introduction

Vegetation in aquatic flows alters its environment in many ways. Most importantly, plants introduce additional hydraulic resistance to the flow, which may significantly reduce the volumetric flow rate in channels. Vegetation also influences the transport of dissolved and particulate material, such as nutrients, pollutants, and sediment, by creating velocity heterogeneity at the scale of individual stems. For example, plants force fluid to follow tortuous paths around them (figure 1-1) and introduce no-slip boundaries and spatial variations in the local interstitial cross-sectional area (because spacing between plants is not uniform) (e.g., Fried and Combarnous, 1971). Under certain conditions, recirculation zones may develop immediately downstream of plants. These small-scale heterogeneities in local velocity contribute to longitudinal and transverse dispersion. In addition, the presence of plants alters the turbulence structure and intensity. This in turn alters the instantaneous thickness of the boundary layer at the surface of plants and organisms in the water and, in the absence of other rate-limiting steps, presumably affects the diffusive flux of nutrients across the boundary layer and their removal from the water. Also, suspended sediment transport is reduced in channels with submerged vegetation because of the reduction in bed shear stress (López and García, 1998). Similarly, treatment wetlands have been observed to reduce the total suspended solid concentration by as much as 90% (Knight et al., 1999), demonstrating that vegetation can create conditions favorable to particle removal.

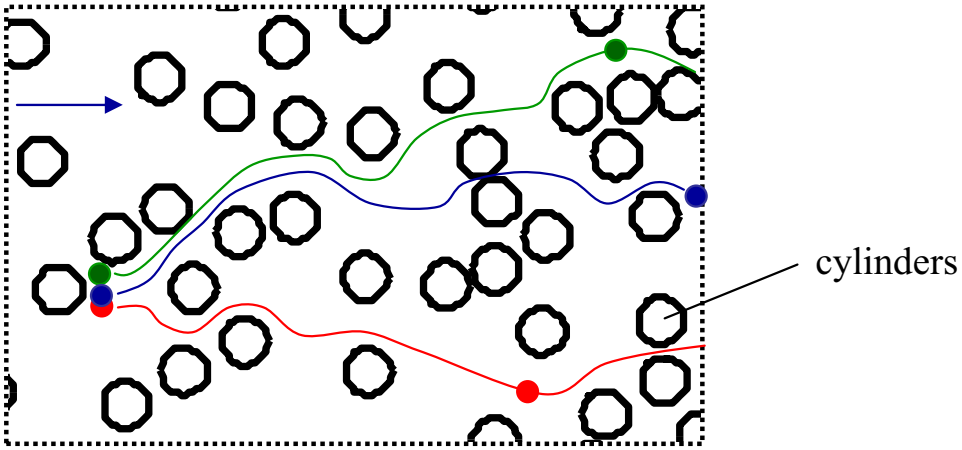

Figure 1-1: Flow in an array of randomly distributed cylinders, a model for emergent plants. Fluid is forced to flow around the impermeable cylinders, such that fluid particles that are close to one another at some instance may be separated laterally after some period of time. Mean flow is from left to right.

Field conditions in aquatic plant canopies span a wide range. For example, even within emergent plant canopies, i.e., canopies where plants span the entire water column and penetrate the free surface, the fraction of the total (plants and fluid) volume occupied by plants may be as small as $\phi = 0.1 - 2\%$ (Valiela et al., 1978; Leonard and Luther, 1995, salt marshes) or as high as 50% (Mazda et al., 1997, mangroves). In the former, flow around each stem in the canopy resembles flow past an isolated stem. The latter approaches the limit of packed beds of spheres ($\phi \approx 0.6 - 0.7$). Similarly, mean flow velocity varies from 0 to $O(10)$ cm s^{-1}, which spans the steady laminar, unsteady laminar, and turbulent flow regimes in the presence of cylindrical plants. In contrast, solid volume fraction and flow conditions in most other types of obstructed flows, e.g., groundwater and flow through packed beds of spheres, trees, buildings, and filters, do not vary significantly within each context. Consequently, previous studies in the literature have generally focused on a narrow parameter range. In this thesis, I describe the dependence of drag, turbulence, and solute transport on two key properties of an emergent plant canopy, plant density (ϕ) and Reynolds number, over the entire range of conditions relevant to emergent plant canopies.

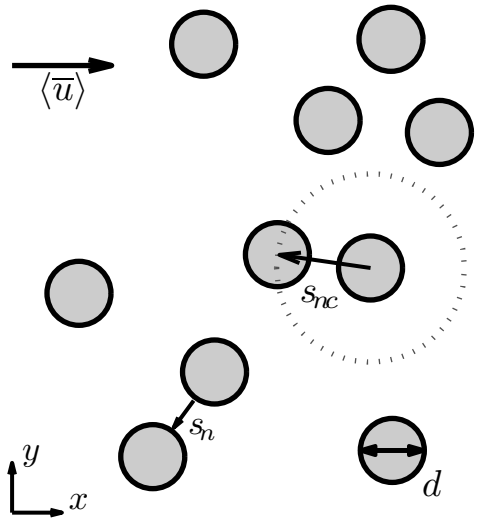

Figure 1-2: Key parameters for a two-dimensional array of randomly-distributed cylinders of uniform diameter d. The center-to-center distance to the nearest neighbor, s_{nc}, differs for each cylinder.

1.1 Key parameters in a random cylinder array

In this thesis, a plant canopy is modeled as a homogeneous, two-dimensional array of rigid, circular cylinders of uniform diameter d distributed randomly with a constant density m (cylinders per unit horizontal area). The corresponding solid volume fraction is $\phi = m\pi d^2/4$. The center-to-center distance from a particular cylinder to its nearest neighbor is denoted by s_{nc}, as illustrated in figure 1-2 for an arbitrary cylinder. The corresponding surface-to-surface distance is denoted by s_n $(= s_{nc} - d)$. The mean nearest-neighbor separation defined between cylinder surfaces, $\langle s_n \rangle_A$, where $\langle\ \ \rangle_A$ denotes an average over many cylinders in the array, can be described analytically as a function of ϕ and d (Appendix D). Note that our formulation is only valid where the large-scale dimensions of the array, e.g., water depth and array width, are much larger than d and $\langle s_n \rangle_A$.

The Cartesian coordinates $\boldsymbol{x} = (x, y, z) = (x_1, x_2, x_3)$ are defined such that the x-axis is aligned with the the mean interstitial fluid velocity $\langle \overline{u} \rangle$ (the fluid velocity averaged over time and the fluid volume). The y-axis is in the horizontal plane and perpendicular to the x-axis (figure 1-2). The z-axis is vertical and aligned with the cylinder axes, which are perpendicular to the horizontal bed of the test section. $z = 0$

is defined at the bed. In this thesis, the overbar denotes an average over a time interval much longer than those associated with turbulent fluctuations and vortex shedding. $\langle\ \rangle$ denotes an average over infinitesimally thin fluid volume that span many cylinders or, equivalently, an ensemble average, i.e., an average over many arrays with the same ϕ, d, and flow conditions, but with different cylinder configurations. In this thesis, we only consider constant, uniform mean flow, i.e., time-independent $\langle\overline{u}\rangle$.

1.1.1 Reynolds number

The two length scales identified above can be used to define two Reynolds numbers, $Re_d \equiv \langle\overline{u}\rangle d/\nu$ and $Re_{\langle s_n\rangle_A} \equiv \langle\overline{u}\rangle\langle s_n\rangle_A/\nu$, where ν is the kinematic viscosity. It is well-established that flow patterns around isolated cylinders are similar at the same Re_d. Detailed descriptions of these flows are available in classic papers and in standard fluid mechanics text books, e.g., Lienhard, 1966; Kundu and Cohen, 2004; Gerrard, 1978, so only the key regimes relevant to this chapter are identified here. As Re_d is increased from Stokes flow, flow remains steady and laminar everywhere in the fluid up to $Re_d \approx 40$. At $Re_d \approx 40$, the isolated cylinder wake begins to oscillate periodically. At $Re_d \approx 90$, vortices begin to periodically shed from the cylinder. This unsteady, laminar wake regime continues until $Re_d \approx 200$, beyond which the periodic motion of the wake gradually breaks down and the wake becomes turbulent as Re_d is increased further. The wake becomes fully turbulent at roughly $Re_d \approx 5000$ (Kundu and Cohen, 2004).

At sufficiently small ϕ, flow around each cylinder in the array resembles flow past an isolated cylinder. In this limit, where $\langle s_n\rangle_A$ tends to infinity, Re_d is the relevant Reynolds number and, for example, transitions between the flow regimes described above occur at the same Re_d as in the isolated cylinder wake. At sufficiently large ϕ, the array resembles a network of intersecting channels of width $\langle s_n\rangle_A$. Accordingly, flow in such arrays is expected to be kinematically and dynamically similar at the same $Re_{\langle s_n\rangle_A}$. Arrays considered in this thesis appear to fall between these limits, and neither Re_d or $Re_{\langle s_n\rangle_A}$ alone captures the similarity across flows at different ϕ (§ 4.3.1). For simplicity, results will be discussed in terms of Re_d only. It should be

noted that in the laboratory experiments reported in this thesis, d was kept constant, and differences in Re_d result entirely from differences in $\langle\overline{u}\rangle/\nu$, i.e., Re_d dependence refers specifically to the dependence on $\langle\overline{u}\rangle/\nu$.

However, certain empirical criteria used in Ch. 3 are more conveniently defined in terms of $Re_{\langle s_n\rangle_A}$. Specifically, it will be shown that the lateral variance of a time-averaged solute plume becomes Re_d-independent above a critical Re_d that is, in general, larger at larger ϕ (Appendix A). For convenience, we prefer to use a single criterion for all ϕ to identify the Re_d-independent variance measurements. Since $\langle s_n\rangle_A$ decreases with increasing ϕ, more of our measurements can be correctly classified as Re_d-independent by a single value of $Re_{\langle s_n\rangle_A}$ than a single value of Re_d and, accordingly, the latter is used to define the empirical criterion for Re_d-independent time-averaged concentration variance.

1.2 Thesis structure

Chapter 2 presents laboratory measurements of cross-sectionally averaged cylinder drag and its dependence on Re_d and ϕ. It is shown that drag per unit cylinder length, when normalized by $\langle\overline{u}\rangle$ and viscosity, increases linearly with Re_d, consistent with the classic dimensional analysis of form/inertial drag of an isolated cylinder. A single linear function (of Re_d) is computed for each ϕ, from which the normalized drag can be predicted. The material in this chapter has been published as Tanino and Nepf, 2008b.

Chapter 3 presents scale models and laboratory measurements of (i) the integral length scale of turbulence, (ii) the mean turbulence intensity, and (iii) the asymptotic (long-time/long-distance) lateral dispersion coefficient, K_{yy}, normalized by $\langle\overline{u}\rangle d$ at high Re_d, where the three properties are found to be independent of Re_d. The material in this chapter has been published as Tanino and Nepf, 2008c.

The model for lateral dispersion predicts that $K_{yy}/(\langle\overline{u}\rangle d)$ emerges entirely from the spatially-heterogeneous velocity field *in dense arrays*. At high ϕ, the spatially-averaged velocity field is not expected to depend strongly on Re_d, so the model

predictions imply that lateral dispersion will also not depend strongly on Re_d. The same argument has been made, but not verified, for packed beds of spheres (Hill et al., 2001; Mickley et al., 1965). Chapter 4 presents laboratory measurements of lateral dispersion at transitional Re_d, i.e., below fully turbulent conditions, to test this conjecture. The material in this chapter has been submitted to *Physics of Fluids* as Tanino and Nepf, 2008a.

For the reader's convenience, all figures, equations, and tables are referred to by the corresponding chapter, figure, equation, and table numbers as they appear in this thesis.

Chapter 2

Cross-sectionally-averaged drag in a random array of rigid cylinders[a]

Abstract

This chapter investigates the drag exerted by randomly distributed, rigid, emergent circular cylinders of uniform diameter d. Laboratory measurements are presented for solid volume fraction $\phi = 0.091$, 0.15, 0.20, 0.27, and 0.35 and cylinder Reynolds number $Re_d = 25$ to 690. These ranges coincide with conditions in aquatic plant canopies. The temporally- and cross-sectionally-averaged drag coefficient, C_D, decreased with increasing Re_d and increased with increasing ϕ under the flow conditions investigated. The dimensionless ratio of the mean drag per unit cylinder length, $\left\langle \overline{f_D} \right\rangle_H$, to the product of the viscosity, μ, and the mean pore velocity, U_p, exhibits a linear Re_d dependence of the form $\left\langle \overline{f_D} \right\rangle_H / (\mu U_p) = \alpha_0 + \alpha_1 Re_d$, consistent with Ergun (1952)'s formulation for packed columns. In the range of experimental conditions, α_1 increases monotonically with ϕ. In contrast, α_0 is constant within uncertainty for $0.15 \leq \phi \leq 0.35$, which suggests that viscous drag per unit cylinder length is independent of ϕ in this range.

[a]This chapter is Tanino and Nepf, 2008b with minor corrections and modifications. The authors also thank the three anonymous reviewers and the associate editor for their comments on the manuscript. This material is based on work supported by the National Science Foundation grants EAR-0509658 and EAR-6895392. Any opinions, conclusions, or recommendations expressed in this material are those of the authors and do not necessarily reflect the views of the National Science Foundation. The authors thank undergraduate students Lucy L. Wu and Sheung Yan Sueann Lee for their assistance with the experiments and Brian L. White for providing unpublished ADV measurements from his Master's thesis (White, 2002).

2.1 Introduction

In the field, the impact of vegetation is largely determined by the additional drag it provides, which can be characterized by a temporally- and spatially-averaged drag coefficient. The drag coefficient is defined here for an array of cylinders of diameter d as

$$C_D \equiv \frac{\left\langle \overline{f_D} \right\rangle}{\rho \left\langle \overline{u} \right\rangle^2 d/2}, \tag{2.1}$$

where $\left\langle \overline{f_D} \right\rangle$ is the average drag in the direction of the average flow per unit length of stem and ρ is the fluid density. In addition to describing the mean drag exerted by the cylinders, C_D is also required in models for turbulence intensity (Nepf, 1999) and longitudinal dispersion (White and Nepf, 2003) in random cylinder arrays.

The drag coefficient of an isolated cylinder is well established. In particular, C_D decreases with increasing Reynolds number up to $Re_d = O(10^3)$. C_D is also influenced by the presence and relative position of neighboring cylinders. For example, a cylinder in the wake of an upstream cylinder experiences a velocity deficit relative to $\langle \overline{u} \rangle$. Consequently, the downstream cylinder experiences a reduced drag (Blevins, 2005; Zdravkovich and Pridden, 1977; Petryk, 1969). Petryk (1969) investigated the influence of a neighboring cylinder on the drag measured at a test cylinder. His data show that, when the cylinders are sufficiently close, the mean drag on the pair of cylinders could be either smaller or greater than that for an isolated cylinder depending on the orientation of the cylinders. In a random array, both the distance between and the relative orientation of each cylinder and its neighbors differ for each cylinder, and it is not obvious whether the array-averaged C_D, as defined by Eq. (2.1), is enhanced or reduced relative to an isolated cylinder.

C_D in a random cylinder array is expected to be a function of ϕ, d, and Re_d. The present chapter considers only the Re_d and ϕ dependence. In salt marshes, stem diameters of 0.2 to 1.2 cm, $\phi = 0.001$ to 0.02, and local flow speeds of the range 0 to 10 cm s^{-1} have been reported (Valiela et al., 1978; Leonard and Luther, 1995). In contrast, ϕ as high as 0.45 and mean trunk diameters of 4 to 9 cm have been reported in mangroves (Mazda et al., 1997; Furukawa et al., 1997). Local flow speeds of the

Source	Array	Configuration	ϕ	Reynolds number
Ayaz and Pedley, 1999	rigid cylinders (N)	square	0.13 0.35 0.50 0.59	$\leq 40.00/(1-\phi)$
Koch and Ladd, 1997	rigid cylinders (N)	random	0.05 0.10 0.20 0.40	≤ 37 ≤ 33 ≤ 100 ≤ 67
		square, staggered	0.2 0.4	$57-210$ $82-320$
Lee et al., 2004	sawgrass (L; F)	N/A	N/A	$0-200$ (L) $70-10^4$ [a] (F)
Mazda et al., 1997	two tidal mangrove swamps (F)	N/A	$0.05-0.45$ [c]	N/A
Nepf, 1999	rigid cylinders (L)	random	0.006 0.02 0.06	$4000-10000$
Petryk, 1969	rigid cylinders (L)	random	0.015 0.027	$(0.6-5)\times 10^4$ $(3-9)\times 10^4$
Stone and Shen, 2002	rigid cylinders (L)	staggered	0.0055 0.0220 0.0610	$O(250-8000)$ assuming $\nu = 0.009$ cm^2 s^{-1}
Wu et al., 1999	flexible horsehair mattress (L)	N/A	N/A	20 - 3000[b]

Table 2.1: Summary of studies that collected drag data in emergent arrays. In the second and fifth columns, (N), (F), and (L) indicate numerical, field, and laboratory results, respectively. N/A denotes information not available or not applicable. Cylinders are circular. Reynolds numbers are based on the cylinder diameter d and U_p unless otherwise noted. The Reynolds number for Lee et al. (2004)'s measurements is defined using the depth-average of the spatially-averaged width of all stems and leaves as the length scale.

[a] Based on depth.
[b] Based on depth and $U_p(1-\phi)$.
[c] Depth dependent.

range 0 to 5 cm s^{-1} have been observed 15 m (Kobashi and Mazda, 2005) and 120 m (Mazda et al., 1997) from the interface between the mangrove and a river. Finally, constructed wetlands may be as dense as $\phi = 0.65$ (Serra et al., 2004). These values suggest that field conditions span $Re_d = 0$ to $O(4000)$ and $\phi = 0$ to 0.65.

Although many recent studies have investigated drag in real and model canopies (see Table 2.1 for examples), a comprehensive data set is not yet available for the entire range of conditions expected in emergent aquatic plant canopies. Specifically, for the simple two-dimensional array of randomly-distributed cylinders, data are not available at $\phi > 0.05$ at $Re_d > 100$ or at $\phi < 0.05$ at $Re_d < 1000$. Moreover, previous studies have reported contradictory ϕ dependence for C_D. Nepf (1999)'s numerical model, which considers two-cylinder interactions in a random array, predicts a monotonically decreasing C_D with increasing ϕ for $8 \times 10^{-4} < \phi < 0.24$ (Nepf, 1999, figure 6). Nepf (1999) verified this model with laboratory measurements at $Re_d \geq 1000$. Similarly, Lee et al. (2004, Eq. (18)) proposed that the depth-averaged C_D is inversely proportional to the depth-averaged frontal area per unit volume and characteristic spacing of all stems and leaves. However, these dependence were not explicitly investigated in that paper. In contrast, C_D increases with ϕ for $Re_d \leq O(100)$ in Koch and Ladd (1997)'s numerical simulations of random arrays for $\phi = 0.05$ to 0.4.

This chapter presents laboratory measurements of the depth-averaged C_D in random arrays of rigid emergent cylinders of $\phi = 0.091$ to 0.35 and $Re_d = 25$ to 685, where Re_d was calculated using the mean pore velocity, U_p, which is the cross-sectional average of $\langle \overline{u} \rangle$. The Re_d dependence of the depth-averaged $\left\langle \overline{f_D} \right\rangle$ is compared with Ergun (1952)'s equation, and the coefficients in that equation are determined for each ϕ. The results are compared with Koch and Ladd (1997)'s numerical simulations and Petryk (1969)'s laboratory measurements.

2.2 Theory

Following the standard formulation in terrestrial canopy literature, e.g., Finnigan, 2000, the pressure $p(\boldsymbol{x}, t)$ and velocity $\boldsymbol{v}(\boldsymbol{x}, t) \equiv (u, v, w) \equiv (v_1, v_2, v_3)$ are first de-

composed into the local time average $(\overline{v_i}, \overline{p})$ and instantaneous deviations from it (v_i', p'), where $\overline{v_i'}, \overline{p'} = 0$. Then, the temporally-averaged quantities are further decomposed into their spatial average $(\langle \overline{v_i} \rangle, \langle \overline{p} \rangle)$ and deviations from that average $(\overline{v_i}'', \overline{p}'')$, where $\langle \overline{v_i}'' \rangle, \langle \overline{p}'' \rangle = 0$. The overbar denotes a temporal average over an interval much longer than the time scales of vortex shedding and turbulent fluctuations and $\langle\ \rangle$ denotes a spatial average over an infinitessimally thin volume V_f that spans many cylinders but excludes all solid volume (see, e.g., Finnigan, 1985, 2000). Recall that the array is homogeneous. The water depth $H(\boldsymbol{x}, t)$ is also decomposed analogously. $\left\langle \overline{H} \right\rangle \gg \left| \overline{H}'' \right|, |H'|$ in systems considered in this chapter. Applying the same temporal and spatial averaging operations to the governing equations yields $(i, j = 1, 2, 3)$

$$\frac{\partial \langle \overline{v_i} \rangle}{\partial t} + \langle \overline{v_j} \rangle \frac{\partial \langle \overline{v_i} \rangle}{\partial x_j} = g_i - \frac{1}{\rho} \frac{\partial \langle \overline{p} \rangle}{\partial x_i} - \frac{\partial \left\langle \overline{v_i' v_j'} \right\rangle}{\partial x_j} + \nu \frac{\partial}{\partial x_j} \frac{\partial \langle \overline{v_i} \rangle}{\partial x_j} - \frac{\partial \langle \overline{v_i}'' \overline{v_j}'' \rangle}{\partial x_j} - f_i, \quad (2.2)$$

where g_i is the i^{th} component of the gravitational acceleration and

$$f_i = -\frac{\nu}{V_f} \iint_{S_c} \frac{\partial \overline{v_i}}{\partial n} \, \mathrm{d}S + \frac{1}{\rho V_f} \iint_{S_c} \overline{p} n_i \, \mathrm{d}S \quad (2.3)$$

is the net hydrodynamic force per unit fluid mass exerted on S_c, where S_c denotes all cylinder surfaces that intersect V_f and $\boldsymbol{n}$ is the unit normal vector on S_c pointing out of V_f. f_1 represents the net cylinder drag per unit fluid mass from which $\left\langle \overline{f_D} \right\rangle$ in Eq. (2.1) can be calculated: $\left\langle \overline{f_D} \right\rangle = \rho(1 - \phi) f_1 / m$. Recall that m is the cylinder density in the array (cylinders per unit horizontal area). The third and fifth terms on the RHS of Eq. (2.2) are the divergence of the spatially-averaged Reynolds stress and the dispersive stress, respectively. The latter arises from spatial correlations of the local deviations from the temporally- and spatially-averaged velocity.

The first term in Eq. (2.3) describes the viscous contribution that arises from the viscous shear stress on the cylinder surface. If we scale $-\partial \overline{u} / \partial n$ as $\langle \overline{u} \rangle / \langle s_n \rangle_A$, the corresponding viscous contribution to $\left\langle \overline{f_D} \right\rangle$ scales as

$$\frac{\langle \overline{f_D} \rangle^{\text{visc}}}{\mu \langle \overline{u} \rangle} \sim \pi \frac{d}{\langle s_n \rangle_A}. \quad (2.4)$$

The second term in Eq. (2.3) describes the inertial contribution arising from the pressure loss in the cylinder wake. Dimensional analysis yields, for the corresponding inertial contribution to $\left\langle \overline{f_D} \right\rangle$, $\left\langle \overline{f_D} \right\rangle^{\text{form}} = \rho d \langle \overline{u}''^2 \rangle \; f(Re_d)$, where $f(Re_d)$ is an unknown function of Re_d. In dimensionless form,

$$\frac{\left\langle \overline{f_D} \right\rangle^{\text{form}}}{\mu \langle \overline{u} \rangle} = \frac{\langle \overline{u}''^2 \rangle}{\langle \overline{u} \rangle^2} f(Re_d) \; Re_d. \tag{2.5}$$

Ergun (1952) proposed an expression for pressure drop in packed columns which, when rearranged, yields the dimensionless drag parameter

$$\frac{\left\langle \overline{f_D} \right\rangle}{\mu \left\langle \overline{u} \right\rangle} = \alpha_0 + \alpha_1 Re_d, \tag{2.6}$$

where μ is the viscosity, α_0 is a function of ϕ, and α_1 is a constant. Recently, Koch and Ladd (1997) demonstrated for arrays of $\phi = 0.05$ to 0.4 that cylinder drag may also be described by a linear Re_d dependence of the same form as Eq. (2.6), but with both α_0 and α_1 varying with ϕ. By comparing Eq. (2.6) with Eqs. (2.4) and (2.5), it can be seen that α_0 and $\alpha_1 Re_d$ correspond to the viscous and inertial contributions to $\left\langle \overline{f_D} \right\rangle / (\mu \langle \overline{u} \rangle)$, respectively. Substituting Eq. (2.6) into Eq. (2.1) yields the corresponding relationship for C_D:

$$C_D = 2 \left(\frac{\alpha_0}{Re_d} + \alpha_1 \right). \tag{2.7}$$

Also, C_D of a smooth isolated cylinder is described by the empirical expression (White, 1991, p.183),

$$C_D \approx 1 + 10.0 {Re_d}^{-2/3}, \qquad 1 < Re_d < 10^5, \tag{2.8}$$

which corresponds to [from Eq. (2.1)]

$$\frac{\left\langle \overline{f_D} \right\rangle}{\mu \left\langle \overline{u} \right\rangle} \approx 5.00 {Re_d}^{1/3} + \frac{1}{2} Re_d, \qquad 1 < Re_d < 10^5. \tag{2.9}$$

As Re_d increases, the second term becomes increasingly large relative to the first term

and Eq. (2.9) approaches a linear Re_d dependence of the form Eq. (2.6).

In the present laboratory conditions and under certain field conditions, Eq. (2.2) can be simplified. Here, we consider a two dimensional, homogeneous array and assume $\langle \overline{v} \rangle = 0$ and $\partial \langle \ \rangle / \partial y = 0$. Accordingly, the depth average is equivalent to a cross-sectional average. The flow is also steady, $\partial / \partial t = 0$. In the cases analyzed here, the free surface gradient ranged in magnitude from 4×10^{-4} to 5×10^{-2}, indicating that the vertical length scale $\left\langle \overline{H} \right\rangle$ was significantly smaller than the horizontal length scale $\left\langle \overline{H} \right\rangle / (d \left\langle \overline{H} \right\rangle / dx)$. Under these conditions, Eq. (2.2) reduces to

$$\langle \overline{u} \rangle \frac{\partial \langle \overline{u} \rangle}{\partial x} + \langle \overline{w} \rangle \frac{\partial \langle \overline{u} \rangle}{\partial z} = -\frac{1}{\rho} \frac{\partial \langle \overline{p} \rangle}{\partial x} - \left(\frac{\partial \left\langle \overline{u'u'} \right\rangle}{\partial x} + \frac{\partial \left\langle \overline{u'w'} \right\rangle}{\partial z} \right) + \nu \frac{\partial^2 \langle \overline{u} \rangle}{\partial z^2} - \left(\frac{\partial \langle \overline{u}'' \overline{u}'' \rangle}{\partial x} + \frac{\partial \langle \overline{u}'' \overline{w}'' \rangle}{\partial z} \right) - f_1 \tag{2.10}$$

in the x-direction. Recall that the bed is horizontal, i.e., $g_1 = g_2 = 0$ and $g_3 = -g$. We also assume that the $i = 3$ component of Eq. (2.2) reduces to the hydrostatic pressure balance. White (2002) measured velocity in random arrays of $\phi = 0.010 - 0.063$. From his measurements closest to the bed, where $\overline{w'w'}$ varied most rapidly with depth, $\overline{w'^2}/z$ ranged from 0.007 to 6.5 cm s^{-2} ($\ll |g_3|$). These data support the hydrostatic pressure assumption. $\overline{u}''$ is expected to vary on the scale of the cylinder spacing and $\overline{w}''$ on the scale of the water depth and, consequently, correlations between time-averaged spatial deviations are expected to be negligible, i.e., $\langle \overline{u}'' \overline{w}'' \rangle \ll \left\langle \overline{u'w'} \right\rangle$ (Kaimal and Finnigan, 1994, p. 85). This was verified experimentally for submerged periodic arrays at $\phi = 0.0008$ to 0.013 (Poggi et al., 2004). In addition, Tsujimoto et al. (1992) measured zero $\overline{u'w'}$ over the entire water column in an emergent periodic array of $\phi = 0.0044$ and 0.0079. Following the above discussion, the third and the sixth terms on the RHS of Eq. (2.10) are neglected.

Next, Eq. (2.10) is averaged over the water depth. Free surface stress is negligible in the laboratory. Bed shear stress estimated from White (2002)'s measurements in a random array of $\phi = 0.010 - 0.063$ is 0.2 to 13% of the cylinder drag contribution estimated from the isolated cylinder solution (2.9). Moreover, the drag contribution from the cylinders is expected to become more dominant as ϕ increases. It should be noted that bed and free surface stresses may be significant in the field, where

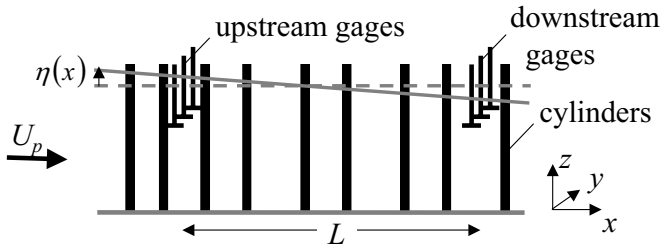

Figure 2-1: A section of the cylinder array. Surface displacement gages were placed a distance L apart longitudinally. In the presence of flow, the free surface (solid line) is displaced by vertical distance $\eta(x)$ from the still water level (dashed line) and a negative free surface gradient develops.

the bed is typically rough and wind may be non-negligible. Finally, we assume that flow conditions are fully developed, and $\partial \left\langle \overline{H} \right\rangle / \partial x$ is only retained to describe the pressure gradient. This is consistent with the horizontally homogeneous array. We thus obtain the balance between the total cylinder drag per unit volume of array and the longitudinal pressure gradient:

$$\left\langle \overline{f_D} \right\rangle_H m = -(1-\phi)\rho g \frac{\mathrm{d}\eta}{\mathrm{d}x}, \tag{2.11}$$

where $\eta(x)$ is the temporally- and spatially-averaged displacement of the free surface from the still water level (figure 2-1) and $\left\langle \overline{f_D} \right\rangle_H$ is the depth-averaged $\left\langle \overline{f_D} \right\rangle$. Eqs. (2.1) and (2.11) yield the following expression for the depth-averaged drag coefficient:

$$\frac{C_D \left\langle \overline{u} \right\rangle_H^2}{2} md = -(1-\phi) g \frac{\mathrm{d}\eta}{\mathrm{d}x}, \tag{2.12}$$

where $\left\langle \overline{u} \right\rangle_H$ is the depth-averaged $\left\langle \overline{u} \right\rangle$. By definition, $md = \phi/(\pi d/4)$, and Eq. (2.12) relates C_D with $\mathrm{d}\eta/\mathrm{d}x$ for a given ϕ, d, and $\left\langle \overline{u} \right\rangle_H$. Where Eq. (2.12) is valid, Manning's coefficient n_M is related to C_D as

$$n_M = \frac{R_h^{2/3}}{(1-\phi)^{3/2}} \sqrt{\frac{C_D}{2g} md}, \tag{2.13}$$

where R_h is the hydraulic radius.

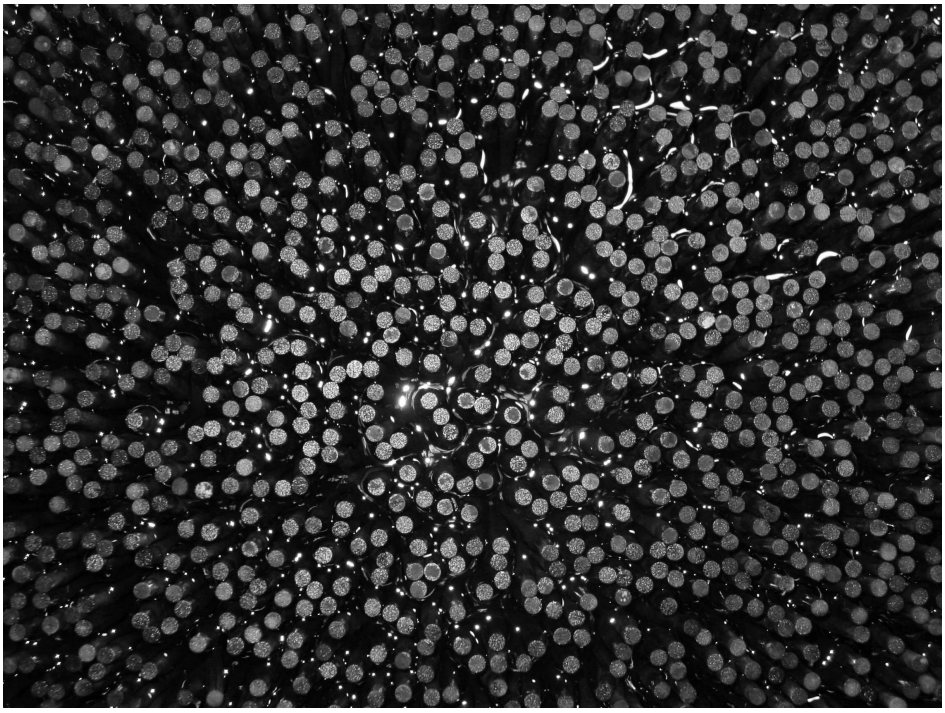

Figure 2-2: A section of the $\phi = 0.27$ array in plan view.

2.3 Experimental procedure

Laboratory experiments were performed in two Plexiglas recirculating flumes. Tank A, with a working section of $(x \times y \times z) = 284$ cm $\times$ 40 cm $\times$ 43 cm, was used for $\phi = 0.15$, 0.20, 0.27, and 0.35 and tank B, with a working section of $(x \times y \times z) =$ 670 cm $\times$ 20.3 cm $\times$ 30.5 cm, was used for $\phi = 0.091$. In each flume, the volumetric flow rate Q was measured with an in-line flow meter.

Cylindrical maple dowels of diameter $d = 0.64$ cm (Saunders Brothers, Inc.) were used as laboratory models for vegetation. The dowels were inserted into four 71.1 cm $\times$ 40.0 cm custom-made PVC sheets of either $\phi = 0.20$ or 0.35 hole fraction to create a 284 cm-long array that spanned the flume width. The PVC sheets were created by generating uniformly-distributed random coordinates for the hole centers until the desired number of non-overlapping holes were assigned. Here, non-overlapping holes were defined to not have any other hole center fall within a $2d \times 2d$ square around its center. The $\phi = 0.20$ and 0.35 arrays were created by completely filling these sheets, and the $\phi = 0.091$, 0.15, and 0.27 arrays were created by partially

filling the sheets. For the latter arrays, the holes that were filled were selected by MATLAB's random number generator. Figure 2-2 is a plan view of the $\phi = 0.27$ array.

$\eta(x)$ was measured using two sets of surface displacement gages. The gages were positioned a longitudinal distance L apart inside the array, with each set attached to a vertical traverse (figure 2-1). Each set consisted of two or three gages that were distributed laterally across the width of the flume. Each gage outputs voltage proportional to its submerged length. The signal was amplified before it was sent to the computer to be collected with the acoustic Doppler velocimeter (ADV) data acquisition software ADVA.exe version 4.4 by SonTek, Inc.. Measurements from all displacement gages were simultaneously recorded and time averaged to yield a mean voltage value for each gage.

After steady conditions were achieved, voltage measurements were recorded over five to twenty minutes. The surface displacement from the still water level for the j^{th} gage was determined from the time average of the voltage record at that gage, V_j:

$$\eta_j = \frac{V_j - V_{0_j}}{(\mathrm{d}V/\mathrm{d}z)_j}. \tag{2.14}$$

V_{0_j} is the time-averaged voltage reading at the j^{th} gage in still water. $(\mathrm{d}V/\mathrm{d}z)_j$ is the gradient of the linear regression of the calibration data for the j^{th} gage. The local time-averaged water depth at each displacement gage was $\overline{H}_j = H_{SWL} + \eta_j$, where $z = H_{SWL}$ is the still water level. The mean water depth between the displacement gages, $\left\langle \overline{H} \right\rangle_L$, was estimated as the average of the mean $\overline{H}_j$ at the upstream gages and the downstream gages. In the present experiments, $\left\langle \overline{H} \right\rangle_L$ ranged from 10.0 to 21.8 cm. The gradient of the free surface, $\mathrm{d}\eta/\mathrm{d}x$, was estimated by calculating the mean of η_j measured by the downstream gages and the mean of η_j measured by the upstream gages, subtracting the latter from the former, and dividing the result by L. The cross-sectionally averaged pore velocity between the gages was estimated as $U_p = Q/\left(\left\langle \overline{H} \right\rangle_L W(1-\phi)\right)$, where W is the width of the flume. In the present thesis, $\langle \overline{u} \rangle_H$ is approximated by U_p. Similarly, the Reynolds number was calculated

as $Re_d \equiv U_p d/\nu$. Finally, $\left\langle \overline{f_D} \right\rangle_H / (\mu U_p)$ and C_D were determined by substituting the values for U_p and $\mathrm{d}\eta/\mathrm{d}x$ into Eqs. (2.11) and (2.12).

For each experiment, the most conservative estimate of the maximum and minimum C_D was calculated by considering the maximum and minimum $\mathrm{d}\eta/\mathrm{d}x$ and U_p estimates. The other variables in Eq. (2.12) do not contribute significantly to the uncertainty. The maximum and minimum $\mathrm{d}\eta/\mathrm{d}x$ are the gradient of the least-squares fit to data plus and minus its uncertainty, as defined by Taylor (1997, Ch. 8.4). The uncertainty in U_p reflects that of the flow meter reading. Variations in the temperature over the duration of each experiment is also included in the uncertainty for Re_d. In tank A, a change in temperature was not observed. In tank B, water temperature increased by as much as 1°C during one time record.

2.4 Experimental results

At low Re_d, small ϕ, or small L, the surface displacement at the gages was very small, which resulted in large uncertainties or, in some cases, negative C_D estimates. In all subsequent discussion, we exclude all C_D measurements with an uncertainty greater than 25% of the estimated C_D and measurements that are negative within uncertainty. The remaining 120 measurements are discussed below. The range of Re_d at each ϕ is provided in Table 2.2.

The normalized drag, $\left\langle \overline{f_D} \right\rangle_H / (\mu U_p)$, is presented in figure 2-3 as a function of Re_d. $\left\langle \overline{f_D} \right\rangle_H / (\mu U_p)$ clearly exhibits a linear dependence on Re_d for all ϕ, consistent with Eq. (2.6). Moreover, $\left\langle \overline{f_D} \right\rangle_H / (\mu U_p)$ at a given Re_d increases with ϕ under the conditions investigated. The figure also includes the least-squares fits to Koch and Ladd (1997)'s simulation results in random cylinder arrays of $\phi = 0.05$ to 0.4 and $5 < Re_d < 100$ (see Table 2.2 for numerical values of the coefficients). At $Re_d < 100$, $\left\langle \overline{f_D} \right\rangle_H / (\mu U_p)$ for $\phi = 0.15$, 0.20, 0.27, and 0.35 fall between Koch and Ladd (1997)'s $\phi = 0.2$ and 0.4 predictions.

The gradient, α_1, and the intercept with the ordinate axis, α_0, of the line of regression of $\left\langle \overline{f_D} \right\rangle_H / (\mu U_p)$ on Re_d are presented in figure 2-4. To estimate these

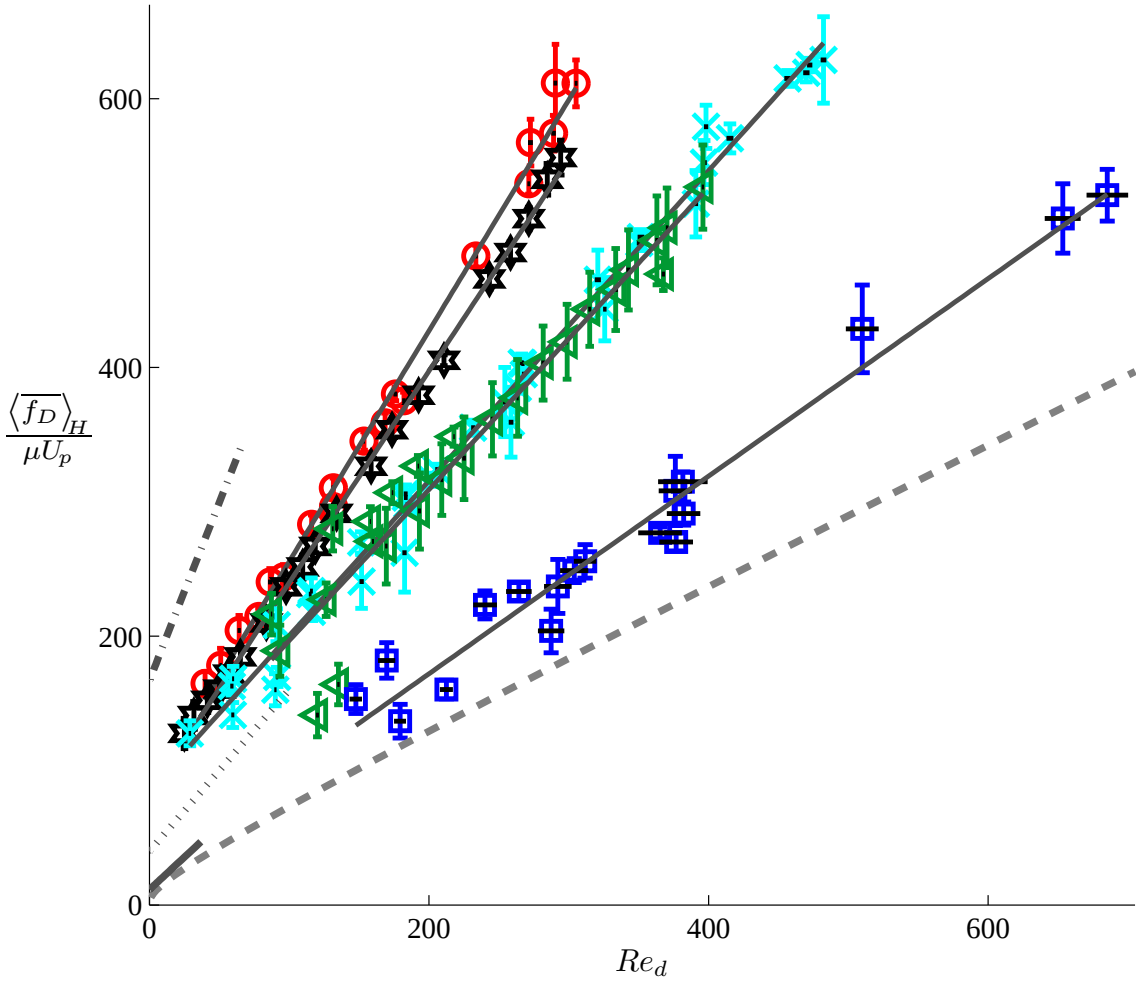

Figure 2-3: $\langle \overline{f_D} \rangle_H / (\mu U_p)$ at $\phi = 0.091$ (square), 0.15 ($\triangleleft$), 0.20 ($\times$), 0.27 (hexagram), and 0.35 ($\circ$), as defined in Eq. (2.11). Solid line marks the linear regression for each ϕ. Grey lines represent Koch and Ladd (1997)'s numerical results at $\phi = 0.05$ (solid), 0.2 (dotted), and 0.4 (dash-dotted), as presented in Table 2.2. The isolated cylinder solution (2.9) is also presented (grey, dashed). Horizontal and vertical lines on present data represent the uncertainty in Re_d and C_D, respectively, as described in the text.

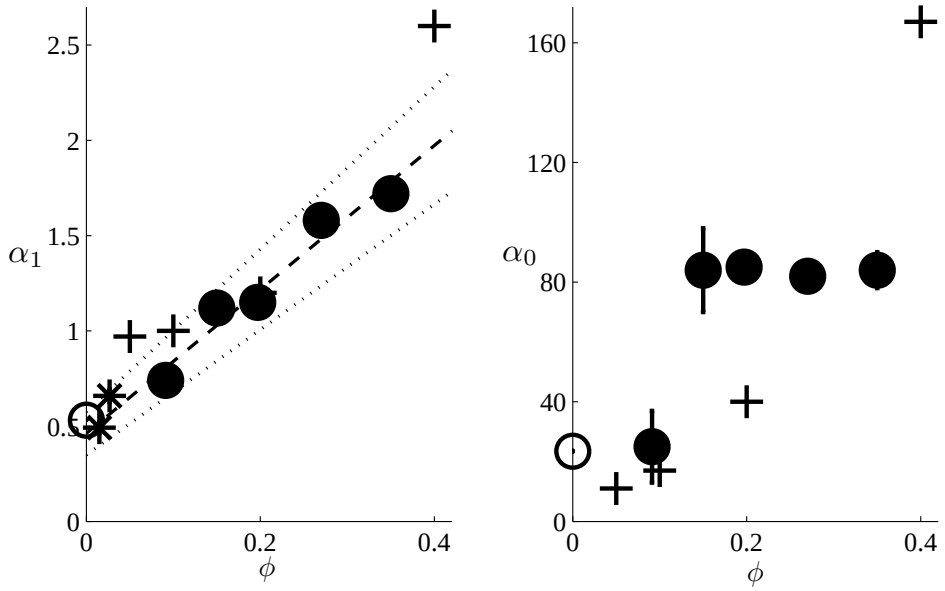

Figure 2-4: The coefficients of Eq. (2.6) estimated from a linear regression on the present laboratory measurements (solid $\circ$), on Petryk (1969)'s laboratory measurements ($*$), on interpolated values of Eq. (2.9) (open $\circ$), and on Koch and Ladd (1997)'s numerical results ($+$). See Table 2.2 for numerical values. Vertical bars on present data points and Petryk (1969)'s data points represent the uncertainty estimated from the regression, as suggested by Taylor (1997, Ch. 8.4). Where the vertical bars are not visible, they are smaller than the marker size. The dashed and dotted lines are the line of regression of α_1 on ϕ and the associated uncertainty as suggested by Taylor (1997, Ch. 8.4), respectively [Eq. (2.15)].

coefficients for the isolated cylinder, Eq. (2.9) was interpolated over $Re_d = 148 - 678$ in increments of 10. A linear regression on these interpolated values yields a correlation coefficient $R = 1.000$ ($n = 54$) and the coefficients $\alpha_0 = 23.5 \pm 0.2$ and $\alpha_1 = (5318 \pm 6) \times 10^{-4}$. The Re_d range selected here coincides with that for which α_0 and α_1 were determined for $\phi = 0.091$ (Table 2.2). As the Re_d range over which the linear regression is applied increases, α_0 increases and α_1 approaches 0.50. This sensitivity to Re_d reflects the deviation of Eq. (2.9) from a linear Re_d dependence. Estimated values of the coefficients are included in Table 2.2.

α_1 increases monotonically with ϕ, which implies that the inertial contribution increases with ϕ at a given Re_d. A linear regression on α_1 and ϕ from the present chapter yields

$$\alpha_1 = (0.46 \pm 0.11) + (3.8 \pm 0.5)\phi, \tag{2.15}$$

with $R = 0.98$ ($n = 5$). α_1 estimates based on Petryk (1969)'s data and the isolated cylinder solution agree within uncertainty with Eq. (2.15), suggesting that this empirical expression is valid at ϕ below those investigated in this thesis. Recall that, from dimensional analysis, α_1 and $\langle \overline{u}''^2 \rangle / \langle \overline{u} \rangle^2$ are expected to exhibit the same ϕ dependence [Eq. (2.5)]. As will be shown in Appendix I, measured $\langle \overline{u}''^2 \rangle / \langle \overline{u} \rangle^2$ does indeed increase with increasing ϕ, even though the rate of its increase with ϕ changes at $\phi \approx 0.1$.

α_0 measured in the present thesis is not linearly proportional to $d/\langle s_n \rangle_A$ and is inconsistent with Eq. (2.4) (figure 2-5, $\circ$). α_0 increases from 25 ± 12 at $\phi = 0.091$ to 84 ± 14 at $\phi = 0.15$, but remains constant within uncertainty for $\phi = 0.15$ to 0.35 at $\alpha_0 = 83.8$, with a standard error of 0.6 ($n = 4$). It should be noted that α_0 is very sensitive to slight changes in the gradient of the line of regression, i.e., α_1. For example, a linear regression on interpolated values for the isolated cylinder yields $\alpha_0 = 114.6 \pm 0.1$ if applied over $Re_d = 10^4$ to 10^5, instead of $\alpha_0 = 23.5 \pm 0.25$ obtained when the regression is applied over $Re_d = 148$ to 678. In contrast, α_1 only changes from $0.5318 \pm 6 \times 10^{-4}$ to $0.5013 \pm 2 \times 10^{-6}$. This may explain the high values of α_0 associated with Petryk (1969)'s measurements. Indeed, α_0 evaluated from Koch and

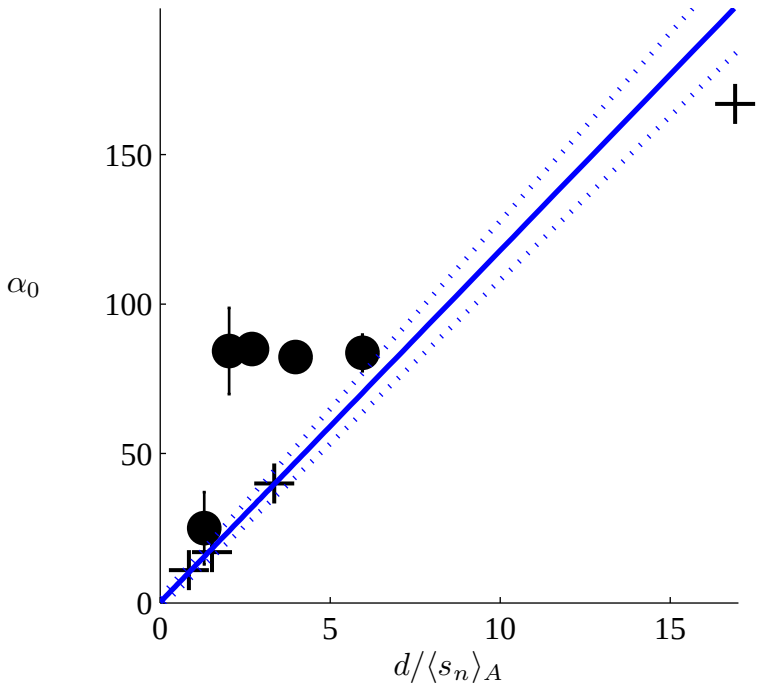

Figure 2-5: α_0 estimated from a linear regression on the present laboratory measurements (solid $\circ$) and on Koch and Ladd (1997)'s numerical results (+). Data are the same as those in figure 2-4. $d/\langle s_n \rangle_A$ is predicted from ϕ by Eq. (D.18) for the present data and by Eq. (D.10) for all other data. The solid and dotted lines are Eq. (2.16).

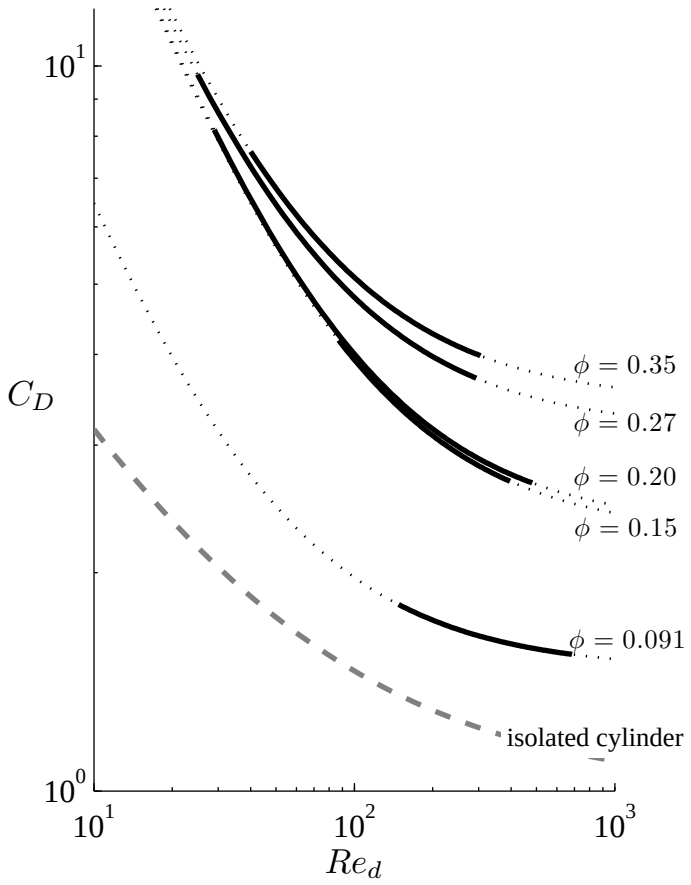

Figure 2-6: C_D as a function of Re_d for $\phi = 0.091$, 0.15, 0.20, 0.27, and 0.35 in the form of Eq. (2.7) with the fitted coefficients (solid lines) (Table 2.2). For reference, the fitted lines were extrapolated beyond the Re_d range of the data set (dotted). Eq. (2.8) (dashed) is also plotted.

Ladd (1997)'s simulation data exhibits a linear dependence on $d/\langle s_n \rangle_A$ [figure 2-5, +], as predicted by Eq. (2.4). Specifically, a linear regression on α_0 in the range $\phi = 0.05 - 0.2$ ($d/\langle s_n \rangle_A = 0.84 - 3.4$) yields

$$\alpha_0 = (0.2 \pm 1.8) + (11.8 \pm 0.8)\frac{d}{\langle s_n \rangle_A}, \tag{2.16}$$

with $R = 1.00$ ($n = 3$). The discrepancy between Eq. (2.16) and simulation at $\phi = 0.4$ ($d/\langle s_n \rangle_A = 17$) is attributed in part to the overestimation of $d/\langle s_n \rangle_A$ by the theoretical formulation (Appendix D.2). In other words, $d/\langle s_n \rangle_A$ in the $\phi = 0.4$ array is expected to have been smaller than that predicted by Eq. (D.10) and assumed in figure 2-5.

Figure 2-6 illustrates C_D as a function of Re_d. C_D decreases as Re_d increases for all ϕ investigated. The data also demonstrate that C_D in a random array is larger than the isolated cylinder for $O(30) \leq Re_d \leq O(700)$ for $\phi \leq 0.35$. Results by Koch and Ladd (1997) and Petryk (1969) suggest that this functionality extends to all conditions they considered, as summarized in Table 2.2. In contrast, Nepf (1999)'s measurements suggest that C_D is smaller than that of the isolated cylinder at higher Re_d.

Finally, note that while the numerical values measured in the present study only apply to randomly-distributed smooth circular cylinders, the qualitative trends are expected to extend to plant stems of slightly different morphology and distribution. Specifically, C_D is expected to decrease as Re_d increases and increase as ϕ increases. For example, James et al. (2004)'s laboratory measurements of the depth-integrated drag exerted by an isolated *Phragmites australis* reed show that foliage enhances C_D in the range $Re_d = 300 - 5000$, where C_D was defined using the depth-integrated frontal area per unit depth as the characteristic plant width. Note that greater foliage implies larger ϕ. Similarly, Ayaz and Pedley (1999) and Stone and Shen (2002, Table 2) report increasing C_D with increasing ϕ in square and staggered arrays, respectively. Koch and Ladd (1997) also investigated square arrays at various orientation to the mean flow. Based on their tabulated results (Koch and Ladd, 1997, Tables 1 and 2), C_D is higher at $\phi = 0.4$ than 0.2 in each configuration for $50 < Re_d < 350$. These results suggest that the qualitative ϕ dependence may be independent of configuration.

2.5 Conclusions

Laboratory measurements of array drag were presented in the form of the array-averaged C_D and $\left\langle \overline{f_D} \right\rangle_H / (\mu U_p)$. Both C_D and $\left\langle \overline{f_D} \right\rangle_H / (\mu U_p)$ increase with ϕ. C_D monotonically decreases as Re_d increases. The Re_d dependence of $\left\langle \overline{f_D} \right\rangle_H / (\mu U_p)$ is consistent with Ergun (1952)'s formulation, as was observed by Koch and Ladd (1997). Therefore, $\left\langle \overline{f_D} \right\rangle_H / (\mu U_p)$ and C_D for a given ϕ can be predicted by interpolating the values for α_0 and α_1 from figure 2-4 and Eq. (2.15), respectively, and applying

them to Eqs. (2.6) and (2.7). However, these predictions are strictly valid only in the range $O(30) \leq Re_d \leq O(700)$. In particular, it should be noted that Nepf (1999) reports the opposite ϕ dependence of C_D at $Re_d > 1000$. Additional measurements are required to determine if our results can be extrapolated to higher Re_d. Similarly, the Re_d dependence changes as Re_d approaches 0. Koch and Ladd (1997) show for $\phi = 0.40$ that the drag exhibits a quadratic Re_d dependence at $0 < Re_d \leq 5$ and that Eq. (2.6) with coefficients as summarized in Table 2.2 underestimates $\left\langle \overline{f_D} \right\rangle_H / (\mu U_p)$ at $Re_d < 1$ (Koch and Ladd, 1997, figure 23). Because experimental constraints on L restricted the analysis to high Re_d (≥ 25), as discussed earlier, we could not capture the expected change in the Re_d dependence in the present study.

Source	ϕ	α_0	α_1	R	n	Re_d range
Petryk, 1969	0.015	$(3.0 \pm 1.2) \times 10^3$	0.49 ± 0.04	0.975	10	$(0.6 - 5) \times 10^4$
	0.027	$(3.2 \pm 2.4) \times 10^3$	0.66 ± 0.04	0.993	5	$(3 - 9) \times 10^4$
present study	0.091	25 ± 12	0.74 ± 0.03	0.985	18	$150 - 690$
	0.15	84 ± 14	1.12 ± 0.06	0.969	26	$87 - 400$
	0.20	85 ± 5	1.15 ± 0.02	0.996	37	$29 - 480$
	0.27	82 ± 2	1.58 ± 0.01	0.999	20	$25 - 290$
	0.35	84 ± 6	1.72 ± 0.03	0.997	19	$40 - 310$
Koch and Ladd, 1997	0.05	11	0.97			$5 - 37$
	0.1	17	1.0			$6 - 33$
	0.2	40	1.2			$6 - 100$
	0.4	167	2.6			$8 - 67$

Table 2.2: The coefficients of Eq. (2.6) estimated from a linear regression on the present laboratory measurements and Petryk (1969)'s laboratory measurements. The Re_d range includes only the experimental conditions of the cases that contributed to the linear regression. R is the correlation coefficient and n is the number of data points included in the regression. The upper and lower estimates for α_0 and α_1 represent the uncertainty in the linear regression estimated from the deviation of $\left\langle \overline{f_D} \right\rangle_H / (\mu U_p)$ from the regression, as suggested by Taylor (1997, Ch. 8.4). Also included are α_0 and α_1 extracted from a graphic representation of Koch and Ladd (1997)'s numerical results in Koch and Ladd, 1997, figure 26.

Chapter 3

Lateral dispersion at high Reynolds number[a]

Abstract

Laser-induced fluorescence was used to measure the lateral dispersion of passive solute in random arrays of rigid, emergent cylinders of solid volume fraction $\phi = 0.010$ to 0.35. Such densities correspond to those observed in aquatic plant canopies and complement those in packed beds of spheres, where $\phi \geq 0.5$. This chapter focuses on pore Reynolds number greater than $Re_{\langle s_n \rangle_A} = 74$, for which our laboratory experiments demonstrate that $K_{yy}/(U_p d)$, the lateral dispersion coefficient normalized by the mean velocity in the fluid volume, U_p, and the cylinder diameter, d, is independent of cylinder Reynolds number, Re_d. $K_{yy}/(U_p d)$ increases rapidly with ϕ from $\phi = 0$ to 0.031. Then, $K_{yy}/(U_p d)$ decreases from $\phi = 0.031$ to 0.20. Finally, $K_{yy}/(U_p d)$ increases again, more gradually, from $\phi = 0.20$ to 0.35. These observations are accurately described by the linear superposition of the proposed model of turbulent diffusion and existing models of dispersion due to the spatially-heterogeneous velocity field that arises from the presence of the cylinders. The contribution from turbulent diffusion scales with the spatially-averaged turbulence intensity, the characteristic length scale of turbulent mixing, and the effective porosity. From a balance between the production of turbulent kinetic energy by the cylinder wakes and its viscous dissipation, the mean turbulence intensity for a given cylinder diameter and

[a]This chapter is Tanino and Nepf, 2008c, with modifications; we thank the three anonymous reviewers for their comments on the manuscript. Some material in § 3.2.1 has been taken from Tanino and Nepf, 2008a. This chapter is based on work supported by the National Science Foundation grant EAR-0309188. Any opinions, conclusions, or recommendations expressed in this material are those of the authors and do not necessarily reflect the views of the National Science Foundation. The authors thank Brian L. White for providing unpublished ADV measurements from his Master's thesis (White, 2002) and Dr. Urs Neumeier for providing unpublished velocity measurements from Neumeier and Amos, 2006.

cylinder density is predicted to be a function of the form drag coefficient and the integral length scale l_t. We propose and experimentally verify that $l_t = \min\{d, \langle s_n \rangle_A\}$, where $\langle s_n \rangle_A$ is the average surface-to-surface distance between a cylinder in the array and its nearest neighbor. We further propose that only turbulent eddies with mixing length scale greater than d contribute significantly to net lateral dispersion, and that neighboring cylinder centers must be farther than r^* from each other for the pore space between them to contain such eddies. If the integral length scale and the length scale for mixing are equal, then $r^* = 2d$. Our laboratory data agree well with predictions based on this definition of r^*.

3.1 Introduction

Turbulence and dispersion in obstructed flows have been investigated for decades because of their relevance to transport in groundwater (e.g., Bear, 1979), to transport in flow around buildings (e.g., Davidson et al., 1995) and trees (e.g., Kaimal and Finnigan, 1994, Ch. 3), and to engineering applications such as contaminant transport and removal in artificial wetlands (Serra et al., 2004). In particular, flow in a packed bed of spheres has been examined intensively, and analytical descriptions of different mechanisms that contribute to dispersion in Stokes flow were derived by Koch and Brady (1985). In packed beds of spheres, the solid volume fraction ϕ is approximately constant at $\phi \approx 0.6$ (e.g., Mickley et al., 1965; Jolls and Hanratty, 1966; Han et al., 1985; Yevseyev et al., 1991; Dullien, 1979, p. 132). In contrast, previous studies on emergent (i.e., spanning the water column and penetrating the free surface), rigid aquatic vegetation have focused on low solid volume fraction arrays ($\phi = 0.0046$ to 0.063, e.g., Nepf et al., 1997; White and Nepf, 2003). Such sparse arrays are characteristic of salt marshes, for example, where $\phi = 0.001 - 0.02$ (Valiela et al., 1978; Leonard and Luther, 1995). However, ϕ in aquatic plant canopies can approach that of packed beds. In mangroves, for example, ϕ can reach 0.45 because of the dense network of roots (Mazda et al., 1997). In constructed wetlands, ϕ may extend to 0.65 (Serra et al., 2004), and in this context Serra et al. (2004) reported lateral dispersion measurements at low Reynolds numbers in random arrays of $\phi = 0.10$, 0.20, and 0.35. In this chapter, turbulence and solute transport in arrays of randomly-distributed, emergent, rigid cylinders of $\phi = 0.010$ to 0.35 in turbulent flow are investigated.

Models for turbulence intensity and net lateral dispersion are presented and verified with laboratory measurements.

In § 3.2, we present a model for the mean turbulence intensity and the lateral dispersion coefficient as a function of cylinder distribution and cylinder density. In § 3.3, the experimental procedure for measuring turbulence, the integral length scale, and net lateral dispersion is described. In § 3.4, the experimental results are presented and compared with the theory.

3.2 Background theory

3.2.1 Solute transport in a random array

Species conservation is described by the expression

$$\frac{\partial c}{\partial t} + \boldsymbol{v} \cdot \boldsymbol{\nabla} c = -\boldsymbol{\nabla} \cdot (-D_m \boldsymbol{\nabla} c), \tag{3.1}$$

where $c(\boldsymbol{x}, t)$ is the solute concentration and D_m is the molecular diffusion coefficient. In obstructed turbulent flows, it is convenient to first decompose c and $\boldsymbol{v}$ into a local time average and instantaneous deviations from that average, and to further decompose the time-averaged parameters into a spatial average and local deviations from that average (e.g., Raupach and Shaw, 1982; Finnigan, 1985). As in Ch. 2, the temporal averaging operation, denoted by an overbar, is defined with a time interval much longer than the time scales of turbulent fluctuations and vortex shedding. The spatial averaging operation, denoted by $\langle\ \rangle$, is defined with an infinitesimally thin volume interval V_f that spans many cylinders. The solid (cylinder) volume is excluded from V_f. Then, $c = \langle \overline{c} \rangle(\boldsymbol{x}, t) + \overline{c}''(\boldsymbol{x}, t) + c'(\boldsymbol{x}, t)$ and $\boldsymbol{v} = \langle \overline{\boldsymbol{v}} \rangle(\boldsymbol{x}, t) + \overline{\boldsymbol{v}}''(\boldsymbol{x}, t) + \boldsymbol{v}'(\boldsymbol{x}, t)$, where $^{-\prime\prime}$ denotes the spatial fluctuations of the temporal average and $'$ denotes the temporal fluctuations. By definition, $\overline{c'}, \overline{\boldsymbol{v}'}, \langle \overline{c}'' \rangle, \langle \overline{\boldsymbol{v}}'' \rangle = 0$. Also, $\langle \overline{v} \rangle = \langle \overline{w} \rangle = 0$, by our definition of Cartesian coordinates. Substituting these expressions into Eq. (3.1), averaging over the same temporal and spatial intervals, and retaining only

the dominant terms yield [Finnigan, 1985, Eq. (21)]

$$\frac{\partial\langle\overline{c}\rangle}{\partial t} + \langle\overline{v}_j\rangle\frac{\partial\langle\overline{c}\rangle}{\partial x_j} = -\frac{\partial}{\partial x_j}\left\{\left\langle\overline{v_j'c'}\right\rangle + \left\langle\overline{v}_j''\overline{c}''\right\rangle - D_m\left\langle\frac{\partial}{\partial x_j}\left(\langle\overline{c}\rangle + \overline{c}''\right)\right\rangle\right\}. \tag{3.2}$$

In addition to fluxes associated with the local temporal fluctuations, $\left\langle\overline{\boldsymbol{v}'c'}\right\rangle$, the averaging scheme introduces dispersive fluxes associated with the time-averaged spatial fluctuations, $\langle\overline{\boldsymbol{v}}''\overline{c}''\rangle$.

In uniform, time-independent mean flow through a spatially-homogeneous random array, long-range velocity correlations are not expected because of the obstructions (Koch and Brady, 1985; Koch et al., 1998). Accordingly, Fickian dispersion is expected after sufficiently long time after the solute is introduced to the flow, once the spatial scale over which the mean concentration gradient varies exceeds the finite scales of the velocity correlations (Corrsin, 1974). Previous (White and Nepf, 2003; Acharya et al., 2007) and present (figures 3-13, 4-5, 4-6, H-2, H-3) observations of dispersion support this conjecture. Then, Eq. (3.2) reduces to

$$\frac{\partial\langle\overline{c}\rangle}{\partial t} + \langle\overline{v}_j\rangle\frac{\partial\langle\overline{c}\rangle}{\partial x_j} = -\frac{\partial}{\partial x_j}\left(-K_{jj}\frac{\partial\langle\overline{c}\rangle}{\partial x_j}\right) = K_{jj}\frac{\partial^2\langle\overline{c}\rangle}{\partial {x_j}^2}, \tag{3.3}$$

where K_{jj} are the coefficients for asymptotic (long-time/long-distance) net dispersion. The first equality in Eq. (3.3) states that the sum of the fluxes on the right-hand side of Eq. (3.2) obeys Fick's law. The second equality states that K_{jj} is spatially homogeneous, which is expected in a homogeneous array.

In this thesis, we are only concerned with the lateral component of the macroscopic dispersion coefficient, K_{yy}. Consider an experiment in which solute particles are released continuously from a point source ($\boldsymbol{x} = \boldsymbol{0}$). Then, $\overline{c}(\boldsymbol{x})$ is the temporal average of the solute concentration observed at some point $\boldsymbol{x}$ during a single experiment, and $\langle\overline{c}\rangle(\boldsymbol{x})$ is its ensemble average. If the solute is transported according to Eq. (3.3), the lateral variance of its distribution is related to K_{yy} as (Fischer et al., 1979)

$$\frac{K_{yy}}{\langle\overline{u}\rangle d} = \frac{1}{2d}\frac{\mathrm{d}}{\mathrm{d}x}\left[\left\langle\sigma_y^2(x)\right\rangle + \left\langle\left(\frac{m_1}{m_0}(x)\right)^2 - \left\langle\frac{m_1}{m_0}(x)\right\rangle^2\right\rangle\right], \tag{3.4}$$

where σ_y^2 and m_1/m_0 are the variance and the center-of-mass, respectively, of the time-averaged lateral concentration distribution at a given x in a single experiment; $\langle m_1/m_0 \rangle$ and the expression inside [ ] are the center-of-mass and variance, respectively, of $\langle \overline{c} \rangle$ at a given x. From Eq. (3.3), it follows that $\mathrm{d}\langle m_1/m_0 \rangle / \mathrm{d}x = 0$. Further, since m_1/m_0 is the mean lateral displacement of many solute particles, $\mathrm{d}\left\langle (m_1/m_0)^2 \right\rangle / \mathrm{d}x$ also approaches zero at sufficiently large x. Then, Eq. (3.4) reduces to

$$\frac{K_{yy}}{\langle \overline{u} \rangle d} = \frac{1}{2d} \frac{\mathrm{d}}{\mathrm{d}x} \left\langle \sigma_y^2(x) \right\rangle . \tag{3.5}$$

$\langle \sigma_y^2 \rangle$ at selected ϕ (= 0.091 and 0.20) and x is found to increase with increasing Re_d up to $Re_d \approx 100$ and is constant above $Re_d \approx 200$ (figure A-1). At lower ϕ, however, the transition between Re_d-dependent and Re_d-independent $\langle \sigma_y^2 \rangle$ regimes appears to occur at lower Re_d (Appendix A). While it is not clear if the *transition* between the two regimes can be identified by a single Reynolds number across all ϕ, measurements collected at $Re_{\langle s_n \rangle_A} > 74$ in the present thesis are independent of Reynolds number at all ϕ (Appendix A). In this chapter, we focus on lateral dispersion in this high Reynolds number regime.[b] In the next chapter, we will examine dispersion at Re_d below this regime for selected ϕ.

Like molecular diffusion, $\left\langle \overline{\boldsymbol{v}' c'} \right\rangle$ and $\langle \bar{\boldsymbol{v}}'' \bar{c}'' \rangle$ are expected to be individually Fickian if the spatial scale of the contributing mechanisms are much smaller than the scale over which the mean concentration gradient varies (Corrsin, 1974; Koch and Brady, 1985; White and Nepf, 2003). The two mechanisms associated with $\left\langle \overline{v' c'} \right\rangle$ and $\langle \overline{v}'' \overline{c}'' \rangle$, as identified below, both have characteristic scales of d and $\langle s_n \rangle_A$ (§ 3.2.2 and § 3.2.3). Because these lengths are finite and, by definition, much smaller than the dimensions of the averaging volume V_f, the solute particles will eventually be dispersed over many d and $\langle s_n \rangle_A$. At this time, $\langle \overline{c} \rangle$ will also vary slowly at these spatial scales. Therefore, $\left\langle \overline{v' c'} \right\rangle$ and $\langle \overline{v}'' \overline{c}'' \rangle$ are expected to be Fickian at long times (i.e., at long distances

[b]The actual criterion used in Tanino and Nepf, 2008c is $Re_s \equiv \langle \overline{u} \rangle s/\nu > 250$, where $\langle \overline{u} \rangle$ was defined at the LIF measurement location and $s \equiv 1/\sqrt{m} - d$ is the surface-to-surface distance between aligned cylinders in a square array with the same ϕ and d; m is the number of cylinders per unit area [Tanino and Nepf, 2008c, figure 1(b)]. In this chapter, the empirical criterion is expressed as $Re_{\langle s_n \rangle_A} > 74$ for consistency with the rest of this thesis.

downstream of the solute source). Consequently, K_{yy} is expected to be the linear sum of three constant coefficients, one that parameterizes $\left\langle \overline{v'c'} \right\rangle$, one that parameterizes $\langle \overline{v}''\overline{c}'' \rangle$, and the molecular diffusion coefficient. The first two coefficients represent, respectively, (i) turbulent diffusion and (ii) mechanical dispersion (i.e., independent of molecular diffusion) due to the spatially-heterogeneous velocity field generated by the randomly distributed cylinders. In this chapter, the two processes are treated as independent, and one is not considered in the description of the other. Molecular diffusion is negligible, as we only consider turbulent flow.

3.2.2 Contribution from turbulence

The classic scaling for turbulent diffusion is $K_{yy} \sim \langle \sqrt{k_t} \rangle l_e$, where l_e is the length scale associated with mixing due to turbulent eddies and $k_t \equiv (\overline{u'^2} + \overline{v'^2} + \overline{w'^2})/2$ is the turbulent kinetic energy per unit mass. Previously, Nepf (1999) assumed that, in a cylinder array, l_e is equal to the integral length scale of the largest turbulent eddies, l_t, and that $l_t = d$ when cylinder spacing is smaller than the water depth. Then, $K_{yy} \sim \langle \sqrt{k_t} \rangle d$. Nepf (1999) fitted this turbulent diffusion scale to experimental observation at $Re_d = 190 - 790$ in a $\phi = 0.0046$, periodic, staggered cylinder array (Nepf et al., 1997, Table 1; see Zavistoski, 1994 for exact cylinder configuration) to obtain

$$\frac{K_{yy}}{U_p d} = 0.9 \left\langle \frac{\sqrt{k_t}}{U_p} \right\rangle . \tag{3.6}$$

The mean interstitial pore velocity U_p is the average of $\overline{u}$ over all fluid volume within the array, and is determined as $U_p = Q / \left[\left\langle \overline{H} \right\rangle W(1-\phi) \right]$, where Q is the time-averaged volumetric flow rate, $\left\langle \overline{H} \right\rangle$ is the mean water depth, and W is the width of the laboratory flume in which the array was contained. Note that $\langle \overline{u} \rangle \approx U_p$ if the thickness of the boundary layers at the bed and sidewalls of the flume are negligible relative to $\left\langle \overline{H} \right\rangle$ and W. Equation (3.6) is inconsistent with experiment at high ϕ, as will be demonstrated in § 3.4.3. Below, we propose a new scale model for turbulent diffusion, in which l_e and l_t may be constrained by cylinder spacing at high ϕ.

Turbulence intensity

The functionality of the mean turbulence intensity, $\langle\sqrt{k_t}/\langle\overline{u}\rangle\rangle$, can be predicted from the temporally- and spatially-averaged mean and turbulent kinetic energy budgets in the array [see, e.g., Raupach et al., 1991, Eq. (4.3a, b) or Kaimal and Finnigan, 1994, Eq. (3.40) for the turbulent kinetic energy budget]. In cylinder arrays, a wake production term, $-\left\langle \overline{v_i'v_j'}''\partial\overline{v_i}''/\partial x_j \right\rangle \quad (\geq 0)$, accounts for turbulence production by the cylinder wakes. Numerical simulation by Burke and Stolzenbach (1983, figure 5.23) demonstrates for $C_D\langle\overline{H}\rangle\phi/(\pi d/4) = 0.01 - 1.0$, where C_D is the coefficient of mean cylinder drag, that wake production exceeds production due to shear within the cylinder array, except near the bed. In fully-developed flow with negligible shear production, the turbulent kinetic energy budget reduces to a balance between wake production and viscous dissipation of turbulent kinetic energy (e.g., Burke and Stolzenbach, 1983; Raupach and Shaw, 1982):

$$0 \approx -\left\langle \overline{v_i'v_j'}''\frac{\partial\overline{v_i}''}{\partial x_j} \right\rangle - \nu\left\langle \overline{\frac{\partial v_i}{\partial x_j}'\frac{\partial v_i}{\partial x_j}'} \right\rangle. \tag{3.7}$$

Similarly, the mean kinetic energy budget reduces to

$$0 \approx \langle\overline{v_i}\rangle f_i^{\text{form}} + \left\langle \overline{v_i'v_j'}''\frac{\partial\overline{v_i}''}{\partial x_j} \right\rangle + \nu\left\langle \overline{v_i}''\nabla^2\overline{v_i}'' \right\rangle, \tag{3.8}$$

where

$$f_i^{\text{form}} = \frac{1}{\rho V_f}\iint_{S_c}\overline{p}n_i\ \mathrm{d}S \quad (\geq 0) \tag{3.9}$$

is the hydrodynamic force per unit fluid mass exerted on S_c that arises from the pressure loss in cylinder wakes, where S_c denotes all cylinder surfaces that intersect V_f, $\boldsymbol{n}$ is the unit normal vector on S_c pointing out of V_f, $p(\boldsymbol{x},t)$ is the local pressure, and ρ is the fluid density.

The Kolmogorov microscale η estimated from our laser Doppler velocimetry (LDV) measurements (see § 3.3) ranged from $\eta/d = 0.0014$ to 0.21 and $\eta/\langle s_n\rangle_A = 0.0036$ to 0.83. These $O(0.001 - 1)$ ratios suggest that wake production is a more significant sink of mean kinetic energy than the viscous term $\nu\langle\overline{v_i}''\nabla^2\overline{v_i}''\rangle$ (Raupach and Shaw,

1982). For simplicity, the latter is neglected in Eq. (3.8), which yields a balance between rate of work done by form drag and wake production [Raupach and Shaw, 1982, Eq. (17)]:

$$0 \approx \langle \overline{v_i} \rangle f_i^{\text{form}} + \left\langle \overline{v_i' v_j'}'' \frac{\partial \overline{v_i}''}{\partial x_j} \right\rangle . \tag{3.10}$$

Note that $i = 1$ is the only non-zero component of $\langle \overline{v_i} \rangle f_i^{\text{form}}$. Combining Eqs. (3.7) and (3.10) and replacing the viscous dissipation term with the classic scaling, $\sqrt{k_t}^3/l_t$ (Tennekes and Lumley, 1972), yield a model for mean turbulence intensity:

$$\left\langle \frac{\sqrt{k_t}}{\langle \overline{u} \rangle} \right\rangle \sim \left[\frac{\left\langle \overline{f_D} \right\rangle^{\text{form}}}{\rho \langle \overline{u} \rangle^2 d/2} \frac{l_t}{d} \frac{md^2}{2(1-\phi)} \right]^{1/3} , \tag{3.11}$$

where $\left\langle \overline{f_D} \right\rangle^{\text{form}} \equiv \rho(1-\phi) f_1^{\text{form}}/m$ is the inertial contribution to the mean drag (in the direction of mean flow) per unit length of cylinder. In Ch. 2, the following empirical relation for $\left\langle \overline{f_D} \right\rangle_H^{\text{form}}$, the depth average of $\left\langle \overline{f_D} \right\rangle^{\text{form}}$, was determined:

$$\frac{\left\langle \overline{f_D} \right\rangle_H^{\text{form}}}{\rho {U_p}^2 d/2} = 2\left[(0.46 \pm 0.11) + (3.8 \pm 0.5)\phi \right] . \tag{3.12}$$

For convenience, we define a drag coefficient that represents this contribution:

$$C_D^{\text{form}} \equiv \frac{\left\langle \overline{f_D} \right\rangle_H^{\text{form}}}{\rho {U_p}^2 d/2} . \tag{3.13}$$

Laboratory measurements suggest that temporally- and spatially-averaged flow properties in the present thesis were approximately uniform vertically (e.g., figure 3-7; White and Nepf, 2003) and laterally (e.g., figure 3-6; White and Nepf, 2003). Consequently, $\left\langle \overline{f_D} \right\rangle^{\text{form}} \approx \left\langle \overline{f_D} \right\rangle_H^{\text{form}}$ and $\langle \overline{u} \rangle \approx U_p$. Then, Eq. (3.11) can be rewritten as:

$$\left\langle \frac{\sqrt{k_t}}{\langle \overline{u} \rangle} \right\rangle \approx \left\langle \frac{\sqrt{k_t}}{U_p} \right\rangle \sim \left[C_D^{\text{form}} \frac{l_t}{d} \frac{\phi}{(1-\phi)\pi/2} \right]^{1/3} , \tag{3.14}$$

where C_D^{form} is described by Eqs. (3.12) and (3.13). Recall that $m = \phi/(\pi d^2/4)$.

The choice of $l_t = d$ is convention in the literature on flow through vegetation

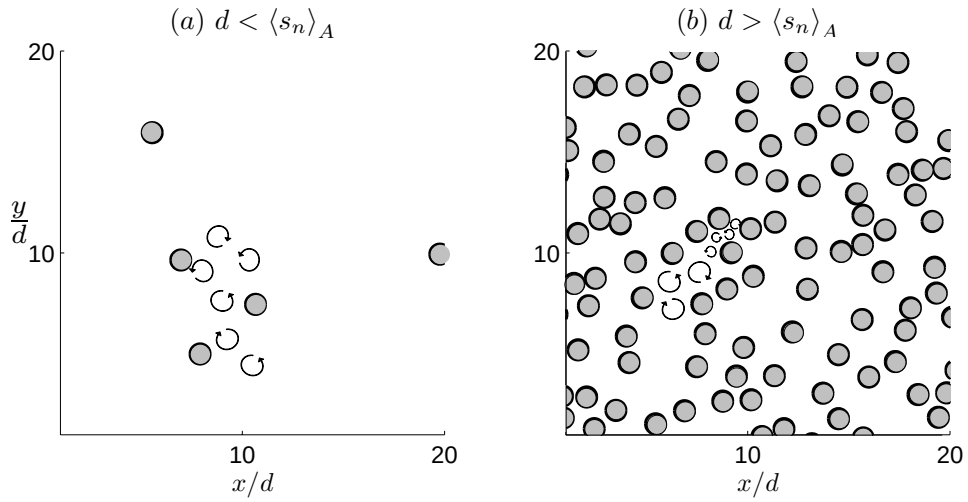

Figure 3-1: A section of simulated arrays of (a) $\phi = 0.010$ and (b) $\phi = 0.20$. Circles represent cylinders, to scale. Turbulent eddies, depicted by the arrows, are $O(d)$ in sparse arrays, but are constrained by the local cylinder separation where the pore length scale is smaller than d.

(e.g., Raupach and Shaw, 1982; Raupach et al., 1991) and is reasonable in sparse arrays [figure 3-1(a)]. In dense arrays, however, the local pore length scale may be less than $O(d)$. In these regions, physical reasoning suggests that the local cylinder spacing will constrain the eddies [figure 3-1(b)]. Therefore, l_t must be redefined at high ϕ. The simplest function consistent with the expected dependence on the local surface-to-surface distance between cylinders is

$$l_t = \min\{d,\ \langle s_n \rangle_A\}. \tag{3.15}$$

Turbulent diffusion coefficient

We expect the spatially-heterogeneous velocity field to induce lateral deflections of $O(d)$ per cylinder in the dispersion mechanism described in § 3.2.3 (e.g., Masuoka and Takatsu, 1996; Nepf, 1999). Therefore, we propose that only turbulent eddies with mixing length scale $l_e \geq d$ contribute significantly to net lateral dispersion relative to the spatially-heterogeneous velocity field. Let r^* be the minimum distance between cylinder centers that permits the pore space constrained by them to contain such eddies. Physical reasoning suggests that the mixing length scale associated with

turbulent eddies is approximately equal to the size of the eddies, i.e., $l_e \approx l_t$, which, together with Eq. (3.15), implies $r^* - d = d$. Then, within an infinitesimally thin section of the array whose total (solid and fluid) volume is denoted by V, the sum of all volume that contributes to turbulent diffusion, V_m ($\leq V$), is a sum of all pore space with length greater than $r^* - d$. Within these pores, $l_e = d$. To simplify, we associate all fluid volume with a cylinder. Further, each cylinder in the array has a fluid volume around it of characteristic horizontal area ${s_n}^2$. Then,

$$V_m = \langle {s_n}^2 \rangle_{s_{nc}>r^*} N_{s_{nc}>r^*}, \tag{3.16}$$

where $N_{s_{nc}>r^*}$ is the number of cylinders with $s_{nc} > r^*$ in V. Recall that $s_{nc} = s_n + d$.

To define K_{yy} as an average over both fluid and solid volume, local $\sqrt{k_t} l_e$ is integrated over V_m and divided by V. Then, the contribution from turbulent diffusion is

$$\frac{K_{yy}}{\langle \overline{u} \rangle d} = \gamma_1 \frac{\left\langle \sqrt{k_t} l_e \right\rangle_m}{\langle \overline{u} \rangle d} \frac{V_m}{V}, \tag{3.17}$$

where $\langle\ \rangle_m$ denotes a spatial average over V_m and γ_1 is the scaling constant. Equation (3.17) is simplified by neglecting the cross-correlations such that $\left\langle \sqrt{k_t} l_e \right\rangle_m = \left\langle \sqrt{k_t} \right\rangle_m \langle l_e \rangle_m$ and assuming that $\left\langle \sqrt{k_t} \right\rangle_m = \left\langle \sqrt{k_t} \right\rangle$, the average over all fluid volume. Equation (3.17) then becomes

$$\frac{K_{yy}}{\langle \overline{u} \rangle d} \approx \gamma_1 \left\langle \frac{\sqrt{k_t}}{\langle \overline{u} \rangle} \right\rangle \frac{\langle {s_n}^2 \rangle_{s_{nc}>r^*}}{d^2} \frac{\phi}{\pi/4} P_{s_{nc}>r^*}, \tag{3.18}$$

where $P_{s_{nc}>r^*} \equiv N_{s_{nc}>r^*}/(mV)$ is the fraction of cylinders with a nearest neighbor farther than r^* (center-to-center) from its center. Recall that $\left\langle \sqrt{k_t}/\langle \overline{u} \rangle \right\rangle$ can be described by Eqs. (3.14) and (3.15), given d and ϕ.

3.2.3 Contribution from the time-averaged, spatially-heterogeneous velocity field

Two existing models of lateral dispersion due to the spatially-heterogeneous velocity field are considered in this chapter. The simplest model describes the lateral deflection of fluid particles due to the presence of the cylinders as a one-dimensional random walk (Nepf, 1999). In this model, a fluid particle is considered to undergo a sequence of independent and discrete lateral displacements of equal length, where each displacement has equal probability of being in the positive or in the negative y direction. The long-time lateral dispersion of many such fluid particles is described by:

$$\frac{K_{yy}}{\langle \overline{u} \rangle d} = \frac{1}{2} \left(\frac{\epsilon}{d} \right)^2 \frac{\phi}{\pi/4}, \tag{3.19}$$

where ϵ, the magnitude of each displacement, is a property of the cylinder configuration and Re_d. Nepf (1999) proposed that $\epsilon = d$. With this assumption, Eq. (3.19) becomes a function of ϕ only.

The second model considered for this mechanism is Koch and Brady (1986)'s analytical solution for mechanical dispersion due to two-cylinder interactions in Stokes flow, with a modification to only include cylinders with a nearest neighbor sufficiently close to permit cylinder-cylinder interaction. Analytical solutions for long-time, Fickian dispersion in a homogeneous, sparse, random cylinder array were derived for Stokes flow by Koch and Brady (1986) by averaging the governing equations over an ensemble of arrays with different cylinder configurations. Neglecting molecular diffusion, lateral dispersion arises from the velocity disturbances induced by the randomly distributed cylinders (Koch and Brady, 1986). The authors demonstrate that this hydrodynamic dispersion consists of a mechanical component and non-mechanical corrections, but that only the mechanical contribution, associated with the spatially-heterogeneous velocity field due to the obstacles, has a non-zero lateral component. Further, the authors showed that, because of their fore-aft symmetry, circular cylinders do not contribute to lateral dispersion unless two-cylinder interactions are considered. Taking into consideration such interactions, Koch and Brady (1986) determined

that the mechanical contribution of the cylinder array in Stokes flow is

$$\frac{K_{yy}}{\langle \overline{u} \rangle d} = \frac{\pi}{4096} \left(\frac{d^2}{k_\perp} \right)^{3/2} \frac{1-\phi}{\phi^2}, \tag{3.20}$$

where $k_\perp$ is the permeability such that the mean drag (in the direction of mean flow) per unit length of cylinder is

$$\left\langle \overline{f_D} \right\rangle = \frac{\pi}{4} \frac{d^2}{k_\perp} \mu \langle \bar{u} \rangle \frac{1-\phi}{\phi}, \tag{3.21}$$

where μ is the dynamic viscosity. Numerical simulations show that $d^2 k_\perp^{-1}$ increases monotonically with ϕ [Koch and Ladd, 1997; figure E-1]. For sparse random arrays, $k_\perp$ is accurately described by Spielman and Goren (1968)'s analytical solution [Eq. (E.1)]. For dense arrays, Koch and Ladd (1997) have shown that a theoretical model based on the lubrication approximation accurately captures the dependence of $k_\perp$ on the characteristic distance between neighboring cylinders. $k_\perp$ for arrays of intermediate density, for which analytical expressions have not been derived, can be described by an empirical fit to numerical simulation data [Eq. (E.3)]. Models for $k_\perp$ relevant to our laboratory experiments are discussed in Appendix E.

Equation (3.20), where $k_\perp$ is described by Eq. (E.1), predicts that dispersion due to two-cylinder interactions will increase as ϕ decreases below $\phi = 0.017$. Koch and Brady (1986) attribute this predicted increase to the increase in the average distance over which velocity disturbances induced by a cylinder decay. This distance, known as the Brinkman screening length, scales with the square-root of permeability. As discussed in Appendix E, $\sqrt{k_\perp} \approx \langle s_n \rangle_A$ in sparse arrays. However, the fraction of cylinders with a neighbour close enough to result in cylinder-cylinder interaction decreases with decreasing ϕ, and physical reasoning suggests that the contribution from this process approaches zero as ϕ decreases to zero. Therefore, we introduce an adjustment to Koch and Brady (1986)'s solution. Previous studies in unsteady and turbulent flow report interacting wakes between side-by-side cylinders with center-to-center distance less than $5d$ (e.g., Zhang and Zhou, 2001; Meneghini et al., 2001).

Similarly, the drag on a cylinder is influenced by the presence of a neighboring cylinder that is within $5d$ (Petryk, 1969). Following these studies, we assume that only cylinders whose centers are within $5d$ of another cylinder center contribute to net dispersion through this mechanism. Accordingly, Koch and Brady (1986)'s solution is multiplied by the fraction of cylinders that have a nearest neighbor within $5d$, $P_{s_{nc}<5d}$. We assume that this process is otherwise unaffected by inertia. In addition, a scaling constant γ_2 is introduced. After the introduction of these two terms, Koch and Brady (1986)'s solution becomes

$$\frac{K_{yy}}{\langle\overline{u}\rangle d} = \gamma_2 P_{s_{nc}<5d} \frac{\pi}{4096} \left(\frac{d^2}{k_\perp}\right)^{3/2} \frac{1-\phi}{\phi^2}. \tag{3.22}$$

3.2.4 Coefficient for net lateral dispersion

Finally, an expression for net lateral dispersion is given by the linear superposition of the models for turbulent diffusion and dispersion due to the spatially-heterogeneous velocity field. For example, superposing Eq. (3.18) and the random walk model [Eq. (3.19)] yields:

$$\frac{K_{yy}}{\langle\overline{u}\rangle d} = \gamma_1 \frac{4}{\pi}\phi \left\langle \frac{\sqrt{k_t}}{\langle\overline{u}\rangle} \right\rangle P_{s_{nc}>r^*} \frac{\langle {s_n}^2 \rangle_{s_{nc}>r^*}}{d^2} + \frac{1}{2}\left(\frac{\epsilon}{d}\right)^2 \frac{\phi}{\pi/4}. \tag{3.23}$$

Similarly, superposing Eq. (3.18) and the proposed modification of Koch and Brady (1986)'s solution [Eq. (3.22)] yields:

$$\frac{K_{yy}}{\langle\overline{u}\rangle d} = \gamma_1 \frac{4}{\pi}\phi \left\langle \frac{\sqrt{k_t}}{\langle\overline{u}\rangle} \right\rangle P_{s_{nc}>r^*} \frac{\langle {s_n}^2 \rangle_{s_{nc}>r^*}}{d^2} + \gamma_2 P_{s_{nc}<5d} \frac{\pi}{4096} \left(\frac{d^2}{k_\perp}\right)^{3/2} \frac{1-\phi}{\phi^2}. \tag{3.24}$$

To permit analytical expressions for Eqs. (3.23) and (3.24), $P_{s_{nc}>r^*}$ and $P_{s_{nc}<5d}$ are approximated as the probability that a single cylinder in a random array will have a nearest neighbor farther away than $r = r^*$ and within $r = 5d$, respectively, where r is the radial coordinate defined with the origin at the center of that cylinder. Analytical expressions for $P_{s_{nc}>r^*}$, $P_{s_{nc}<5d}$, and $\langle {s_n}^2 \rangle_{s_{nc}>r^*}$ for the random arrays used in the present laboratory experiments are derived in Appendix D. Note that $P_{s_{nc}<5d}$ ap-

proaches one monotonically as ϕ increases from zero, with $P_{s_{nc}<5d} > 0.99$ at $\phi \geq 0.043$. Expressions for $k_\perp$ are presented in Appendix E.

3.3 Experimental procedure

Laboratory experiments were conducted to verify the definition of l_t [Eq. (3.15)] and the scale model for $\langle\sqrt{k_t}/\langle\overline{u}\rangle\rangle$ [Eq. (3.14)] and to document the ϕ dependence of $K_{yy}/(\langle\overline{u}\rangle d)$. Scaling constants in Eq. (3.14) and the model for $K_{yy}/(\langle\overline{u}\rangle d)$ [Eq. (3.24)] are determined from the experimental data. Recall that this chapter focuses on the high Re_d regime in which our measurements of the lateral concentration variance $\langle\sigma_y^2\rangle$, hence $K_{yy}/(\langle\overline{u}\rangle d)$, are independent of Re_d. An empirical criterion of $Re_{\langle s_n\rangle_A} > 74$ is used to identify the Re_d-independent σ_y^2 measurements [§ 3.2.1; see Table 3.3 for the exact $(Re_d, Re_{\langle s_n\rangle_A})$ range for each ϕ]. Similarly, turbulence intensity measurements were independent of Re_d at $Re_{\langle s_n\rangle_A} > 105$ (Table 3.2). Only these velocity measurements are considered in evaluating the scale models for l_t and $\langle\sqrt{k_t}/\langle\overline{u}\rangle\rangle$.

The laboratory study consisted of two parts: measuring velocity and imaging the lateral concentration profile of a passive solute. In both parts, cylindrical maple dowels of diameter $d = 0.64$ cm (Saunders Brothers, Inc.) were used to create arrays of eight densities: $\phi = 0.010$, 0.020, 0.031, 0.060, 0.091, 0.15, 0.20, and 0.35 for the velocity measurements and $\phi = 0.010$, 0.031, 0.060, 0.091, 0.15, 0.20, 0.27, and 0.35 for the solute study. All arrays, except for the $\phi = 0.031$ arrays, were created in custom-made 71.1 cm $\times$ 40.0 cm perforated PVC sheets of either 20% or 35% hole fraction. The location of the holes in these sheets were defined by generating uniformly-distributed random coordinates for the hole centers until the desired number of non-overlapping holes was assigned; these non-overlapping holes were drilled into the sheets. Here, non-overlapping holes were defined to not have any other hole center fall within a $2d \times 2d$ square around its center. Any directional bias resulting from this definition, instead of defining the overlap over a circle of radius d, is assumed negligible. The $\phi = 0.20$ and 0.35 arrays were created by filling all of the holes. The $\phi = 0.010, 0.020, 0.060, 0.091, 0.15$, and 0.27 arrays were created by

ϕ	array base	$d/\langle s_n \rangle_A$	array length [cm]	Δx_{gap} [cm]	n
0.010	PVC	0.28	569.0	0.0	118
0.020	PVC	0.43	497.8	0.0	147
0.031	Plexiglas	0.49	498.8	0.0	261
0.060	PVC	0.93	284.5	0.0	260
0.091	PVC	1.3	284.5	0.7 - 1.3	191
0.15	PVC	2.0	213.4	0.0	195
0.20	PVC	2.7	213.4	0.0, 0.1	136
0.35	PVC	5.9	106.1	0.3, 0.6	116, 22

Table 3.1: Array setup for laser Doppler velocimetry (LDV) measurements. Δx_{gap} is the width of the gap that was created in the cylinder array to permit multiple LDV measurements in each lateral transect. $\Delta x_{gap} = 0.0$ indicates an unmodified array. n is the total number of time records collected at $Re_{\langle s_n \rangle_A} > 105$ ($\phi = 0.010 - 0.20$) and both $Re_{\langle s_n \rangle_A} > 70$ and $Re_{\langle s_n \rangle_A} > 105$ for $\phi = 0.35$.

selecting the holes to be filled or to be left empty by MATLAB's random number generator. The $\phi = 0.031$ array in the solute study was created by partially filling 20% hole fraction PVC sheets with 1/2-inch staggered hole centers (Ametco Manufacturing Corporation). The $\phi = 0.031$ array used in the velocity measurements were created by partially filling Plexiglas boards that were designed by White and Nepf (2003). Note that White and Nepf (2003) defined non-overlapping holes to not have any other hole center fall within a concentric circle of diameter $4d$. In the solute study, the dowels were inserted into four PVC sheets placed along the bed of the working section of the flume. For the velocity measurements, different numbers of PVC sheets were used (see Table 3.1) because the density of cylinders increases with ϕ and a shorter array length is required to achieve fully-developed conditions at higher ϕ. The cylinders are perpendicular to the horizontal bed of the working section of the flume.

As stated previously, velocity measurements taken in emergent cylinder arrays by White and Nepf (2003) and in the present study (e.g., figures 3-6, 3-7) have shown that $\langle \overline{u} \rangle$ is approximately constant within the array, except very close to the bed and the sidewalls. Therefore, $\langle \overline{u} \rangle$ is approximated by U_p, measured as the Q divided by W, $\left\langle \overline{H} \right\rangle$, and $1 - \phi$. Recall that $\left\langle \overline{H} \right\rangle$ decreases along the length of the array to

balance the net drag exerted on the flow (Ch. 2). The maximum decrease in $\left\langle \overline{H} \right\rangle$ between the solute source and the LIF measurement location is estimated to have been 31% of the depth at the solute source for experiments reported in this chapter, and 17% for experiments reported in Ch. 4. $\left\langle \overline{H} \right\rangle$ was defined at the measurement location for velocity measurements and at the solute source in solute concentration measurements. Reynolds numbers were calculated using U_p as the velocity scale.

3.3.1 Velocity measurements

Velocity measurements were taken in a 670 cm × 20.3 cm × 30.5 cm recirculating Plexiglas laboratory flume using two-dimensional laser Doppler velocimetry (LDV) (Dantec Measurement Technology). The time-averaged water depth at the LDV sampling volume ranged from $\left\langle \overline{H} \right\rangle = 13.1$ cm to 22.1 cm. Flow was generated by a centrifugal pump and measured with an in-line flow meter. At each ϕ, time records of longitudinal and vertical velocity components were collected at positions $(s+d)/4$ apart along a lateral transect at several streamwise positions within the array for a range of Re_d. Recall that $s \equiv 1/\sqrt{m} - d$ is the surface-to-surface distance between aligned cylinders in a square array with the same ϕ and m is the number of cylinders per unit area [Tanino and Nepf, 2008c, figure 1(b)]. The lateral transects were at an elevation of $2\left\langle \overline{H} \right\rangle /3$ from the bed.

In total, 2107 time records were collected. The time average ($\overline{u}$, $\overline{w}$), the temporal deviations (u', w'), and the temporal variance ($\overline{u'^2}$, $\overline{w'^2}$) were calculated for each record as

$$\overline{u} = \frac{\sum_k u_k \Delta t_k}{\sum_k \Delta t_k}, \tag{3.25}$$

$$u'_k = u_k - \overline{u}, \tag{3.26}$$

and

$$\overline{u'^2} = \frac{\sum_k u_k^{'\,2} \Delta t_k}{\sum_k \Delta t_k}, \tag{3.27}$$

respectively, where Δt_k is the residence time of the k^{th} seeding particle in the LDV sampling volume. The vertical components are defined analogously. Note that only

$u(t)$ and $w(t)$ could be measured. However, previous measurements indicate $\overline{v'^2} \approx \overline{u'^2}$ (figure B-1), and the turbulent kinetic energy per unit mass, k_t, was determined as $k_t = (2\overline{u'^2} + \overline{w'^2})/2$.

The integral length scale l_t can be estimated from the time record of turbulent fluctuations. Specifically, the Eulerian integral length scale is approximately equal to $|\overline{u}|/(2\pi f_{peak,v_j})$, where f_{peak,v_j} is the frequency at which the frequency-weighted power spectral density of v'_j peaks (Kaimal and Finnigan, 1994, p. 38) and is one measure of l_t (e.g., Pearson et al., 2002). To determine f_{peak,v_j}, $u'(t)$ and $w'(t)$ records were resampled at uniform time intervals by linear interpolation. The shortest interval between consecutive samples in that time record was used as the interval. The power spectral densities [cm^2 s^{-2} Hz^{-1}] of the reevaluated $u'(t)$ and $w'(t)$ were determined using MATLAB's pwelch.m function. A peak at 120 Hz exists in most records, which is attributed to background noise. Because this frequency is one order of magnitude higher than the maximum U_p/d in our experiments, which was 15 Hz, it is assumed that this noise did not interfere with the analysis. Also, the resampled record is accurate only to $f = \overline{f_{raw}}/(2\pi)$, where $\overline{f_{raw}}$ is the mean data rate of the raw time record (Tummers and Passchier, 2001). Accordingly, frequencies above $\overline{f_{raw}}$ and 110 Hz were neglected in the analysis. Finally, l_t was estimated from the frequency $f_{peak,u}$ corresponding to the peak in the frequency-weighted power spectral density of the resampled $u'(t)$ as:

$$l_{peak,u} \equiv \frac{|\overline{u}|}{2\pi f_{peak,u}}. \tag{3.28}$$

The vertical length scale, $l_{peak,w}$, was determined from the power spectral density of w' analogously. Of a total of 1317 $l_{peak,u}$ measurements at $Re_{\langle s_n \rangle_A} > 105$, ten were discarded because they differed from the mean $l_{peak,u}$ for that ϕ by more than three standard deviations and three were discarded because a peak could not be identified in the frequency-weighted spectrum.

Alternatively, l_t can be estimated from the autocorrelation function of the local

velocity fluctuation as:

$$l_{corr,\ u} \equiv |\overline{u}| \int_0^{\tau_0} \frac{\overline{u'(t)u'(t+\tau)}}{\overline{u'^2}}\ \mathrm{d}\tau, \tag{3.29}$$

where τ is the time lag with respect to t and τ_0 is τ at the first zero-crossing. MATLAB's xcov.m function was used to calculate the variance-normalized auto-correlation function of each resampled $u'(t)$ record, from which the Eulerian integral length scale $l_{corr,u}$ [Eq. (3.29)] was calculated. Of a total of 1290 time records at $Re_{\langle s_n\rangle_A} > 105$ for which $l_{corr,u}$ could be computed, 22 were discarded because the calculated $l_{corr,u}$ deviated from the mean for that ϕ by more than three standard deviations.

The spatial heterogeneity of the velocity field is quantified by the spatial variance of $\overline{u}''(x,y) = \overline{u(x,y,t)} - \langle\overline{u}\rangle$ normalized by $\langle\overline{u}\rangle^2$. Time records at a given ϕ were divided into five or six subsets based on Q. $\langle\overline{u}''^2\rangle / \langle\overline{u}\rangle^2$ was then estimated for each (ϕ, Q) as the average $\overline{u}''^2/\langle\overline{u}\rangle^2 \approx (\overline{u} - U_p)^2/U_p^2$ of all time records in that subset.

Except in the sparsest arrays, measurements could not be collected across the entire width of the flume because cylinders obstructed the LDV laser beams. To permit sufficient sampling positions along each transect, gaps of normalized width $\Delta x_{gap}/\langle s_n\rangle_A = 1.4$ to 2.7, 0.0 to 0.4, and 3 to 6 were created in arrays of $\phi = 0.091$, 0.20, and 0.35, respectively (Table 3.1). To determine whether these gaps biased the results, velocity time records were collected along a lateral transect in a $\phi = 0.20$ array for a range of Δx_{gap}, from which lateral averages of $\overline{u}/U_p$, $\overline{w}/U_p$, $\overline{u'^2}/{U_p}^2$, $\overline{w'^2}/{U_p}^2$, $l_{peak,u}/d$, and $l_{peak,w}/d$ were calculated for each transect. The lateral averages, with the exception of $\langle\overline{w}/U_p\rangle$ and $\left\langle\overline{w'^2}/{U_p}^2\right\rangle$, remained within standard error of their respective values at $\Delta x_{gap}/\langle s_n\rangle_A = 0.2$ in the range $\Delta x_{gap}/\langle s_n\rangle_A = 0.2$ to 8.1 ± 0.4 (figure 3-2). The constant values suggest that our results were not biased by the gaps.

The duration of measurement at a single position was determined from the time taken for the time average and the variance, as defined by Eqs. (3.25) – (3.27), of preliminary velocity time records to converge to within 5% of their 20-minute average. This test was performed for each ϕ for several Re_d. The duration varied from 60 s to 1000 s, with lower Re_d generally requiring a longer time to converge.

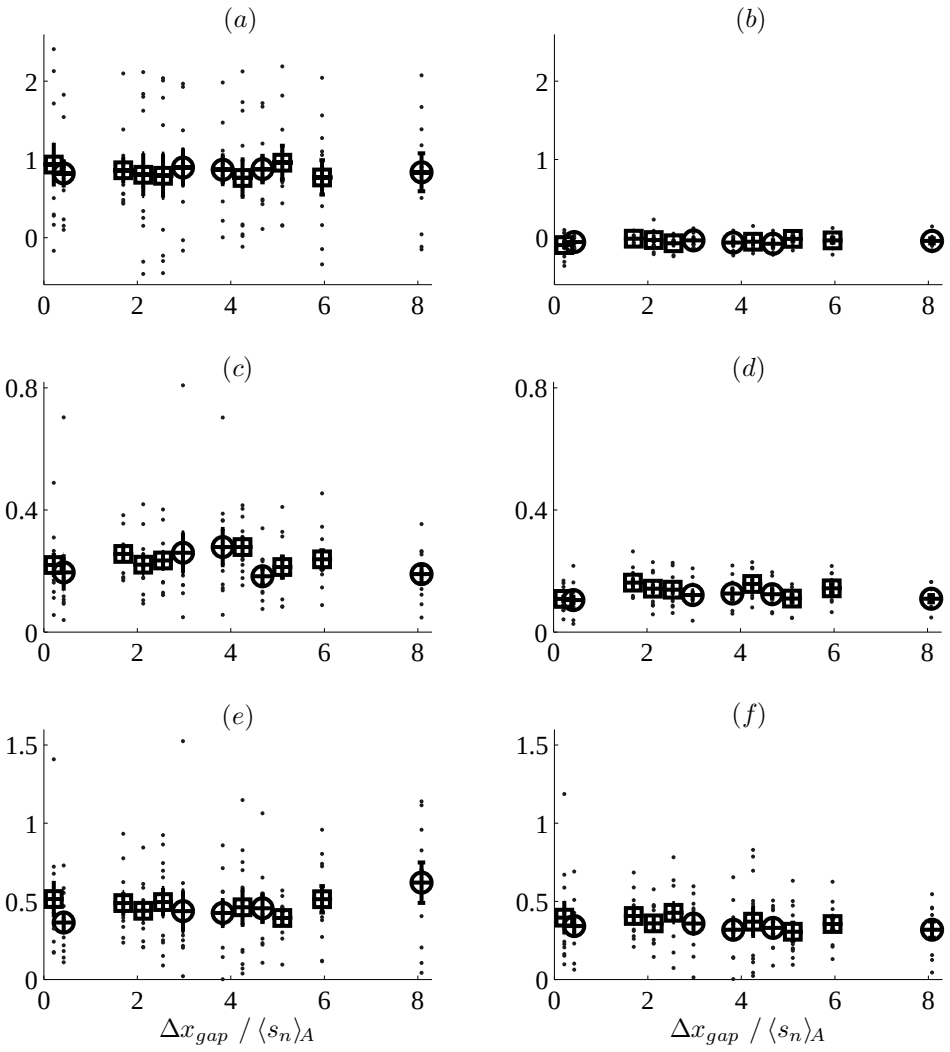

Figure 3-2: Sensitivity of (a) $\langle \overline{u}/U_p \rangle$, (b) $\langle \overline{w}/U_p \rangle$, (c) $\left\langle \overline{u'^2}/{U_p}^2 \right\rangle$, (d) $\left\langle \overline{w'^2}/{U_p}^2 \right\rangle$, (e) $\langle l_{peak,u} \rangle / d$, and (f) $\langle l_{peak,w} \rangle / d$, as defined by Eqs. (3.25) – (3.28), to Δx_{gap}, the width of the gap in the array at the sampling locations. Ten or eleven time records were collected at lateral intervals of $(s+d)/2$ along a single lateral transect in a $\phi = 0.20$ array for each Δx_{gap}. Dots represent the local values and open markers represent the lateral average over each transect. $\left(Re_d, Re_{\langle s_n \rangle_A}\right) = (430-480, 160-180)$ $(\circ)$ and $(470-540, 170-200)$ (square). Vertical bars indicate the standard error of the mean.

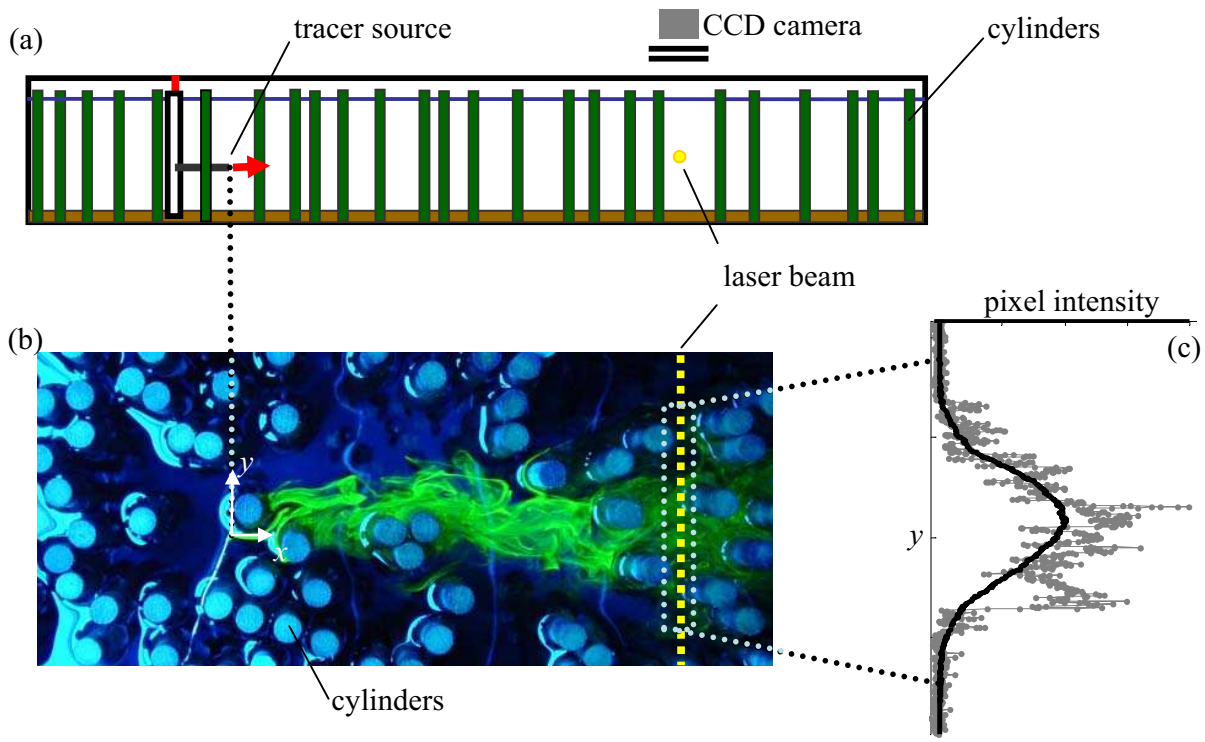

Figure 3-3: Side (a) and plan (b) view of the test section of the experimental setup. Mean flow $\langle \overline{u} \rangle$ is left to right. Pixel intensity was extracted along a lateral transect from each image [grey $\cdot$ in (c)] as a measure of the instantaneous concentration profile. The thick line in (c) is the temporally averaged profile.

3.3.2 Laser-induced fluorescence experiments

LIF was used to measure the lateral dispersion coefficient in a recirculating Plexiglas laboratory flume with a $(x \times y \times z) = 284$ cm $\times$ 40 cm $\times$ 43 cm working section. LIF measurements could not be collected in the same flume as the LDV measurements because the seeding material used in the latter would have interfered with the former. The use of the two flumes is justified because the spatially-averaged turbulence characteristics are determined by the macroscopic array properties and are not specific to the flume system, as demonstrated by the good agreement in $l_{peak,u}/d$ and mean turbulence intensity observed by White (2002) and in the present study (figures 3-9 and 3-12).

Dilute rhodamine WT was injected continuously from a horizontal needle with a syringe pump (Orion Sage^{TM} M362) at a rate that was matched visually with the local flow. A single horizontal beam of argon ion laser (Coherent INNOVA^{R} 70 ion

laser) passed laterally through the flume at a single streamwise position x downstream of the solute source (figure 3-3). A Sony CCD Firewire digital camera XCD-X710 controlled by Unibrain Fire-i 3.0 application captured the line of fluoresced solute from above the flume in a sequence of 1024×48 bitmap images. 530 nm and 515 nm long-pass filters (Midwest Optical Systems, Inc.) were attached to the camera to filter out the laser beam. Preliminary measurements confirmed that the recorded fluorescence intensity was linearly proportional to rhodamine WT concentration; for simplicity, the former was used in all analyses. The correct spatial scale on the images were determined from a photo of a ruler submerged horizontally in the position of the laser beam. The image of the ruler was taken every time the local water depth, the camera setting, or the position of the laser beam or the camera changed. At high ϕ, cylinders were removed to create the 1.3-cm gap in the array necessary to insert this ruler. This gap also ensured that the laser beam could pass through the entire width of the flume. The position of the laser beam relative to the solute source, which was restricted by the distance at which the solute reached the sidewalls, ranged from $x = 5$ cm to 143 cm. The time-averaged water depth at the longitudinal position of the laser beam ranged from 9.1 cm to 18.6 cm.

Instantaneous intensity profiles were extracted from the bitmap images, corrected for background and anomalous pixel intensities, and averaged over the duration of the experiment to yield a time-averaged intensity profile, $\overline{I(y,t)}$. The time-averaged profile was corrected for noise and background. Then, its variance was calculated as

$$\sigma_y^2(x) = \frac{m_2(x)}{m_0(x)} - \left[\frac{m_1(x)}{m_0(x)}\right]^2, \tag{3.30}$$

where $m_j(x)$ is the j^{th} moment,

$$m_j(x) = \int_{\kappa_2}^{\kappa_1} y^j \overline{I(y,t)}\, \mathrm{d}y. \tag{3.31}$$

The zeroth, first, and second moments and the corresponding σ_y were calculated by setting the limits of integration in Eq. (3.31), $\kappa_{1,2}$, at the two edges of the images.

Next, $\kappa_{1,2}$ were redefined as $\kappa_{1,2} = (m_1/m_0) \pm 3\sigma_y$ and the calculation was repeated. These limits were applied to prevent small fluctuations at large distances from the center of mass from increasing the variance estimate unrealistically.

The net lateral dispersion coefficient normalized by U_p and d for each ϕ was calculated as

$$\frac{K_{yy}}{U_p d} = \frac{1}{2d}\frac{\mathrm{d}\sigma_y^2}{\mathrm{d}x}, \tag{3.32}$$

where $\mathrm{d}\sigma_y^2/\mathrm{d}x$ is the gradient of the line of regression applied to all σ_y^2 measurements at $Re_{\langle s_n \rangle_A} > 53$ for $\phi = 0.35$ and at $Re_{\langle s_n \rangle_A} > 74$ for all other ϕ. The criterion for $\phi = 0.35$ is lower because the experimental setup could not accommodate the large longitudinal free surface gradient that results from the cylinder drag (Ch. 2) at $Re_{\langle s_n \rangle_A} > 70\,(Re_d > 400)$.

3.4 Experimental results

3.4.1 Flow visualization

We first consider the qualitative Reynolds number dependence. Figures 3-4 and 3-5 present unprocessed still photos taken in the $\phi = 0.010$ and 0.15 arrays, respectively, at four different Re_d. In figure 3-4, fluorescein solution was injected approximately 3.7 cm upstream of cylinder A. The injection point is visible at the top of the images in figure 3-5. The tracer emerges from the needle as a single distinct filament for all Re_d. In figure 3-5(a), the tracer is deflected by the cylinders and is advected through the array forming a streakline that is stationary in time. The flow is unsteady for all other conditions presented in figures 3-4 and 3-5 and, consequently, the angle at which the tracer encounters cylinders A and B in figure 3-4 and cylinder A in figure 3-5 varies with time. In both arrays, the Re_d dependence is qualitatively the same. The tracer forms distinct, thin ($\ll d$) bands of dyed and undyed fluid at $Re_d \approx 30$ [figures 3-4(a) and 3-5(a)]. At higher Re_d, turbulent eddies rapidly mix the fluid within the pores, resulting in a more spatially-uniform distribution. For example, distinct filaments cannot be distinguished at the bottom of the image in figures 3-4(d) and 3-5(d).

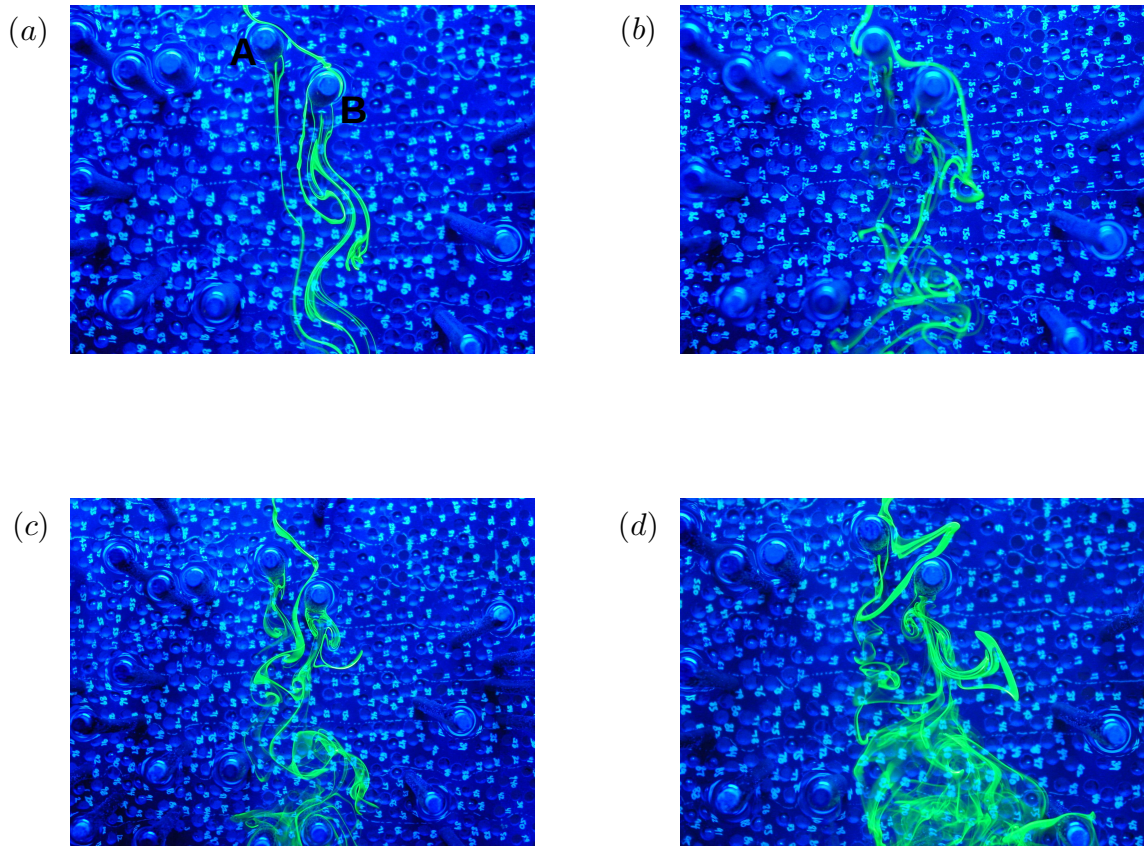

Figure 3-4: Flow visualization using fluorescein and blue lighting in a $\phi = 0.010$ array at $Re_d = (a)\ 28 \pm 1$, $(b)\ 56 \pm 3$, $(c)\ 78 \pm 3$, and $(d)\ 113 \pm 5$. These values correspond to $Re_{\langle s_n \rangle_A} = 99 \pm 5$, 200 ± 9, 270 ± 10, and 400 ± 20, respectively. Mean flow is from top to bottom. Camera and dye injection position were fixed. The injection point is approximately 3.7 cm upstream of cylinder A.

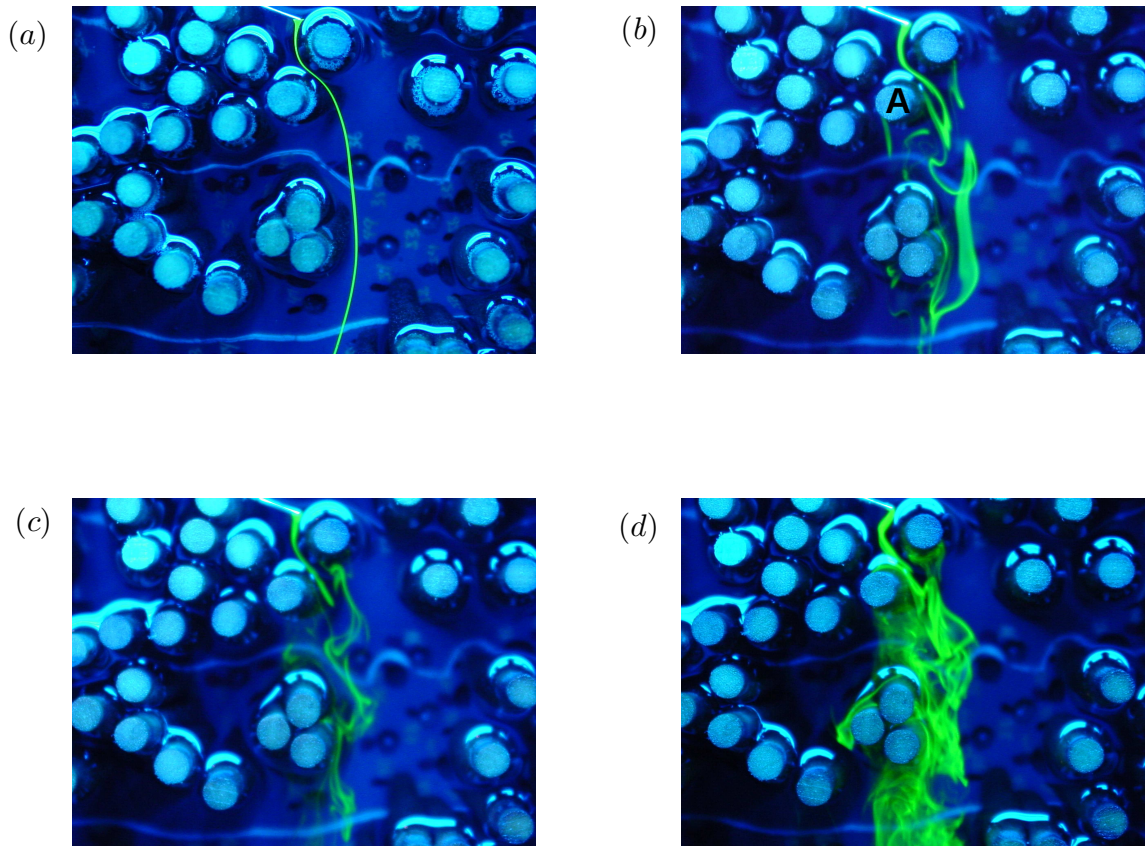

Figure 3-5: Flow visualization using fluorescein and blue lighting in a $\phi = 0.15$ array at Re_d =(a) 32 ± 2, (b) 73 ± 3, (c) 108 ± 4, and (d) 186 ± 7. These values correspond to $Re_{\langle s_n \rangle_A} = 16.0 \pm 0.8$, 36 ± 2, 53 ± 2, and 92 ± 4, respectively. Mean flow is from top to bottom. Camera and dye injection position were fixed.

The $\phi = 0.010$ array is sufficiently sparse that individual vortex streets and their interactions can be identified. A laminar vortex street is seen behind cylinder B at $Re_d = 28 \pm 1$ [figure 3-4(a)]. In contrast, a pair of standing eddies are attached to cylinder A in the same image. Here, tracer emerges $O(d)$ downstream of the cylinder as a single, straight filament. The difference between the wakes of cylinders A and B can be attributed to differences in the local flow conditions due to the random nature of the cylinder distribution. At an isolated cylinder, standing eddies form at $Re_d \approx 5$ and become unsteady at $Re_d \approx 40$ (Lienhard, 1966). In figure 3-4(a), $Re_d = 28 \pm 1$, and an isolated wake is expected to be steady. The presence of neighboring cylinders may have elevated the local Re_d such that flow around cylinder B enters the unsteady regime. Figure 3-4(a) also highlights the interaction of the wakes. The single tracer filament leaving cylinder A is drawn into the vortex street of cylinder B as it propagates downstream. At $Re_d = 78 \pm 3$, cylinders A and B both shed vortices [figure 3-4(c)]. Moreover, the shedding is in phase, indicating wake interaction. Here, the center-to-center distance between cylinders A and B is approximately $4d$, and the occurrence of wake interaction is consistent with Eq. (3.22). The vortex street from the two cylinders appears to merge and form a single turbulent street at approximately $x \approx 15d$. This is consistent with Williamson (1985)'s observations of in-phase vortex shedding behind a pair of side-by-side cylinders. A similar merging of vortex streets can be identified downstream of four cylinders in a square configuration at a 45° angle to the flow (Lam et al., 2003, figure 9, $Re_d = 200$).

3.4.2 Velocity and turbulence structure

Local velocity varies dramatically in the horizontal plane due to the random configuration of the cylinders. This is highlighted in figure 3-6, in which each subplot presents lateral transects of time-averaged and turbulent components of velocity, normalized by U_p, at a single longitudinal position. For example, the time average of the longitudinal component of velocity ($\overline{u}$) deviates dramatically from its cross-sectional average (U_p) at all ϕ and Re_d. Indeed, $\overline{u}$ is negative at certain positions in the array because of recirculation zones that develop immediately downstream of a cylinder

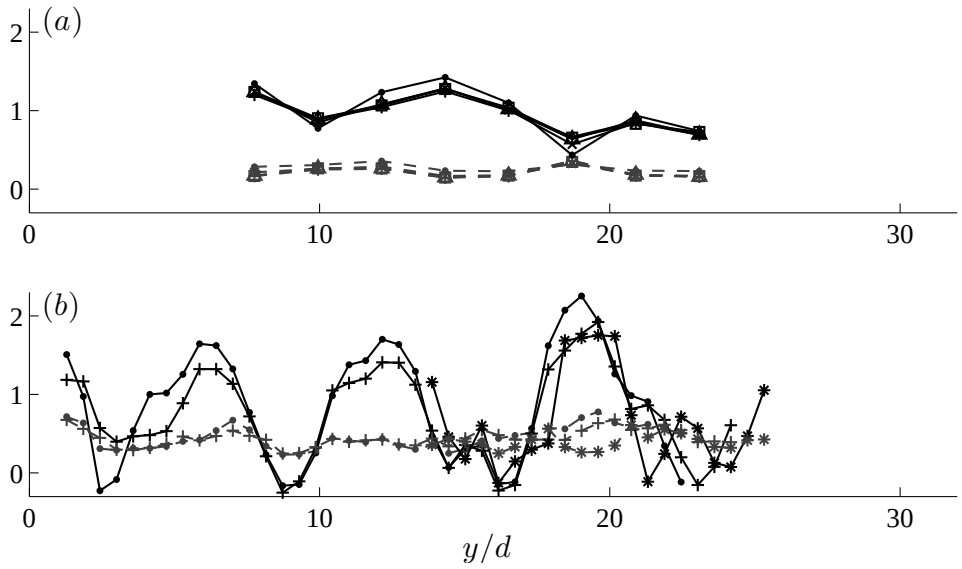

Figure 3-6: Lateral transects of $\overline{u}/U_p$ (solid line) and $\sqrt{k_t}/U_p$ (grey, dashed line) at (a) $\phi = 0.010$, $Re_d = 81-89$ $(\cdot)$, $210-220$ $(\times)$, $310-330$ (Δ), $350-370$ (square), and $400-420$ $(+)$ and at (b) $\phi = 0.15$, $Re_d = 99-110$ $(\cdot)$, $310-330$ $(+)$, and $400-460$ $(*)$. These values correspond to $Re_{\langle s_n \rangle_A} = 280-310$, $730-770$, $1100-1200$, $1200-1300$, and $1400-1500$ for (a) and $Re_{\langle s_n \rangle_A} = 49-55$, $150-160$, and $200-230$ for (b). Flume sidewalls were at $y = 0$ and $32.0d$.

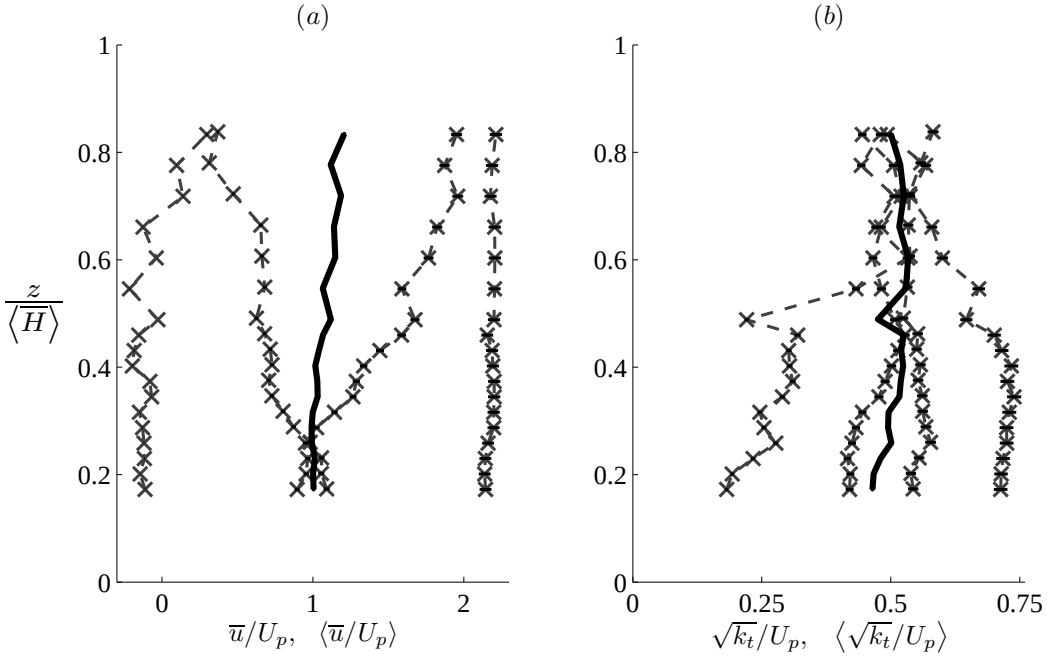

Figure 3-7: Vertical profiles of (a) $\overline{u}/U_p$ and (b) $\sqrt{k_t}/U_p$ at four positions, $1.0d$ apart, along a lateral transect $(\times)$. The lateral average of the four profiles is presented as a thick solid line. Horizontal bars reflect the uncertainty in U_p. $\phi = 0.20$, $\left(Re_d, Re_{\langle s_n \rangle_A}\right) = (440-490, 160-180)$, $\left\langle \overline{H} \right\rangle = 17.3-17.4$ cm.

[figure 3-6(b)]. A comparison of lateral profiles at different Re_d at the same position in the array indicates that the shape of the lateral profiles remains constant as Re_d varies (figure 3-6), confirming that the spatial variability is largely dictated by the cylinder configuration. Because the array is vertically uniform, vertical variations in the time-averaged velocity and turbulence intensity are expected to be smaller than their lateral heterogeneity. In particular, spatial averages $\langle \overline{u}/U_p \rangle$ and $\langle \sqrt{k_t}/U_p \rangle$ are approximately uniform in depth (solid lines in figure 3-7). Similar observations were made in random arrays of $\phi = 0.010$, 0.020, and 0.063 by White and Nepf (2003). Finally, note that the spatial variability is smaller in figure 3-6(a) ($\phi = 0.010$) than in figure 3-6(b) ($\phi = 0.15$). Indeed, $\langle \overline{u}'' \rangle^2 / \langle \overline{u} \rangle^2$ increases with increasing ϕ at a given Re_d (Appendix I).

The frequency-weighted power spectral density and the autocorrelation function of selected $u'(t)$ records are presented in figure 3-8 for reference. Like $\overline{u}$ and $\sqrt{k_t}$, the power spectrum and the autocorrelation function vary dramatically in the horizontal plane, and these plots should not be interpreted as typical profiles. Note that the autocorrelation function in (a) appears oscillatory with a period of about 1 s, which indicates that this particular $u'(t)$ time record contains a periodic component.

The two methods for estimating the integral length scale yield similar values (figure C-1). Therefore, only $\langle l_{peak,u}/d \rangle$ ($\circ$) is compared with the scale model Eq. (3.15) here (figure 3-9). Note that each $\cdot$ in figure 3-9 represents a single time record; the spread of the data at each ϕ reflects the spatial heterogeneity of the local velocity. The measured integral length scale generally decreases with increasing $d/\langle s_n \rangle_A$, as demonstrated by $\langle l_{peak,u}/d \rangle$, where the spatial average was calculated as the mean of all LDV measurements at $Re_{\langle s_n \rangle_A} > 105$ at each ϕ. Equation (3.15) captures this decrease of $\langle l_{peak,u}/d \rangle$ reasonably well for $d/\langle s_n \rangle_A \geq 1.3$. As expected from Eq. (3.15), the mean of $\langle l_{peak,u}/d \rangle$ for $d/\langle s_n \rangle_A < 0.5$ is 1.0. However, $\langle l_{peak,u}/d \rangle$ decreases with increasing $d/\langle s_n \rangle_A$ below $d/\langle s_n \rangle_A = 1$ in both the present study and in White (2002)'s experiments. Additional measurements are necessary to verify Eq. (3.15) for $d/\langle s_n \rangle_A < 1$.

The mean turbulence intensity at a given ϕ, $\langle \sqrt{k_t}/U_p \rangle$, is calculated as the gradient of the line of regression of all LDV measurements of $\sqrt{k_t}$ on U_p for $Re_{\langle s_n \rangle_A} > 105$ at

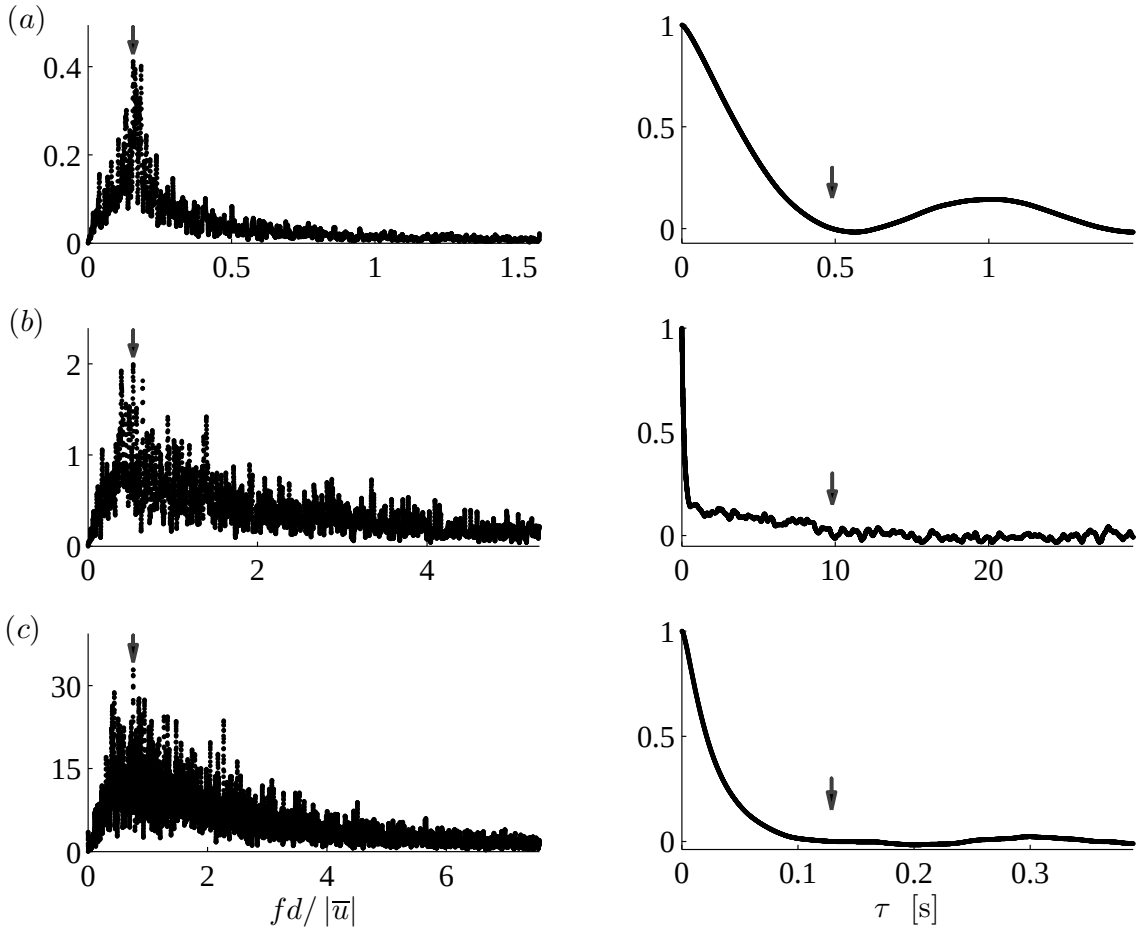

Figure 3-8: The frequency-weighted power spectral density [cm^2 s^{-2}] (left) and the variance-normalized autocorrelation function (right) of selected u' time records. (a) $\phi = 0.010$, $\overline{u} = 3.8$ cm s^{-1}, $Re_d = 350$, $Re_{\langle s_n \rangle_A} = 1200$, (b) $\phi = 0.20$, $\overline{u} = -1.4$ cm s^{-1}, $Re_d = 320$, $Re_{\langle s_n \rangle_A} = 120$, and (c) $\phi = 0.35$, $\overline{u} = 4.9$ cm s^{-1}, $Re_d = 770$, $Re_{\langle s_n \rangle_A} = 130$. Arrows ($\downarrow$) mark the identified peak in the frequency-weighted power spectral density (left) and τ_0 (right). f denotes frequency.

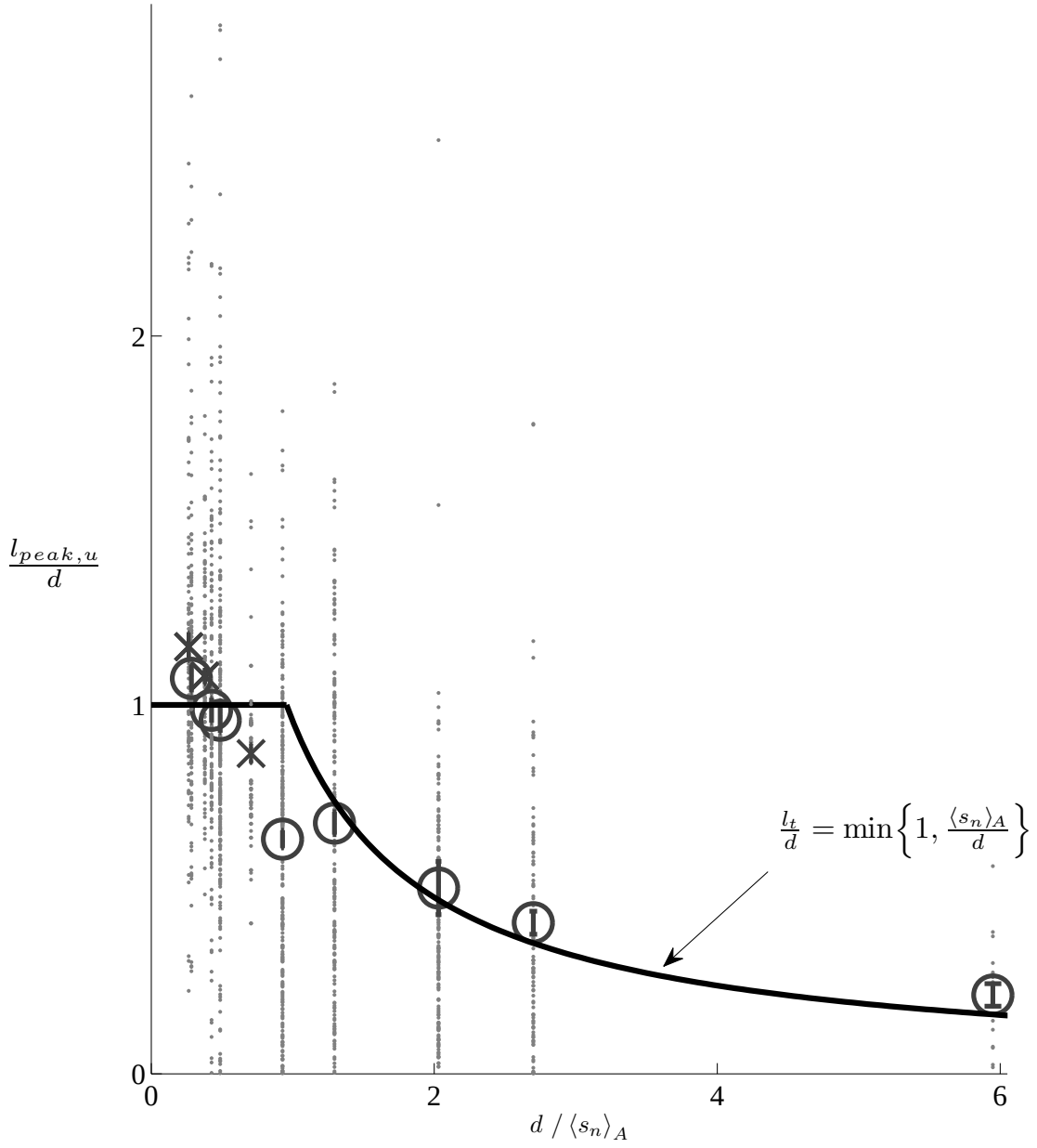

Figure 3-9: $l_{peak,u}/d$ as defined by Eq. (3.28) ($\cdot$) for LDV measurements at $Re_{\langle s_n \rangle_A} > 105$. Each $\cdot$ in figure 3-9 represents a single time record. Circles mark the mean and vertical bars represent the standard error of the data from the present study for each ϕ. The solid line is Eq. (3.15). There are data points at $(d/\langle s_n \rangle_A, l_{peak,u}/d) = (0.49, 5.34)$ and $(2.0, 13.6)$ which are not visible in the figure but are included in the calculation of the mean. White (2002)'s ADV measurements for $Re_{\langle s_n \rangle_A} > 105$ are also included ($\cdot$) with their mean ($\times$) and standard error (power spectral density data provided by B. L. White, personal comm.).

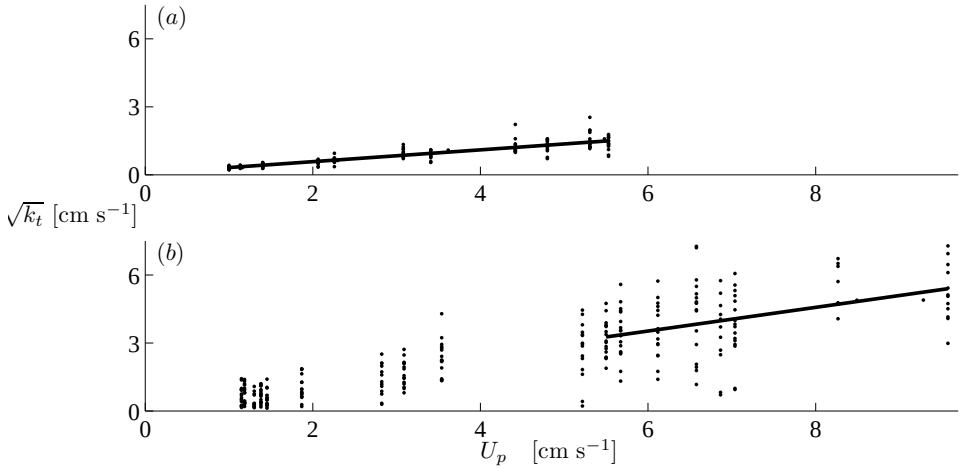

Figure 3-10: All LDV measurements of $\sqrt{k_t}$ for $\phi = (a)$ 0.020 and (b) 0.35. Each $\cdot$ represents a single time record at one location within the array and the associated U_p. The solid line in each subplot is the least-squares fit to all data in the range (a) $Re_{\langle s_n \rangle_A} > 105$ and (b) $Re_{\langle s_n \rangle_A} > 70$. See Table 3.2 for the equations for the fitted lines.

ϕ	line of regression of $\sqrt{k_t}$ on U_p	R	n	Re_d
0.010	$(0.07 \pm 0.06) + (0.21 \pm 0.02)U_p$	0.77	118	$57 - 380$
0.020	$(0.06 \pm 0.04) + (0.26 \pm 0.01)U_p$	0.88	147	$61 - 380$
0.031	$(0.02 \pm 0.05) + (0.30 \pm 0.01)U_p$	0.81	261	$67 - 430$
0.060	$(-0.0 \pm 0.1) + (0.38 \pm 0.02)U_p$	0.73	260	$130 - 370$
0.091	$(0.1 \pm 0.1) + (0.37 \pm 0.02)U_p$	0.80	191	$200 - 540$
0.15	$(0.0 \pm 0.3) + (0.43 \pm 0.05)U_p$	0.53	195	$220 - 460$
0.20	$(0.3 \pm 0.5) + (0.47 \pm 0.09)U_p$	0.43	136	$280 - 540$
0.35	$(0.4 \pm 0.7) + (0.52 \pm 0.10)U_p$	0.44	116	$430 - 770$

Table 3.2: The equation of the least-squares fit to data at mean $Re_{\langle s_n \rangle_A} > 105$ ($\phi = 0.010 - 0.20$) or at mean $Re_{\langle s_n \rangle_A} > 70$ ($\phi = 0.35$). R is the correlation coefficient and n is the total number of data points included in the regression. See Table 3.1 for the corresponding $d/\langle s_n \rangle_A$.

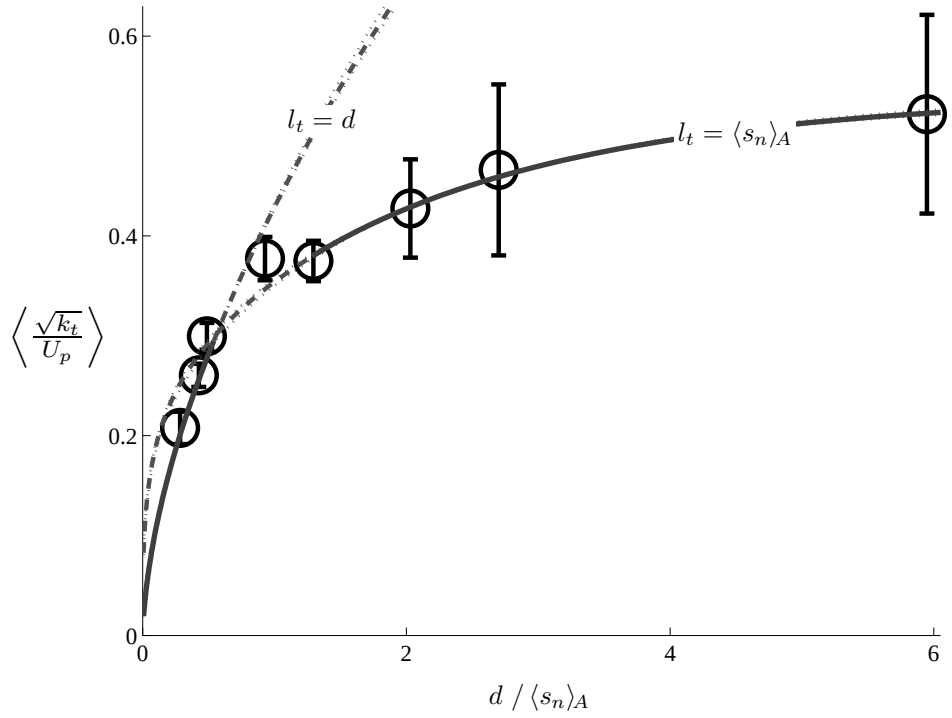

Figure 3-11: The gradient of the line of regression of $\sqrt{k_t}$ on U_p at $Re_{\langle s_n \rangle_A} > 105$ for $\phi < 0.35$ and $Re_{\langle s_n \rangle_A} > 70$ for $\phi = 0.35$ from this thesis only. Vertical bars represent the uncertainty in the gradient as defined by Eq. (F.1). Solid lines are Eq. (3.33); the empirical fits are extrapolated over the range of the data set (dashed). Dotted lines reflect the uncertainty in C_D^{form}: the lines are Eq. (3.14) with the upper and lower estimates of C_D^{form} in Eq. (3.12) and the corresponding best-fit scaling constants 0.84 and 0.94 for $l_t = \langle s_n \rangle_A$ and 1.00 and 1.17 for $l_t = d$, respectively.

$\phi < 0.35$ and for $Re_{\langle s_n \rangle_A} > 70$ at $\phi = 0.35$. The $Re_{\langle s_n \rangle_A}$ ranges fall within those for which $K_{yy}/(U_p d)$ is calculated (§ 3.3.2). The observed correlation is highly significant for all ϕ (Table 3.2), indicating that $\langle \sqrt{k_t}/U_p \rangle$ is independent of Re_d under these conditions. $\sqrt{k_t}$ measurements and the corresponding line of best-fit for $\phi = 0.020$ and 0.35 are presented as examples in figure 3-10. Despite the large spatial heterogeneity in individual (local) $\sqrt{k_t}/U_p$ estimates, their spatial average increases monotonically with ϕ, within uncertainty (figure 3-11).

The scaling constants for the turbulence intensity scale Eq. (3.14) were determined by least-squares fitting Eq. (3.14), with l_t defined by Eq. (3.15), to the $\langle \sqrt{k_t}/U_p \rangle$ measurements presented in figure 3-11. The data point at $d/\langle s_n \rangle_A = 0.93$ was excluded from the fitting because it is near the expected transition in l_t, i.e., $d/\langle s_n \rangle_A = 1$.

Further, to avoid discontinuities in the model predictions, we will assume that the transition between the two regimes occurs at $d/\langle s_n \rangle_A = 0.56$, where the two functions intersect, i.e.,

$$\left\langle \frac{\sqrt{k_t}}{U_p} \right\rangle = \begin{cases} (1.07 \pm 0.09) \left[C_D^{\text{form}} \frac{\phi}{(1-\phi)\pi/2} \right]^{1/3}, & d/\langle s_n \rangle_A < 0.56 \\ (0.88 \pm 0.02) \left[C_D^{\text{form}} \frac{\langle s_n \rangle_A}{d} \frac{\phi}{(1-\phi)\pi/2} \right]^{1/3}, & d/\langle s_n \rangle_A \geq 0.56 \end{cases}, \tag{3.33}$$

where C_D^{form} is described by Eq. (3.12). The uncertainty in the scaling constants is the 95% confidence interval. The theory accurately captures the ϕ dependence of the measured $\langle \sqrt{k_t}/U_p \rangle$ for both $d/\langle s_n \rangle_A < 0.49$ and ≥ 1.3 (figure 3-11). Note that the measurement at $d/\langle s_n \rangle_A = 0.93$ falls between the extrapolation of the two expressions in Eq. (3.33), suggesting transition effects.

Field measurements by Neumeier and Amos (2006), Nikora (2000), and Leonard and Luther (1995), presented in figure 3-12, fall within the range of $\sqrt{k_t}/U_p$ observed in the present study. To the authors' knowledge, these are the only field reports in which both turbulence measurements and stem density are presented for emergent plant canopies. $\langle \sqrt{k_t}/U_p \rangle$ calculated from White (2002)'s three-dimensional acoustic Doppler velocimeter (ADV) measurements are also presented in figure 3-12 for comparison. The good agreement between Eq. (3.33) and laboratory data suggests that mean turbulence intensity at high Re_d can be predicted in random cylinder arrays from $d/\langle s_n \rangle_A$, ϕ, and C_D^{form}.

3.4.3 Net lateral dispersion

The lateral variance of the time-averaged concentration distribution $\left(\langle \sigma_y^2 \rangle\right)$, hence $\mathrm{d}\langle \sigma_y^2 \rangle / \mathrm{d}x$, measured at a fixed longitudinal distance from the source at $Re_{\langle s_n \rangle_A} > 74$ is independent of Re_d (e.g., figure 3-13; Appendix A; see Table 3.3 for exact range in Re_d that were considered at a given ϕ). Such Re_d independence is expected in fully turbulent conditions, defined here to refer to high Re_d flows in which turbulence properties are Re_d independent. Following the Re_d independence of measured l_t (at $\phi \geq 0.031$) and $\left\langle \sqrt{k_t}/\langle \overline{u} \rangle \right\rangle$ at similar Re_d, this Re_d independence of $\langle \sigma_y^2 \rangle$ is interpreted

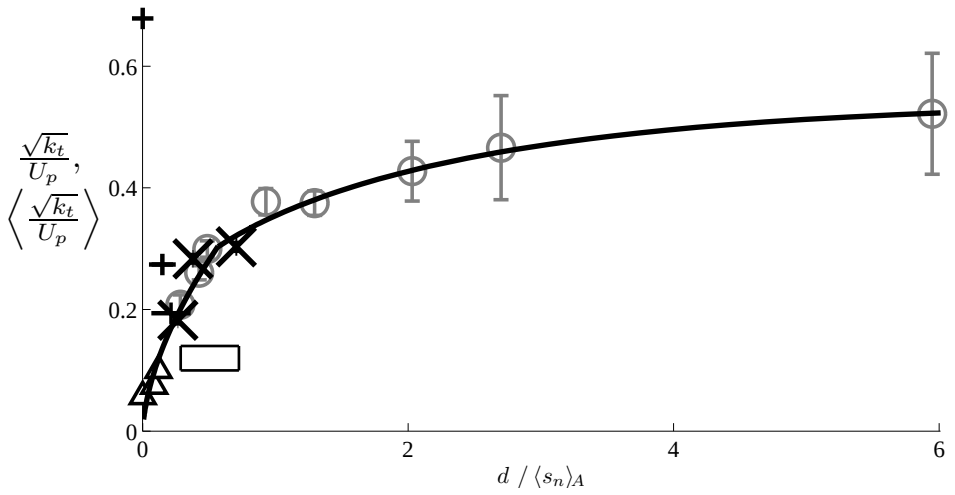

Figure 3-12: $\langle \sqrt{k_t}/U_p \rangle$ calculated from LDV measurements collected in the present study ($\circ$) and from White (2002)'s measurements at $\phi = 0.010$, 0.020, and 0.063 ($\times$) (lateral profiles of $\sqrt{\overline{u'^2}}, \sqrt{\overline{v'^2}}, \sqrt{\overline{w'^2}}$, and $\overline{u}$ were provided by B. L. White, personal comm.). Vertical bars represent the uncertainty in the gradient as defined by Eq. (F.1). Field measurements of $\sqrt{k_t}/U_p$ in emergent plant canopies by Nikora (2000, $\triangle$), Leonard and Luther (1995, +), and Neumeier and Amos (2006, unpublished values and details provided by U. Neumeier, personal comm., rectangle) are also plotted. U. Neumeier provided eight depth-profiles of $(\sqrt{\overline{u'^2}}, \sqrt{\overline{v'^2}}, \sqrt{\overline{w'^2}})$ in emergent canopies, but only the profile where the estimated wind-induced horizontal and vertical wave speeds were less than 50% of the reported r.m.s. speeds (profile $H21$) is included here. The vertical range of the box marks the minimum and maximum values in that profile. The horizontal range in Leonard and Luther (1995) and Neumeier and Amos (2006)'s data represents that in the mean stem d reported in the studies. An exactly random distribution was assumed in calculating $\langle s_n \rangle_A$ for the field data from Eq. (D.10). Solid line is Eq. (3.33).

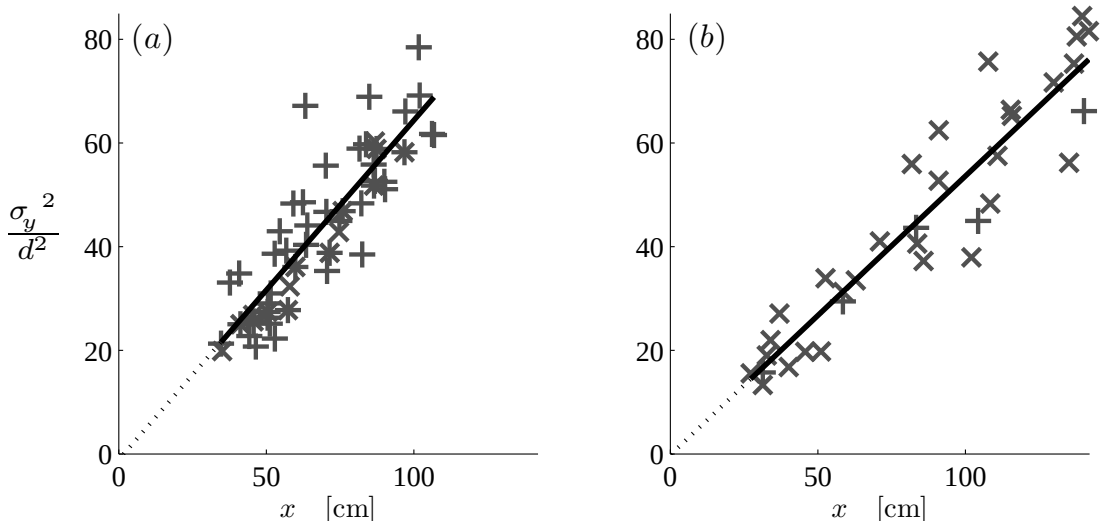

Figure 3-13: $\sigma_y^2(x)$ for (a) $Re_d = 83-84$ $(\times)$, $120-130$ $(+)$, and $180-190$ $(*)$ in a $\phi = 0.010$ array and (b) $Re_d = 190-210$ $(\times)$ and $340-370$ $(+)$ in a $\phi = 0.15$ array. These values correspond to $Re_{\langle s_n \rangle_A} = 290-300$, $420-450$, and $640-660$ for (a) and $Re_{\langle s_n \rangle_A} = 94-100$ and $170-180$ for (b). Solid line represents the linear regression on all $Re_{\langle s_n \rangle_A} > 74$ data; dotted line is its extrapolation to smaller x. Note that the best-fit lines were not forced through $\left(x, \sigma_y^2/d^2\right) = (0,0)$.

to be due to fully turbulent conditions.

The assumption that net lateral dispersion becomes Fickian at large x is confirmed by the linear increase of σ_y^2 with x observed at all ϕ (e.g., figure 3-13). At each ϕ, the linear correlation coefficient for all (x, σ_y^2) measurements at $Re_{\langle s_n \rangle_A} > 74$ is highly significant, suggesting that all measurements at $Re_{\langle s_n \rangle_A} > 74$ were collected within the asymptotic dispersion regime (see Table 3.3 for corresponding range in x). By analogy with turbulent diffusion, $\mathrm{d}\sigma_y^2/\mathrm{d}x$ is not expected to reach its asymptotic limit until the solute particles have dispersed over distances substantially larger than the distance over which velocity is correlated. Accordingly, close to the solute source, $\sigma_y^2(x)$ is expected to deviate from the line of regression of $\sigma_y^2(x)$ on x in the asymptotic regime (e.g., solid line in figure 3-13). However, the extrapolation of the line of regression coincides with $\left(x, \sigma_y^2/d^2\right) = (0,0)$ within uncertainty at all $\phi \leq 0.27$, which suggests that lateral dispersion in the high Reynolds number regime becomes asymptotic at a very short advective distance. In Ch. 4, it will be shown that the distance required to achieve asymptotic dispersion increases as Re_d decreases below fully turbulent

conditions in dense ($\phi = 0.20, 0.35$) arrays.

The normalized coefficients for net asymptotic lateral dispersion $K_{yy}/(U_p d)$ are presented in figures 3-14 and 3-15 and in Table 3.3. The figures include measurements at $\phi = 0$ reported by Nepf et al. (1997, Table 1). Three distinct regimes can be identified in the figures. In the sparse array, $K_{yy}/(U_p d)$ increases rapidly as ϕ and $d/\langle s_n \rangle_A$ increase. In the present laboratory study, this regime extends from $d/\langle s_n \rangle_A = 0$ to 0.58 ($\phi = 0 - 0.031$). In the intermediate range, $K_{yy}/(U_p d)$ decreases as ϕ increases. This regime extends from $d/\langle s_n \rangle_A = 0.58$ to 2.7 ($\phi = 0.031 - 0.20$) in our arrays. Finally, in the densest arrays, $K_{yy}/(U_p d)$ again increases with ϕ, but more gradually. To the authors' knowledge, this ϕ dependence of lateral dispersion over one order of magnitude range of ϕ has not been documented previously.

Nepf et al. (1997)'s measurements of $K_{yy}/(U_p d)$ in periodic, staggered cylinder arrays at $Re_{\langle s_n \rangle_A} > 1700$[c] are included in figure 3-14 (+) for the purpose of qualitative comparison only. Only measurements for which the exact cylinder configuration is available (see Zavistoski, 1994) are presented. It should be noted that Nepf et al. (1997)'s measurements do not represent a dispersion phenomenon analogous to the one investigated in the present study. In their experiments, solute was injected 54 cm upstream of the array (Sullivan, 1996). It is not obvious how end effects (i.e., the effects of being transported in non-fully-developed flow) influence the dispersion coefficient. Also, the nearest neighbor spacing was anisotropic in Nepf et al. (1997)'s arrays, and $\langle s_n \rangle_A$ may not be the appropriate length scale.

Models proposed by Nepf (1999) and Koch and Brady (1986) are compared with experiment in figure 3-14. Nepf (1999)'s model for turbulent diffusion [Eq. (3.6)] is consistent with the qualitative trend observed in the sparse array regime ($\phi \leq 0.031$). However, the model does not capture the decrease in $K_{yy}/(U_p d)$ observed from $d/\langle s_n \rangle_A = 0.58$ to 2.7 and, consequently, overpredicts $K_{yy}/(U_p d)$ above $d/\langle s_n \rangle_A = 0.58$. Note that Eq. (3.6) is equivalent to assuming that the product of $\langle l_e \rangle_m / d$ and the effective porosity, V_m/V, in Eq. (3.17) is constant for all ϕ. Consequently,

[c] In calculating this value, $\langle s_n \rangle_A$ was taken as the minimum distance between cylinders in any direction.

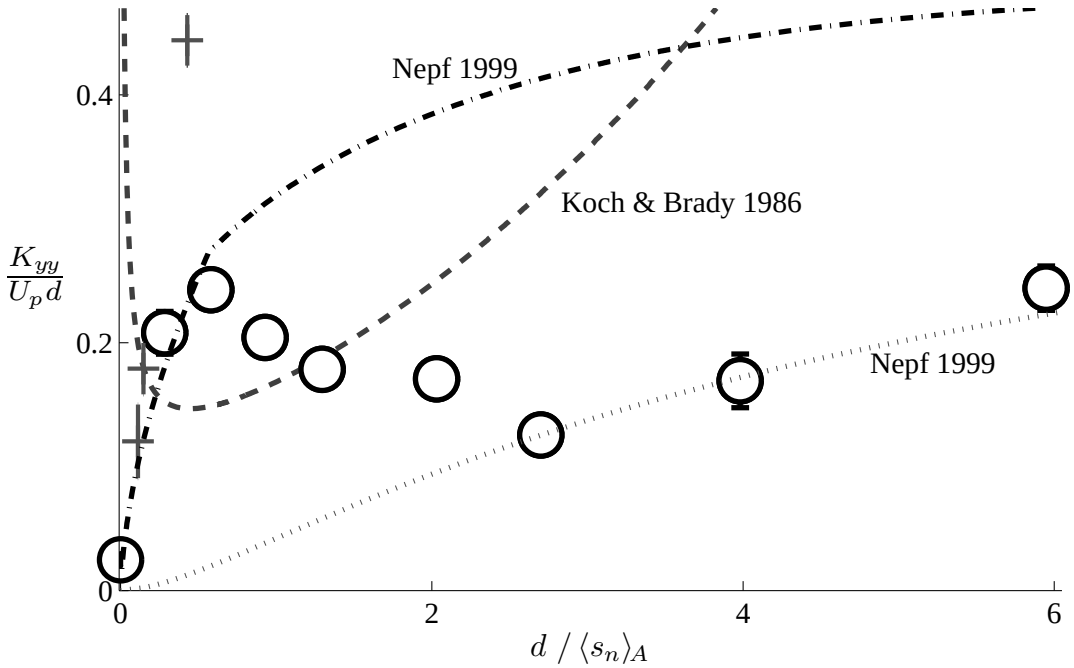

Figure 3-14: Comparison of observed $K_{yy}/(U_p d)$ ($\circ$) with Eq. (3.6) (dash-dotted), Eq. (3.19) (dotted), and Eq. (3.20) (dashed). $\left\langle \sqrt{k_t}/U_p \right\rangle$ in Eq. (3.6) is predicted by Eq. (3.33). $\epsilon = d$ in Eq. (3.19), as proposed by Nepf (1999). $k_\perp$ in Eq. (3.20) is predicted for the arrays used in our experiments as described in Appendix E. $K_{yy}/(U_p d)$ at $\phi = 0$ is taken from Nepf et al., 1997, Table 1. Also represented are Nepf et al. (1997)'s measurements in periodic staggered arrays of $d = 0.6$ cm, $\phi = 0.0046$, 0.014, and 0.055 at $Re_{\langle s_n \rangle_A} > 1700$. The marker (+) indicates their mean. For the periodic array, $\langle s_n \rangle_A$ was taken as the minimum distance between cylinders in any direction. Vertical bars on our data represent uncertainty in the gradient of the linear regression of the variance data, as defined by Eq. (F.1). Vertical bars on Nepf et al. (1997)'s data indicate the quadratic sum of the standard error and the mean of the experimental uncertainty associated with each measurement. Where vertical bars are not visible, they are smaller than the size of the marker.

Eq. (3.6) predicts that turbulent diffusion will grow monotonically with $d/\langle s_n \rangle_A$. In contrast, $(\langle l_e \rangle_m / d)(V_m/V)$ decreases monotonically as ϕ increases in our formulation [Eq. (3.18)], which permits a description of turbulent diffusion that decreases with increasing $d/\langle s_n \rangle_A$ for $d/\langle s_n \rangle_A > 0.56$ (dash-dotted line in figure 3-15).

At high ϕ ($\geq$ 0.20), where physical reasoning suggests that dispersion due to the spatially-heterogeneous velocity field is most important, Nepf (1999)'s random walk model [Eq. (3.19) with $\epsilon = d = 0.64$ cm] yields good quantitative agreement with the data. While Koch and Brady (1986)'s Stokes flow solution [Eq. (3.20)] predicts the correct qualitative trend at $\phi \geq 0.20$, the quantitative agreement with the experiment is poor: the solution dramatically overpredicts our measurements at $\phi = 0.20$, 0.27, and 0.35. Also, Eq. (3.20) predicts a rapidly-increasing contribution as ϕ decreases below $d/\langle s_n \rangle_A = 0.44$ (figure 3-14). The laboratory data exhibit the opposite trend, with $K_{yy}/(U_p d)$ decreasing as $d/\langle s_n \rangle_A$ decreases below 0.58. In the proposed modification [Eq. (3.22)], Eq. (3.20) is multiplied by $P_{s_{nc}<5d}$, the probability that a single cylinder in the array will have a nearest neighbor within $r = 5d$. $P_{s_{nc}<5d}$ monotonically decreases to zero as ϕ decreases to zero, which also allows Eq. (3.22) to remain finite.

The linear superposition of models describing the contributions of turbulence and the spatially-heterogeneous velocity field to net dispersion [Eqs. (3.23), (3.24); $\epsilon = d$, $r^*/d = 2$] is compared with experiment in figure 3-15. Recall that r^* is the minimum center-to-center separation between neighboring cylinders necessary for the fluid between them to contain eddies with mixing length scale $l_e \geq d$. Here, we anticipated that $l_e = l_t$ and imposed $r^*/d = 2$. The best-fit scaling constants $\gamma_1 = 4.0$ and $\gamma_2 = 0.34$ were determined by substituting Eq. (3.33) and $r^*/d = 2$ into Eq. (3.24) and fitting the resulting expression, in the least-squares sense, to the observed $K_{yy}/(U_p d)$ for $\phi > 0$. Because the two expressions for dispersion due to the spatially-heterogeneous velocity field [Eqs. (3.19) and (3.22)] have a similar dependence on ϕ at large ϕ, Eq. (3.23) yields comparable agreement to data (dotted line). The corresponding scaling constant for the turbulent diffusion model is $\gamma_1 = 4.5$. The proposed model for net dispersion captures the three observed regimes. Some

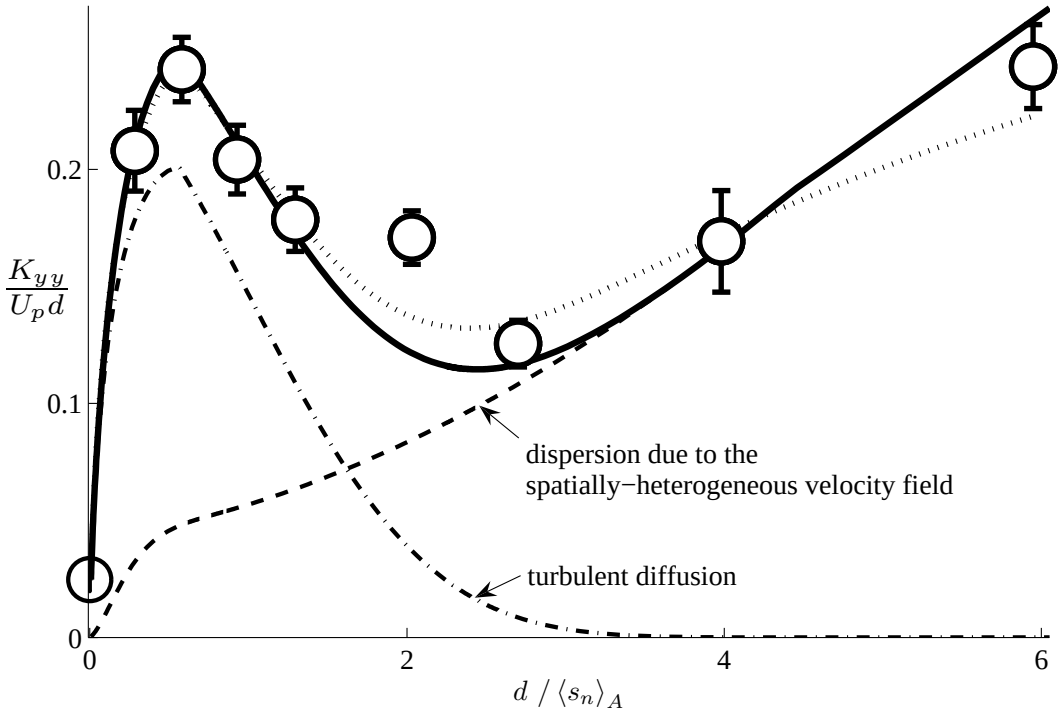

Figure 3-15: Comparison of the observed $K_{yy}/(U_p d)$ ($\circ$) with the theory. $K_{yy}/(U_p d)$ at $\phi = 0$ is taken from Nepf et al., 1997, Table 1. Solid line is Eq. (3.24), with scaling constants $\gamma_1 = 4.0$ and $\gamma_2 = 0.34$, as determined from least-squares fitting to data. $\langle \sqrt{k_t}/U_p \rangle$ in Eq. (3.24) is predicted by Eq. (3.33). The two terms that constitute Eq. (3.24) – Eq. (3.22) (dashed) and Eq. (3.18) (dashed-dotted) – are also presented. Dotted line is Eq. (3.23); $\epsilon = d$ was imposed and the scaling constant $\gamma_1 = 4.5$ was determined from least-squares fitting to data. Vertical bars for $\phi > 0$ represent uncertainty in the gradient of the linear regression of the variance data, as defined by Eq. (F.1). The vertical bar on Nepf et al. (1997)'s data point ($\phi = 0$) indicate the quadratic sum of the standard error and the mean of the experimental uncertainty associated with each measurement. Where the vertical bars are not visible, they are smaller than the marker.

disagreement between theory and experiment occurs at $d/\langle s_n \rangle_A = 2.0$ ($\phi = 0.15$), suggesting non-linear interactions between the two components of lateral dispersion at this $d/\langle s_n \rangle_A$. Note that Eq. (3.24) suggests that the contribution from the spatially-heterogeneous velocity field to net lateral dispersion first exceeds the contribution from turbulent diffusion around this $d/\langle s_n \rangle_A$ ($= 1.6$).

The present model for turbulent diffusion suggests that its contribution increases rapidly with $d/\langle s_n \rangle_A$ until $d/\langle s_n \rangle_A = 0.56$ and then decays as $d/\langle s_n \rangle_A$ increases further. With the best-fit scaling constants determined above, the predicted contribution from turbulence constitutes less than 1% of the predicted net $K_{yy}/(U_p d)$ for $d/\langle s_n \rangle_A > 3.3$, and the theory suggests that dispersion arises predominantly from the spatial heterogeneity in the velocity field due to the solid obstructions. Note that $P_{s_{nc}<5d} = 1$ at $d/\langle s_n \rangle_A > 3.3$, and the ϕ dependence predicted by Eq. (3.24) is captured entirely by Koch and Brady (1986)'s Stokes flow solution [Eq. (3.20)]. The good agreement despite the high Re_d suggests that, at large ϕ, the time-averaged velocity field may not be strongly altered by turbulence, whose length scale is constrained by the cylinder separation. This further suggests that $K_{yy}/(U_p d)$ may not change significantly from Stokes flow to high Re_d at high $d/\langle s_n \rangle_A$. Additional measurements are necessary to verify our assumption of Re_d independence. The same data can be used to examine whether the choice of $\epsilon = d$ in the random walk model [Eq. (3.19)] is appropriate at lower Re_d. As a first step towards understanding lateral dispersion prior to the onset of full turbulence, additional LIF experiments were conducted at Re_d below those considered in the present chapter, i.e., at $Re_{\langle s_n \rangle_A} < 74$, at $\phi = 0.20$ and 0.35. These measurements are presented in Ch. 4.

Finally, let us evaluate the assumption $r^*/d = 2$ that we imposed to determine the scaling constants γ_1 and γ_2 in Eq. (3.24). If r^* is treated as a third fitting parameter, least-squares fitting Eq. (3.24) to the experimental data at $\phi > 0$ yields $r^*/d = 1.6$ ($\gamma_1 = 3.8$ and $\gamma_2 = 0.32$), which agrees with $r^*/d = 2$ to within 20%, suggesting that $l_e = l_t$ is a reasonable approximation.

ϕ	$d/\langle s_n \rangle_A$	$K_{yy}/(U_p d)$	n	U_p [cm s^{-1}][a]	Re_d[a]	$Re_{\langle s_n \rangle_A}$[a]	x/d
0.010	0.28	0.21 $\pm$0.02	51	$1.4 - 3.1$	$83 - 190$	$290 - 660$	$55 - 168$
0.031	0.58	0.24 $\pm$0.01	56	$1.0 - 2.7$	$67 - 180$	$120 - 310$	$7 - 174$
0.060	0.93	0.20 $\pm$0.01	44	$1.5 - 2.6$	$97 - 170$	$100 - 180$	$23 - 124$
0.091	1.3	0.18 $\pm$0.01	61	$3.2 - 6.6$	$230 - 480$	$180 - 370$	$22 - 134$
0.15	2.0	0.17 $\pm$0.01	35	$3.1 - 5.8$	$190 - 370$	$94 - 180$	$43 - 223$
0.20	2.7	0.13 $\pm$0.01	48	$3.8 - 6.5$	$210 - 340$	$78 - 130$	$80 - 225$
0.27	4.0	0.17 $\pm$0.02	36	$4.5 - 7.0$	$300 - 480$	$74 - 120$	$27 - 152$
0.35	5.9	0.24 $\pm$0.02	16	$4.6 - 5.6$	$320 - 390$	$53 - 66$	$36 - 145$

Table 3.3: Summary of $K_{yy}/(U_p d)$ data. n is the number of cases for which $Re_{\langle s_n \rangle_A} > 74$ ($\phi = 0.010 - 0.27$) and $Re_{\langle s_n \rangle_A} > 53$ ($\phi = 0.35$).

[a]Values at the solute source.

3.5 Conclusions

Laboratory measurements of turbulence and lateral dispersion in random arrays of cylinders of diameter $d = 0.64$ cm at high Re_d, at which the lateral variance of the time-averaged concentration distribution is independent of Re_d, were presented for $\phi = 0.010 - 0.35$. In sparse arrays, the characteristic size of the largest turbulent eddies is $l_t = d$. However, when the mean nearest-neighbor cylinder spacing, $\langle s_n \rangle_A$, is smaller than d, the turbulence length scale becomes constrained by the pore size (figure 3-9). Thus, even though mean turbulence intensity increases monotonically with ϕ (figure 3-11), its contribution to solute dispersion declines in this regime. Our experiments verified that mean turbulence intensity can be predicted in terms of the cylinder density, l_t/d, and C_D^{form} only. Further, since C_D^{form} in a random cylinder array is a function only of ϕ for a constant d (Ch. 2), mean turbulence intensity in a random cylinder array can be described as a function of ϕ and d only.

The normalized coefficient for net asymptotic lateral dispersion $K_{yy}/(U_p d)$ increases, decreases, and then increases again as ϕ increases. The observed $K_{yy}/(U_p d)$ is described accurately by a linear superposition of models describing the contributions of turbulence and the spatially-heterogeneous velocity field. Comparable agreement is achieved by describing the contribution from the latter by a one-dimensional random walk model with a step size that is comparable to the cylinder diameter, as proposed by Nepf (1999), and by a modification of Koch and Brady (1986)'s Stokes flow solution. The good agreement with the experiment supports the two main assumptions of our turbulent diffusion model. First, only turbulent eddies with characteristic mixing length $l_e \geq d$ contribute significantly to net lateral dispersion. Second, neighboring cylinder centers must be farther than $r^* = 2d$ from each other for the pore space between them to contain such eddies. The fractional volume of the array that comprises pores larger than this critical length scale decreases with increasing $d/\langle s_n \rangle_A$. Consequently, although $\langle \sqrt{k_t}/U_p \rangle$ increases monotonically with $d/\langle s_n \rangle_A$, the contribution of turbulent diffusion to net lateral dispersion decreases for $d/\langle s_n \rangle_A > 0.56$, correctly capturing the observed decrease in net lateral dispersion at intermediate densities.

The conceptual framework presented here is not specific to arrays of circular cylinders. Specifically, the results suggest that the integral length scale l_t and mean turbulence intensity can be determined simply from the distribution and geometry of the elements. In addition, the three $d/\langle s_n \rangle_A$ regimes identified for $K_{yy}/(U_p d)$ are expected to apply to solute transport in random arrays in general. Furthermore, observations of transverse dispersion in ceramic foam agree with Koch and Brady (1985)'s theory for packed bed of spheres in Stokes flow [e.g., Pereira et al., 2005, figure 3(d)]. This agreement suggests that, at least in isotropic media of $\phi = O(0.13)$, transverse dispersion is not sensitive to the exact geometry of the individual obstacles (Hackert et al., 1996). Similarly, Eqs. (3.23) and (3.24), with the scaling constants determined in this work, may accurately describe transport in plant canopies of slightly different stem morphology. Finally, the good agreement between the data and the model for the contribution from the spatially-heterogeneous velocity field based on Koch and Brady (1986)'s analytical solution at $\phi \geq 0.20$ suggests that lateral dispersion predictions based on Stokes flow analysis may be applicable at higher Reynolds numbers at sufficiently high ϕ once asymptotic (long-time/long-distance) dispersion is achieved. Indeed, Hackert et al. (1996) and Pereira et al. (2005)'s transverse dispersion measurements, which also agree with a Stokes flow solution (discussed above), were collected at pore Reynolds numbers of $10 - 300$, where inertia is clearly non-negligible.

Chapter 4

Lateral dispersion at transitional Reynolds number: dense arrays[a]

Abstract

Lateral dispersion of passive solute was examined in unsteady laminar flows and in turbulent flows prior to the onset of fully turbulent conditions through a two-dimensional array of randomly distributed circular cylinders of uniform diameter d. These flows, and the corresponding Reynolds numbers, are referred to as transitional flows and transitional Re_d in this thesis. The present chapter focuses on dense arrays, for which the theory developed in Ch. 3 implies that the asymptotic (long-time/long-distance) dispersion coefficient, when normalized by the mean interstitial fluid velocity, $\langle \overline{u} \rangle$, and d, will only exhibit a weak dependence on Re_d. However, the advective distance required to reach asymptotic dispersion is expected to be controlled by pore-scale mixing, which is strongly Re_d-dependent prior to the onset of full turbulence. Laser-induced fluorescence was used to measure the time-averaged lateral concentration profiles of solute released continuously from a point source in arrays of solid volume fraction $\phi = 0.20$ and 0.35 at $Re_d = 48$ to 120. Results are compared with previous measurements at higher Re_d. Lateral dispersion reaches the same rate as asymptotic dispersion in fully turbulent flow at $x \approx 154d$ at $(\phi, Re_d) = (0.20, 110 - 120)$ and at $x \approx 87d$ at $(\phi, Re_d) = (0.35, 300 - 390)$. In contrast, dispersion does not reach the fully turbulent flow limit at $Re_d < 100$ within the range of x considered. Also, concentration profiles deviate further from a Gaussian distribution at $\phi = 0.35$ than at 0.20 for similar Re_d and $x\phi/d$. From these observations, it can be inferred that the pre-asymptotic regime extends farther downstream, in terms of the number of

[a]This chapter was submitted to *Physics of Fluids* as Tanino and Nepf, 2008a, with minor differences. This material is based on work supported by the National Science Foundation grant EAR−0309188. Any opinions, conclusions, or recommendations expressed in this material are those of the authors and do not necessarily reflect the views of the National Science Foundation.

cylinders spanned, at lower Re_d and at larger ϕ.

4.1 Introduction

Lateral dispersion at sufficiently high Re_d exhibited two properties over the range of x considered in Ch. 3 ($Re_d > 67$ to 320 and $x/d > 7$ to 80, depending on ϕ). First, $\mathrm{d}\left\langle\sigma_y^2\right\rangle/\mathrm{d}x$ remained constant in x, consistent with a spatially homogeneous $K_{yy}/(\langle\overline{u}\rangle d)$. Second, $\mathrm{d}\left\langle\sigma_y^2\right\rangle/\mathrm{d}x$ was independent of Re_d. As a result, the corresponding $K_{yy}/(\langle\overline{u}\rangle d)$ was a function only of ϕ (d was kept constant). Further, it was shown that $K_{yy}/(\langle\overline{u}\rangle d)$ in this high-Re_d regime can be described by the linear superposition of a model for turbulent diffusion and existing models for asymptotic (long-distance) dispersion associated with the tortuous flow path that fluid is forced to follow around the cylinders (Ch. 3).

In predicting the contribution from turbulent diffusion, fully turbulent flow, defined here to refer to flow that has achieved the maximum (and therefore Re_d-independent) mean turbulence intensity for that ϕ, was assumed. The model predicts that turbulent diffusion makes a non-negligible (specifically, $\geq 10\%$) contribution to $K_{yy}/(\langle\overline{u}\rangle d)$ at $d/\langle s_n\rangle_A \leq 2.6$ ($\phi \leq 0.19$) in fully turbulent flow [Eq. (3.24), with scaling constants as proposed in § 3.4.3]. Since turbulent diffusion must decrease as Re_d decreases below the fully turbulent regime, the theory implies that $K_{yy}/(\langle\overline{u}\rangle d)$ will also decrease as Re_d decreases in this ϕ range in turbulent flow. However, in unsteady laminar flow, periodic wakes may introduce a different mechanism of dispersion. Unsteady laminar flows at intermediate ϕ were not explicitly considered in this thesis. Nevertheless, selected $\left\langle{\sigma_y}^2\right\rangle$ measurements at Re_d prior to the onset of full turbulence are presented in Appendix H for $\phi = 0.091$ and 0.15.

Conversely, the model predicts that at large ϕ (> 0.19), turbulence does not contribute significantly to asymptotic dispersion and, consequently, that the contribution from the tortuous flow path, i.e., the time-averaged, spatially-heterogeneous velocity field, dominates. In dense arrays, physical reasoning suggests that the time-averaged velocity field, and therefore its contribution to lateral dispersion, are determined pri-

marily by the local cylinder configuration and, therefore, do not depend strongly on Re_d. This conjecture is supported by figure 3-6, which shows that lateral transects of turbulence intensity and $\overline{u}/U_p$ remain approximately constant with Re_d. Therefore, $K_{yy}/(\langle\overline{u}\rangle d)$ at $\phi > 0.19$ is not expected to depend strongly on Re_d either. To our knowledge, the Re_d-dependence of the time-averaged velocity field has not been investigated directly. Nevertheless, the good agreement between experiment and the model in Ch. 3, which assumes a Re_d-independent contribution from the tortuous flow path, supports this conjecture. Indeed, Hill et al. (2001) made the same conjecture for dense arrays of randomly distributed spheres, based on their observation that the spatial variance of the transverse components of velocity normalized by $\langle\overline{u}\rangle^2$ differ by less than 4% between Stokes flow and $Re_d = 113$ in their numerical simulations at $\phi = 0.588$. The same conjecture has also been made for rhombohedrally distributed spheres (Mickley et al., 1965).

In fully turbulent flow, $\mathrm{d}\left\langle\sigma_y^2\right\rangle/\mathrm{d}x$ is expected to be independent of Re_d at all x. This implies that $\left\langle\sigma_y^2\right\rangle(x)$ is also Re_d-independent at all x in this flow regime, given the same initial distribution of the solute $\left[\left\langle\sigma_y^2(x=0)\right\rangle = 0\right]$. Indeed, at $\phi = 0.20$, $\left\langle{\sigma_y}^2\right\rangle$ is independent of Re_d above $Re_d \approx 200$ (figure A-1). However, $\left\langle{\sigma_y}^2\right\rangle$ decreases as Re_d decreases below $Re_d \approx 100$ (figure A-1). If asymptotic $\mathrm{d}\left\langle\sigma_y^2\right\rangle/\mathrm{d}x$ does not depend strongly on Re_d at this ϕ ($= 0.20$), this Re_d dependence of $\left\langle\sigma_y^2\right\rangle$ at $Re_d < 100$ must arise entirely from a Re_d-dependent pre-asymptotic dispersion.

The objective of the present study is to use laboratory observations to evaluate two conjectures for lateral dispersion in dense arrays:

(i) asymptotic $\mathrm{d}\left\langle\sigma_y^2\right\rangle/\mathrm{d}x$ exhibits only a weak dependence on Re_d and

(ii) the advective distance required for the solute to achieve this asymptotic behavior is strongly dependent on Re_d prior to the onset of full turbulence, due to the Re_d dependence of pore-scale mixing.

The latter conjecture is explained in detail in § 4.3. To the authors' knowledge, experimental measurements of lateral dispersion at transitional Re_d within homogeneous random cylinder arrays are not currently available in the literature. Shavit and Bran-

don (2001) report laboratory measurements in a $\phi = 0.035$ array, but illustrations of their array suggest that the cylinder distribution was in fact not random. More recently, Serra et al. (2004) measured the lateral dispersion of solute released at the upstream edge of a random array of $\phi = 0.10$, 0.20, and 0.35 at $Re_d = 11 - 120$. Their estimates of $K_{yy}/(\langle\overline{u}\rangle d)$ are independent of Re_d within experimental uncertainty over $32 < Re_d < 120$, which is consistent with conjecture (i) above. However, the ϕ dependence of their reported values disagrees with that reported in Ch. 3 (figure 3-15). Specifically, $K_{yy}/(\langle\overline{u}\rangle d)$ at $\phi = 0.10$ and at $\phi = 0.20$ were the same within experimental uncertainty, and $K_{yy}/(\langle\overline{u}\rangle d)$ was the smallest at $\phi = 0.35$ in Serra et al. (2004)'s experiments. This disagreement may be due to their flow not being fully developed at the solute source or measurements being collected at very short distances ($x/d = 8-26$). Although Serra et al. (2004) report that their estimates of K_{yy} did not vary with x within this range, comparison with experiments reported in the present chapter suggests that they were sampling in the pre-asymptotic regime (§ 4.3.3).

In this study, a set of LIF experiments were performed in arrays of $\phi = 0.20$ and 0.35 at selected Re_d in the range $Re_d = 48$ to 120, which extends from steady laminar to turbulent conditions. These experiments were not reported in Ch. 3. Visualizations of pore-scale mixing are presented, and the observed Re_d dependence is discussed qualitatively (§ 4.3.1). Time-averaged concentration profiles are discussed in § 4.3.2 and § 4.3.3, in terms of their deviation from a Gaussian distribution, their variance, and the evolution of these two parameters with x. The growth rate of the variance is also compared with the corresponding $K_{yy}/(\langle\overline{u}\rangle d)$ in fully turbulent flow presented in Ch. 3, and pre-asymptotic and asymptotic regimes are identified.

4.2 Experimental procedure

LIF was used to measure the lateral concentration distribution at (x, Re_d) selected systematically between $Re_d = 48$ to 120 and $x = 38$ to 234 cm ($x = 0$ is the solute source). The range of experimental conditions examined are summarized in Table 4.1. The flume setup and procedure used in the laboratory experiments reported in this

chapter were essentially the same as those described in § 3.3 and § 3.3.2, respectively. Two changes in the setup are noted. First, a different argon ion laser, Coherent INNOVA^R 70C ion laser, was used for some of the experiments, as the laser used in Ch. 3 was replaced during the course of the experiments reported in this chapter. Second, different $\phi = 0.20$ arrays were created by selecting different combinations of the 20% and 35% hole fraction sheets. In doing so, more array realizations could be included in the ensemble average. The duration of the experiments in $\phi = 0.20$ ranged from 46 to 213 s (4.5 to 18.9 frames per second). In $\phi = 0.35$, images were collected over 94 s (10.1 to 10.7 frames per second) in all but six runs; the duration of the other six runs ranged from 80 to 112 s (9.0 to 12.5 frames per second). The high frame rate at $\phi = 0.20$ arose because one of the two computers used was able to record images at a faster frame rate.

In this chapter, two quantitative parameters were considered in describing the time-averaged intensity profile, $\overline{I(y,t)}$. First, its variance was calculated as

$$\sigma_y{}^2(x) = \frac{m_2(x)}{m_0(x)} - \left[\frac{m_1(x)}{m_0(x)}\right]^2, \tag{4.1}$$

where $m_j(x)$ is the j^{th} moment,

$$m_j(x) = \int_{\kappa_2}^{\kappa_1} y^j \overline{I(y,t)}\ \mathrm{d}y. \tag{4.2}$$

$y = 0$ is defined at the lateral position of the solute source. The zeroth, first, and second moments and the corresponding σ_y^2 were calculated by setting the limits of integration in Eq. (4.2), $\kappa_{1,2}$, at the two edges of the images. Next, $\kappa_{1,2}$ were redefined as $\kappa_{1,2} = (m_1/m_0) \pm 4\sigma_y$ and the calculation was repeated. Second, the deviation of $\overline{I(y,t)}$ from a Gaussian distribution was parameterized by

$$C_{ms} = \frac{1}{\kappa_1 - \kappa_2} \int_{\kappa_2}^{\kappa_1} \frac{\left\{\overline{I(y,t)}/m_0 - I_G(y)\right\}^2}{I_G(y)}\ \mathrm{d}y, \tag{4.3}$$

where $\kappa_{1,2} = (m_1/m_0) \pm 3\sigma_y$ and $I_G(y)$ is a Gaussian distribution with unit total mass

ϕ	$d/\langle s_n \rangle_A$	x_c/d (fully turbulent)	Re_d	$Re_{\langle s_n \rangle_A}$	$\langle \overline{u} \rangle$ [cm s^{-1}]	$\left\langle \overline{H} \right\rangle$ [cm]	n
0.20	2.70	$O(5.9)$	58 - 61	21 - 22	0.82 - 1.4	12.7 - 16.8	57
			84 - 89	31 - 33	1.3 - 2.0	13.5 - 16.9	62
			110-120	40 - 43	1.6 - 2.5	12.8 - 16.5	39
			310-340	110-130	5.0 - 6.5	11.8 - 15.1	23[a]
0.35	5.95	$O(11)$	48 - 51	8.1-8.6	0.93 - 1.1	12.8 - 14.8	22
			77 - 82	13-14	1.4 - 1.8	13.5 - 15.0	30
			97 -100	16-17	1.4 - 2.2	13.5 - 15.3	31
			300-390	51-66	4.5 - 5.6	13.3 - 20.3	17[a]

Table 4.1: Relevant parameters for experiments considered in this chapter. $d/\langle s_n \rangle_A$ is predicted by Eq. (D.18). x_c/d is predicted by Eq. (4.5), with $\left\langle \sqrt{k_t}/\langle \overline{u} \rangle \right\rangle$ as predicted for fully turbulent flow by Eq. (3.33) and l_t/d as predicted by Eq. (4.6). $\langle \overline{u} \rangle$ was approximated by its cross-sectional average. n is the total number of LIF experiments at all x for $(\phi, Re_d) = (0.35, 300 - 390)$ and only at x for which ensemble-averaged values are derived for all other (ϕ, Re_d). Values for Re_d, $Re_{\langle s_n \rangle_A}$, $\langle \overline{u} \rangle$, and $\left\langle \overline{H} \right\rangle$ represent the range across these replicate runs at the solute source.

[a]These experiments were reported in Ch. 3.

and with the same center of mass (m_1/m_0) and σ_y^2 as $\overline{I(y,t)}$. Note that the integral in Eq. (4.3) is the chi-square statistic.

4.3 Experimental results

Recall from § 3.2.1 that, by analogy with turbulent diffusion, dispersion in a homogeneous array is expected to become Fickian once the plume becomes well-mixed at, and significantly larger than, the spatial scales of all contributing mechanisms (Corrsin, 1974; Koch and Brady, 1985; White and Nepf, 2003). In steady laminar flows and turbulent flows through dense arrays, the mechanisms that contribute to (macroscopic) lateral dispersion are molecular diffusion, turbulent diffusion, and dispersion associated with the tortuous flow path. Turbulent eddies are constrained by the local cylinder spacing, and thus the largest eddies scale with $\langle s_n \rangle_A$ in dense arrays (Ch. 3). Dispersion associated with the tortuous flow path can be modeled as a series of independent, discrete lateral deflections that fluid particles undergo as they flow around cylinders; each deflection is expected to scale with d (Nepf, 1999; Masuoka and Takatsu, 1996). Accordingly, asymptotic dispersion is expected once $\left\langle \sigma_y^2 \right\rangle \gg d^2, \langle s_n \rangle_A{}^2$.

The initial (small x) growth of the ensemble-averaged variance of the plumes may be approximated by $\left\langle \sigma_y^2 \right\rangle = 2D_{\text{pore}}t = 2D_{\text{pore}}x/\langle \overline{u} \rangle$, where the diffusion coefficient D_{pore} characterizes pore-scale mixing. Then, the mean streamwise distance that the solute is advected before achieving asymptotic behavior, x_c, is expected to scale as

$$\frac{x_c}{d} \sim \left(\frac{\max\{d, \langle s_n \rangle_A\}}{d} \right)^2 \frac{\langle \overline{u} \rangle d}{D_{\text{pore}}}. \tag{4.4}$$

In steady laminar flow, D_{pore} is the molecular diffusion coefficient D_m, and x_c/d is linearly proportional to the Peclet number $Pe \equiv \langle \overline{u} \rangle d/D_m$. This Pe dependence has been observed in simulations of different types of steady laminar obstructed flows, e.g., in packed beds of spheres (Stapf et al., 1998; Maier et al., 2000), in periodic cylinder arrays (Acharya et al., 2007), and in a lattice network (Bijeljic and Blunt,

2007). In contrast, in turbulent flow, turbulent mixing is the dominant mechanism for pore-scale mixing. Then, $D_{\text{pore}} \sim \langle\sqrt{k_t}\rangle l_t$. Recall that $d > \langle s_n\rangle_A$ in the arrays considered in the present chapter (Table 4.1). Under these conditions, Eq. (4.4) yields

$$\frac{x_c}{d} \sim \left(\left\langle \frac{\sqrt{k_t}}{\langle\overline{u}\rangle} \right\rangle \frac{l_t}{d}\right)^{-1}. \tag{4.5}$$

It was shown in Ch. 3 that the integral length scale of turbulence is accurately described by $l_t/d = \min\{1, \langle s_n\rangle_A/d\}$ in fully turbulent flow. Then, in the arrays considered in this chapter,

$$\frac{l_t}{d} = \frac{\langle s_n\rangle_A}{d}, \tag{4.6}$$

which decreases monotonically as ϕ increases. Further, Eq. (4.6) is expected to be valid in transitional turbulent flow as well, because the size of the largest turbulent eddies is still constrained by the cylinder spacing, which is independent of Re_d. In contrast, mean turbulence intensity, $\left\langle\sqrt{k_t}/\langle\overline{u}\rangle\right\rangle$, is expected to depend strongly on Re_d. In fully turbulent flow, $\left\langle\sqrt{k_t}/\langle\overline{u}\rangle\right\rangle$ can be described by Eq. (3.33); at smaller Re_d, values for $\left\langle\sqrt{k_t}/\langle\overline{u}\rangle\right\rangle$ are not available, to our knowledge. Nevertheless, $\left\langle\sqrt{k_t}/\langle\overline{u}\rangle\right\rangle$ is expected to increase gradually and monotonically with Re_d between laminar and fully turbulent conditions. While we are not aware of any experimental verification of this expected Re_d dependence in random arrays of cylinders or spheres, it has been observed in ceramic foams (Hall and Hiatt, 1996) and in numerical simulations of a periodic staggered cylinder array (Hill and Koch, 2002, $\phi = 0.19$). With this assumption, Eq. (4.5) implies that, in transitional turbulent flow, x_c decreases as Re_d increases until the flow becomes fully turbulent. The appropriate definition for D_{pore} and the mechanism that replaces turbulent diffusion in unsteady laminar flow are not obvious. Nevertheless, x_c is expected to be continuous over all Re_d, which requires that x_c decrease as the flow transitions from the steady laminar flow regime to the turbulent flow regime.

In summary, dispersion in dense arrays ($\phi > 0.19$) are expected to exhibit three properties. First, dispersion at large x is expected to be Fickian, i.e., $\mathrm{d}\langle\sigma_y^2\rangle/\mathrm{d}x \neq f(x)$, at all Re_d. Second, $\mathrm{d}\langle\sigma_y^2\rangle/\mathrm{d}x$ in this asymptotic limit is expected to be approximately

the same for all Re_d (§ 4.1). Third, the distance required to reach this limit, x_c, is expected to decrease as Re_d increases beyond steady laminar flow, until fully turbulent flow is achieved [Eq. (4.5)]. The simplest dependence of $\langle\sigma_y^2(x)\rangle$ on x and Re_d that would satisfy these assumptions is depicted in figure 4-1 for a given ϕ. Note that this schematic further assumes that $\mathrm{d}\langle\sigma_y^2\rangle/\mathrm{d}x$ at a given Re_d increases monotonically as it approaches its asymptotic (large x) limit. With this pre-asymptotic behavior, $\langle\sigma_y^2(x)\rangle$ at a given x necessarily increases with Re_d until fully turbulent flow is reached for all x (cf. red line in figure 4-1), consistent with observation (Appendix A). It should be noted that in flows in which the lateral velocity autocorrelation function takes on negative values, $\mathrm{d}\langle\sigma_y^2\rangle/\mathrm{d}x$ will decrease with increasing x at some $x < x_c$ prior to achieving its asymptotic limit, as highlighted in the classic paper by Taylor (1922). A transient decrease in the (pre-asymptotic) transverse dispersion coefficient has been observed in numerical simulations of randomly packed bed of spheres (Maier et al., 2000) and lattice networks (Bijeljic and Blunt, 2007); Maier et al. (2000) demonstrate that the decrease coincides with a negative autocorrelation function in their simulations.

4.3.1 Pore-scale mixing and the approach to asymptotic dispersion

Pore-scale mixing was visualized using fluorescein for both solid volume fractions ($\phi = 0.20$ and 0.35) in steady laminar flow and in unsteady flow (figure 4-2). Beginning at the lowest Re_d, tracer streaklines remained stationary in time, indicating steady flow, everywhere in figure 4-2(a) and (e) except in the region immediately downstream of the cylinder marked with an oval in figure 4-2(a). Vortices shed from the marked cylinder, indicating that flow was unsteady in that region. This simultaneous occurrence of both steady and unsteady flow at $(\phi, Re_d) = (0.20, 61)$ is attributed to the random distribution of the cylinders and the resulting spatial variations in the local velocity field.

In the absence of turbulence, the tracer is mixed with ambient fluid only through

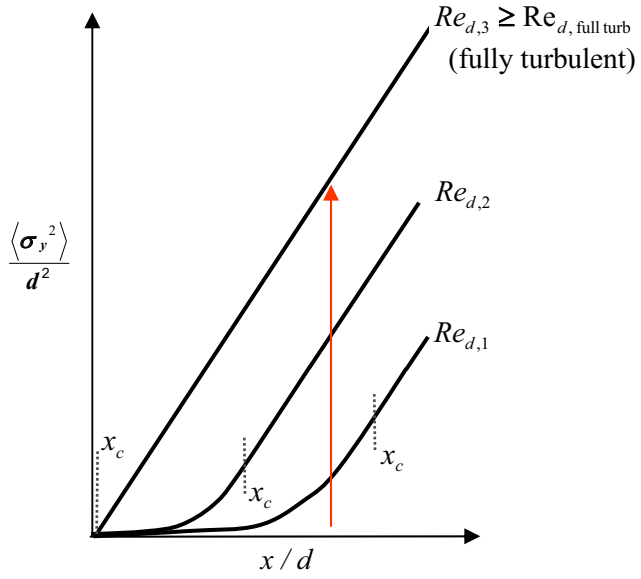

Figure 4-1: Anticipated evolution of the variance of the lateral concentration profile with distance, and its dependence on Re_d in unsteady laminar and turbulent flows in dense arrays. The distance required to reach the asymptotic limit at a given Re_d, x_c (dotted), is described by Eq. (4.4). $Re_{d,1} < Re_{d,2} < Re_{d,\text{full turb}} \leq Re_{d,3}$, where $Re_{d,\text{full turb}}(\phi)$ denotes the Re_d at which flow becomes fully turbulent. Not to scale.

molecular diffusion, which is a very slow process: $D_m \approx 3 \times 10^{-6}$ cm^2 s^{-1} for rhodamine WT (estimated from Schwarzenbach et al., 2003, figure 18.10) and $D_m \approx (3-5) \times 10^{-6}$ cm^2 s^{-1} for fluorescein (Rani et al., 2005; Hodges and La Mer, 1948; Petrasek and Schwille, 2008). In the time taken for the tracer to advect to the right edge of the photo in figure 4-2(a) ($x \approx 22d$) and figure 4-2(e) ($x \approx 15d$), molecular diffusion can only have mixed the tracer over $O(0.01d)$. Accordingly, thin, distinct filaments are observed in the photos. In contrast, at $Re_d > 120$ in the $\phi = 0.20$ array and at $Re_d = 180$ in the $\phi = 0.35$ array, the interface between the tracer and the ambient fluid was blurred, and the tracer was well-mixed at the pore scale and distributed over distances larger than d and $\langle s_n \rangle_A$ by the time it reached the right edge of the respective photos [figure 4-2(c), (d), (h)]. The rapid pore-scale mixing and the absence of any apparent periodicity in the tracer distribution are indicative of turbulent flow, in which small-scale turbulence provides an additional, much faster mechanism for mixing within the pores. Recall that the tracer plume must be well-mixed and much wider than d and $\langle s_n \rangle_A$ for its dispersion to be asymptotic. Based

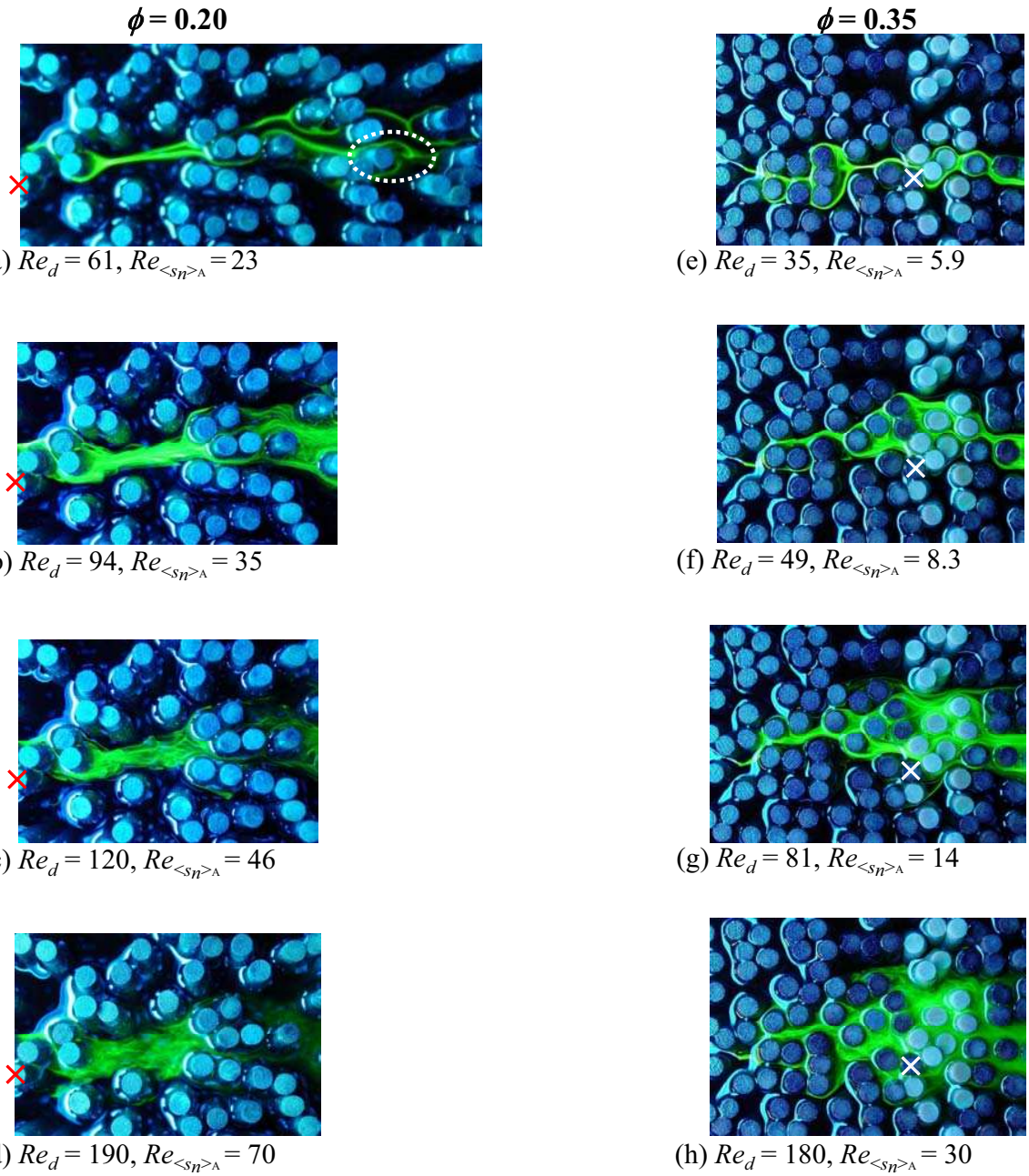

Figure 4-2: Flow visualization by illuminating fluorescein with blue lighting (Current Inc.) in a $\phi = 0.20$ array at Re_d = (a) 61, (b) 94, (c) 120, and (d) 190 and in a $\phi = 0.35$ array at Re_d = (e) 35, (f) 49, (g) 81, and (h) 180. These values correspond to $Re_{\langle s_n \rangle_A}$ = (a) 23, (b) 35, (c) 46, (d) 70, (e) 5.9, (f) 8.3, (g) 14, and (h) 30. Mean flow was from left to right. The fluorescein injection position was fixed over (a) - (d) and over (e) - (h). In (a) - (d), fluorescein was injected along the upstream edge of the cylinder marked with a ×; in (e) - (h), the source is visible in the photo. In (e) - (h), the distance between the source and the cylinder marked with a white × is 6.0 cm. Vortex shedding can be observed downstream of one of the cylinders in (a) (dotted oval).

on the above observations, we expect that beyond the steady laminar flow regime, the streamwise distance necessary for dispersion to become asymptotic, x_c, is smaller at higher Re_d.

Although the transition from steady to fully turbulent flow, and its dependence on ϕ, have not been systematically investigated in obstructed flows, existing observations suggest that they are complex. For example, compared to flow past an isolated cylinder, flow regime transitions appear to occur at a lower Re_d in sparse arrays and at a higher Re_d in dense arrays. Specifically, flow in the $\phi = 0.20$ array became unsteady at a *higher* Re_d (> 60) than the near wake of an isolated cylinder [figure 4-2(a)]. This apparent delay in the onset of unsteadiness in dense arrays is reminiscent of the delay in the onset of vortex shedding in uniform shear flow past an isolated cylinder reported by Kiya et al. (1980). In contrast, in a $\phi = 0.010$ array, a laminar vortex street was observed, and flow became turbulent, at a *lower* Re_d than in an isolated cylinder wake (figure 3-4). Further, it is unclear whether periodic vortex shedding would even occur from all cylinders at large ϕ, given the random distribution of cylinders and their proximity to each other. Indeed, the absence of vortex shedding has been reported previously in packed beds of spheres (Mickley et al., 1965, $\phi = 0.74$).

Given the random distribution of the cylinders, detailed velocity measurements are necessary to describe how flow and turbulence properties vary with ϕ and Re_d and to determine if certain regimes, such as the unsteady laminar flow regime, are suppressed above a certain ϕ. It would be interesting to determine if the Reynolds number can be redefined using a different length scale such that the onset of unsteadiness, turbulence, and full turbulence occur at the same values at all ϕ. Although a likely candidate, the Reynolds number based on the mean distance between nearest cylinders, $Re_{\langle s_n \rangle_A}$, does not appear to capture the exact ϕ dependence of these flow regime transitions. For example, tracer remains in distinct filaments at $x/d \approx 15$ at $Re_{\langle s_n \rangle_A} = 23$ in the $\phi = 0.20$ array, but not above $Re_{\langle s_n \rangle_A} \geq 8.3$ in the $\phi = 0.35$ array (figure 4-2).

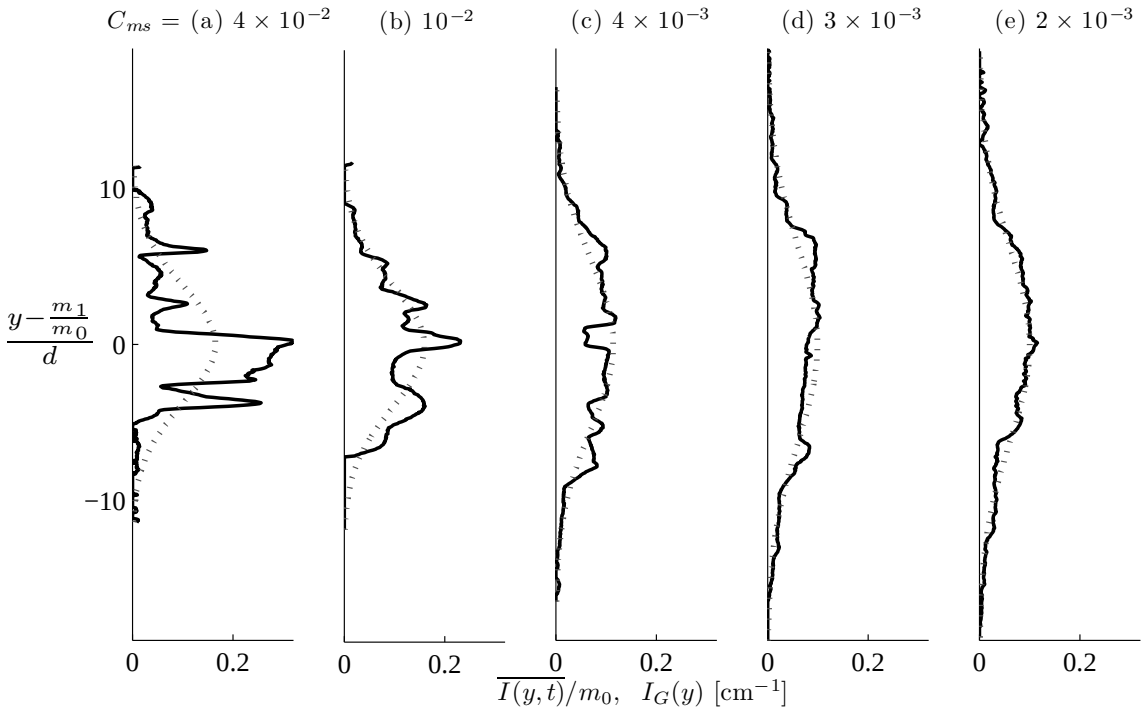

Figure 4-3: $\overline{I(y,t)}/m_0$ [cm^{-1}] (solid) and the corresponding $I_G(y)$ [dotted; see Eq. (4.3)] for selected runs at $(\phi, Re_d) = (0.35, 97-100)$. $x\phi/d$ increases from left to right: (a) 21, (b) 42, (c) 58, (d) 87, and (e) 100. C_{ms} values are also in [cm^{-1}]. The growth of σ_y^2 with x can be discerned from the width of the profiles, which are truncated at $y = m_1/m_0 \pm 3\sigma_y$.

4.3.2 Deviation of the time-averaged concentration profile from a Gaussian distribution

Fickian dispersion of solute released from a point source results in a Gaussian concentration distribution. Therefore, the deviation of the time-averaged concentration profile, $\overline{I(y,t)}$, from a Gaussian distribution is a convenient measure of the proximity to Fickian behavior. For reference, selected $\overline{I(y,t)}$ are presented in figure 4-3. Note that the ensemble average of $\overline{I(y,t)}/m_0$, where $(x,y) = (0,0)$ is defined at the solute source, is equivalent to the probability density function of the solute particle displacement. The time-averaged profiles gradually approach a Gaussian distribution as x increases, and this trend is reflected in the corresponding decrease in the mean normalized squared deviation, C_{ms} [Eq. (4.3)].

The ensemble-averaged C_{ms} are presented in figure 4-4 as a function of $x\phi/d$, which

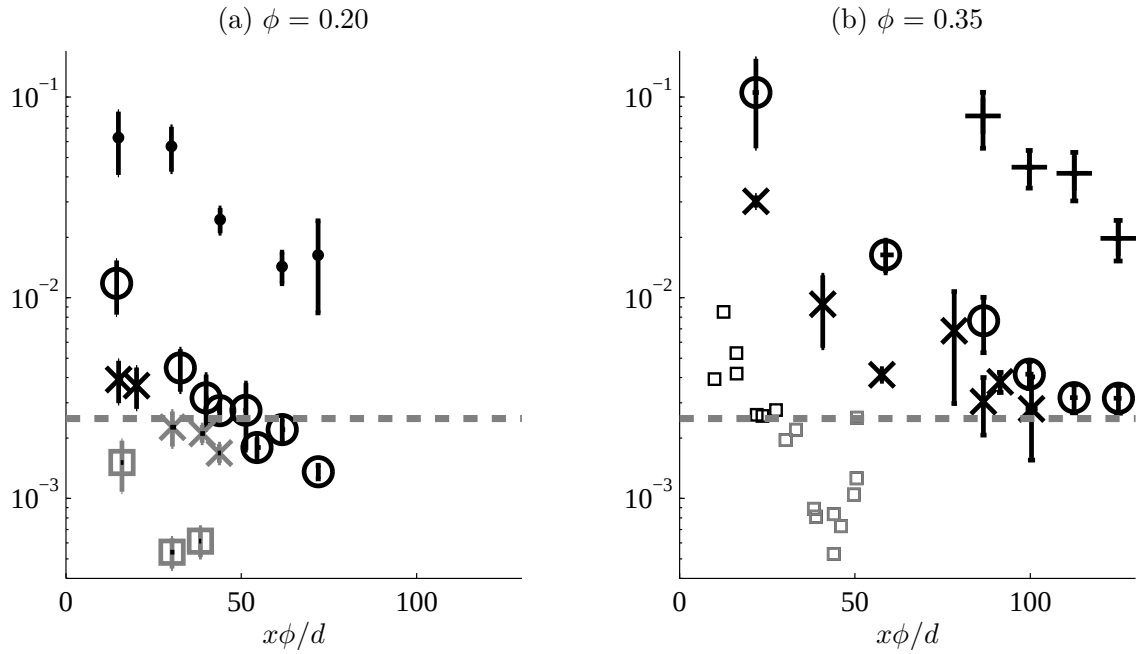

Figure 4-4: Ensemble average of C_{ms} [cm^{-1}] as defined by Eq. (4.3) for (a) $\phi = 0.20$ at $Re_d = 58 - 61$ ($\cdot$), $84 - 89$ ($\circ$), $110 - 120$ ($\times$), and $310 - 340$ (square; Ch. 3) and (b) $\phi = 0.35$ at $Re_d = 48 - 51$ ($+$), $77 - 82$ ($\circ$), and $97 - 100$ ($\times$). Each data point for these (ϕ, Re_d) represents an average of four or more runs: horizontal bars indicate the range in x and vertical bars indicate the standard error of the mean. (b) also includes individual C_{ms} at $(\phi, Re_d) = (0.35, 300 - 390)$ (square; Ch. 3). Note that ensemble averages cannot be computed for this (ϕ, Re_d) because replicate measurements were not collected. Data points in grey correspond to (ϕ, Re_d, x) at which dispersion was observed to have occurred at the same rate as asymptotic dispersion in fully turbulent flow (figures 4-5 and 4-6). $\langle C_{ms} \rangle = 2.5 \times 10^{-3}$ cm^{-1} (dashed) is the proposed empirical boundary between the pre-asymptotic and asymptotic dispersion regimes.

is the expected number of cylinders in a $d \times x$ area (multiplied by $\pi/4$). Two salient trends can be identified at each ϕ. First, at each Re_d, $\langle C_{ms} \rangle$ decreases as x increases. This trend is attributed to the plume having had more time to mix over the pore scale at larger x. Second, for all x considered, $\langle C_{ms} \rangle$ decreases as Re_d increases. This is attributed to the enhancement of pore-scale mixing that results from the increase in turbulence intensity with increasing Re_d. Note that the large reduction in $\langle C_{ms} \rangle$ between $Re_d = 58 - 61$ and $84 - 89$ at $\phi = 0.20$ coincides with the transition from steady to unsteady flow captured in figure 4-2(a, b). A similar reduction occurred at $\phi = 0.35$ between $Re_d = 48 - 51$ and $77 - 82$. Note that the ranges in Re_d reflect unintended, small variations across replicate runs, not measurement uncertainty (Table 4.1).

At similar $x\phi/d$ and Re_d, $\langle C_{ms} \rangle$ was consistently larger at $\phi = 0.35$ than at $\phi = 0.20$ (figure 4-4). This implies that at larger ϕ, a longer advective distance in terms of the number of cylinders per d-width is required for dispersion to become Fickian for the same Re_d. This ϕ dependence is expected in fully turbulent flow, for which Eq. (4.5) predicts $x_c\phi/d \sim 4$ for $\phi = 0.35$ and ~ 1 for $\phi = 0.20$ (Table 4.1). Unfortunately, the ϕ dependence of $x_c\phi/d$ at transitional Re_d cannot be predicted from Eq. (4.5) because measurements of $\left\langle \sqrt{k_t}/\langle \overline{u} \rangle \right\rangle$ are not available. However, flow became fully turbulent at smaller $\langle \overline{u} \rangle/\nu$ in ceramic foams with larger pore diameters in Hall and Hiatt (1996)'s experiments. Recall that $d = 0.64$ cm in all of our experiments, and runs with the same $\langle \overline{u} \rangle/\nu$ have the same Re_d. Therefore, the analogous trend would be for flow to become fully turbulent at smaller Re_d at smaller ϕ (larger $\langle s_n \rangle_A$). This trend would yield a smaller x_c/d at smaller ϕ at Re_d close to the onset of full turbulence, consistent with the observed behavior of $\langle C_{ms} \rangle$. Such a trend would also be consistent with the delayed onset of vortex shedding from a cylinder in the presence of shear (Kiya et al., 1980), since shear is presumably larger at smaller $\langle s_n \rangle_A$ (higher ϕ) for a given $\langle \overline{u} \rangle$. To the authors' knowledge, the ϕ dependence of dispersion or turbulence at transitional Re_d has not been explored for other types of homogeneously obstructed flows, presumably because ϕ cannot be altered significantly or easily in other types of real porous media.

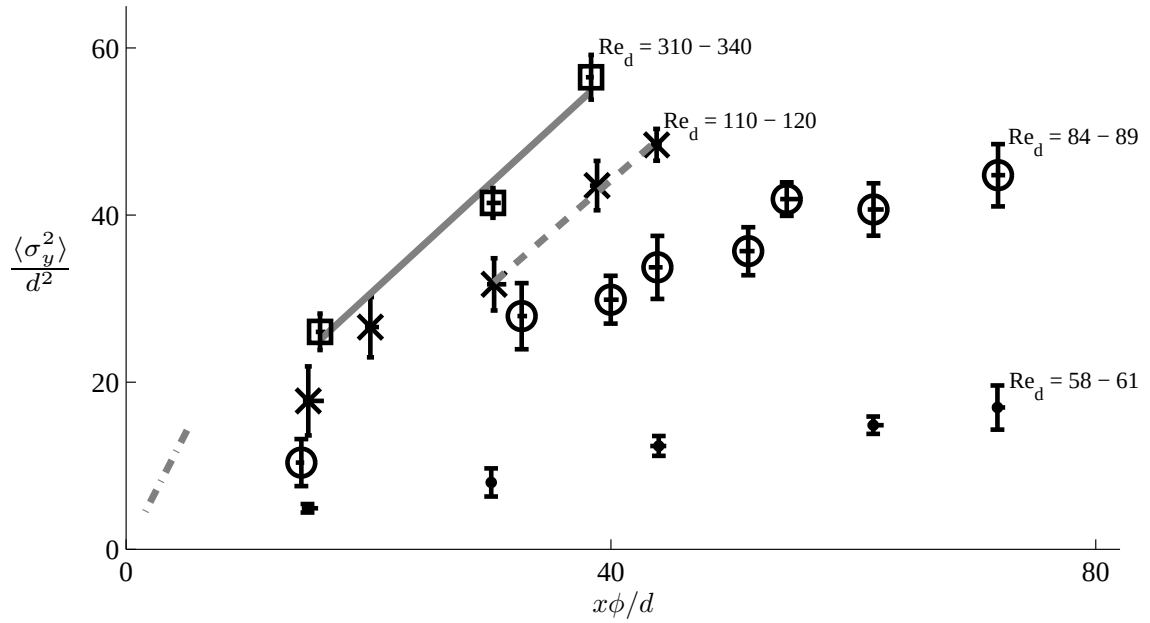

Figure 4-5: Evolution of the ensemble-averaged variance with normalized distance at $\phi = 0.20$. Markers same as figure 4-4(a). Solid line is the least-squares fit to $\left\langle \sigma_y^2 \right\rangle (x)$ at $Re_d = 310-340$: $\mathrm{d}\langle\sigma_y^2\rangle/\mathrm{d}x = 0.17 \pm 0.03$ cm ($R^2 = 0.98, n = 3$). Dashed line is the least-squares fit to $\left\langle \sigma_y^2 \right\rangle (x)$ at $Re_d = 110-120$, $x\phi/d > 30$: $d\langle\sigma_y^2\rangle/dx = 0.16 \pm 0.01$ cm ($R^2 = 0.99, n = 3$). Also included is $\left\langle \sigma_y^2 \right\rangle / x = 0.56$ cm (dashed-dotted), as measured by Serra et al. (2004) at $37 < Re_d \leq 110$.

4.3.3 Variance of the time-averaged concentration profile

The ensemble-averaged variance of the time-averaged lateral concentration profiles $\left(\langle\sigma_y^2\rangle\right)$ are presented in figures 4-5 and 4-6 for $\phi = 0.20$ and 0.35, respectively. A subset of measurements at high Re_d that were reported in Ch. 3 are also included (square). As discussed in § 4.1, $\langle\sigma_y^2\rangle$ at a given x becomes Re_d-independent at $Re_d \approx 200$ in a $\phi = 0.20$ array (Appendix A). The high Re_d ($= 310 - 340$) data for $\phi = 0.20$ were selected from this regime, i.e., both $\langle\sigma_y^2\rangle$ and $\mathrm{d}\langle\sigma_y^2\rangle/\mathrm{d}x$ are independent of Re_d. At $\phi = 0.35$, Re_d-independent $\langle\sigma_y^2\rangle$ could not be confirmed under experimental conditions considered, i.e., at $Re_d < 400$. Therefore, $\sigma_y^2(x)$ at $(\phi, Re_d) = (0.35, 300 - 390)$ is expected to be smaller than in fully turbulent flow for all x (cf. figure 4-1). Unfortunately, the laboratory flume cannot accommodate $Re_d > 400$ at this ϕ (Ch. 3).

Both $\langle\sigma_y^2(x)\rangle$ and $\mathrm{d}\langle\sigma_y^2\rangle/\mathrm{d}x$ decrease as Re_d decreases below $Re_d \approx 100$ at both

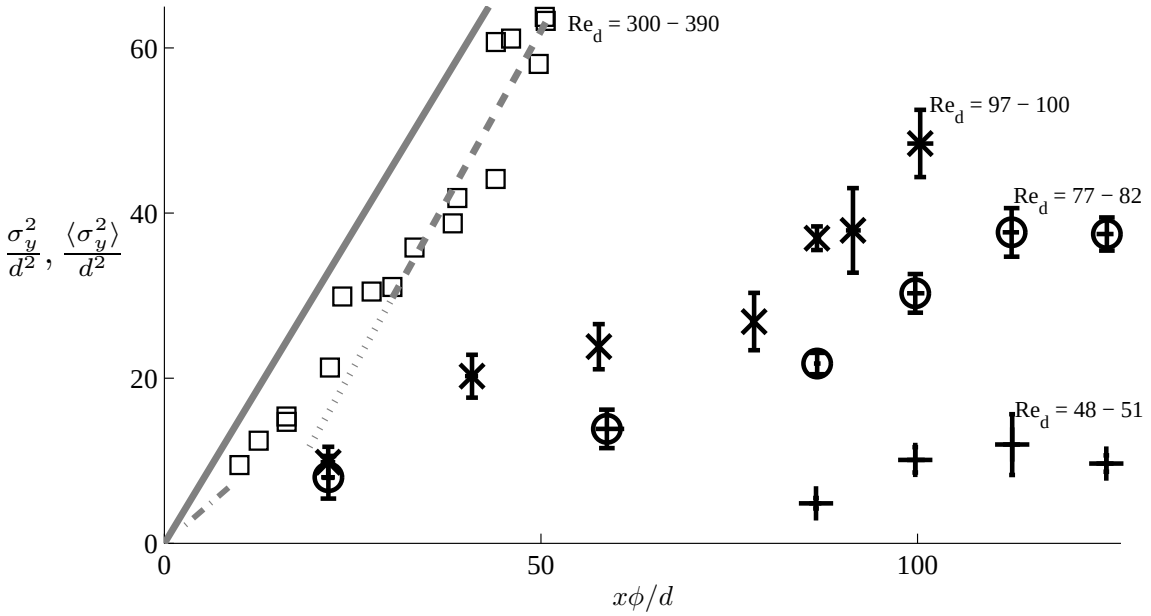

Figure 4-6: Evolution of the ensemble-averaged variance with normalized distance at $\phi = 0.35$: $Re_d = 48 - 51$ (+), 77 - 82 ($\circ$), and 97 - 100 ($\times$). Individual σ_y^2 measurements from experiments at $Re_d = 300 - 390$ (square) reported in Ch. 3 are also included. Each +, $\circ$, and $\times$ represents an average of four or more runs; horizontal bars indicate the range in x and vertical bars indicate the standard error of the mean. Solid line depicts $\mathrm{d}\langle\sigma_y^2\rangle/\mathrm{d}x = 0.34$ cm, as predicted for fully turbulent flow by Eq. (3.24), with scaling constants proposed in § 3.4.3. Dashed line is the least-squares fit to $\sigma_y^2\ (x)$ for $Re_d = 300 - 390$, $x\phi/d > 30$: $\mathrm{d}\sigma_y^2/\mathrm{d}x = 0.36 \pm 0.05$ cm ($R^2 = 0.86, n = 10$). Dotted line is its extrapolation to smaller x, for reference. Also included is $\left\langle\sigma_y^2\right\rangle/x = 0.28$ cm (dashed-dotted), as measured by Serra et al. (2004) at $46 < Re_d \leq 120$.

ϕ (figures 4-5 and 4-6). As depicted in figure 4-1, this Re_d dependence of $\mathrm{d}\langle\sigma_y^2\rangle/\mathrm{d}x$ at transitional Re_d is attributed to pre-asymptotic effects, i.e., the plume reached the measurement location before the solute particles experienced a sufficiently large subset of velocities in the array or, equivalently, before the solute particles dispersed over scales much larger than d and $\langle s_n\rangle_A$ [Eq. (4.4)]. A qualitatively similar increase of $\mathrm{d}\langle\sigma_y^2\rangle/\mathrm{d}x$ with $\langle\overline{u}\rangle/\nu$ at a fixed x, and subsequent $\langle\overline{u}\rangle/\nu$ independence at high $\langle\overline{u}\rangle/\nu$, have been observed in ceramic foam (Pereira et al., 2005; Hackert et al., 1996).

If the observed Re_d dependence of $\mathrm{d}\langle\sigma_y^2\rangle/\mathrm{d}x$ is indeed due to pre-asymptotic effects, then $\mathrm{d}\langle\sigma_y^2(x)\rangle/\mathrm{d}x$ is expected to approach its asymptotic value in fully turbulent flow at sufficiently large x ($= x_c$) (figure 4-1). At $(\phi, Re_d) = (0.20, 58-61)$, flow is steady and laminar [figure 4-2(a)], and the predicted $x_c\phi/d$ [$\sim 3\times10^4$, Eq. (4.4)] is two orders of magnitude larger than the length of the laboratory array ($x\phi/d = 88$). Accordingly, $\mathrm{d}\langle\sigma_y^2\rangle/\mathrm{d}x$ remains smaller than its asymptotic value at high Re_d ($= 310-340$) for all x considered (figure 4-5, $\cdot$). In contrast, at $(\phi, Re_d) = (0.20, 110-120)$, $\mathrm{d}\langle\sigma_y^2\rangle/\mathrm{d}x$ is equal to its asymptotic value at high Re_d within uncertainty at $x\phi/d > 30$, but deviates at $x\phi/d \leq 20$ (figure 4-5, $\times$). This trend indicates that asymptotic dispersion is reached in the range $20 < x_c\phi/d \leq 30$ at this (ϕ, Re_d). This distance is larger than $x_c\phi/d \sim 1$ predicted by Eq. (4.5) for fully turbulent flow, presumably because the flow was not fully turbulent at this Re_d ($= 110-120$) and the weaker turbulence intensity relative to fully turbulent flow extended x_c (cf. figure 4-1).

It is convenient to relate numerical values of C_{ms} to asymptotic/pre-asymptotic dispersion as interpreted directly from $\mathrm{d}\langle\sigma_y^2\rangle/\mathrm{d}x$. A threshold defined at $C_{ms} = 2.5\times10^{-3}$ cm^{-1} accurately segregates $(\phi, Re_d) = (0.20, 110-120)$ data in the asymptotic regime ($x\phi/d > 30$) from those in the pre-asymptotic regime ($x\phi/d \leq 20$), as determined above. With this threshold, $\langle C_{ms}\rangle$ for $(\phi, Re_d) = (0.20, 58-61)$ and $(0.20, 310-340)$ are also correctly classified into the pre-asymptotic and asymptotic dispersion regimes, respectively [figure 4-4(a)].

This criterion can now be applied to classify the remaining measurements, for which the anticipated transition from pre-asymptotic to asymptotic (large x) disper-

sion cannot be easily identified by eye (figures 4-5, 4-6). For example, the range of x over which $\mathrm{d}\sigma_y^2/\mathrm{d}x$ is constant is not obvious for $(\phi, Re_d) = (0.35, 300-390)$. However, $\langle C_{ms}\rangle$ at $(\phi, Re_d) = (0.35, 300-390)$ and $(0.20, 84-89)$ fall below the threshold at $x\phi/d > 30$ and ≥ 55, respectively, implying that the asymptotic regime had been reached at these x. Least-squares fit to data in the former yields $\mathrm{d}\sigma_y^2/\mathrm{d}x = 0.36 \pm 0.05$ cm ($R^2 = 0.86, n = 10$) (figure 4-6, dashed line). The correlation is highly significant, confirming that dispersion is indeed Fickian at $x\phi/d > 30$. Furthermore, the best-fit $\mathrm{d}\sigma_y^2/\mathrm{d}x$ is equal, within uncertainty, to that predicted for fully turbulent flow by Eq. (3.24), with scaling constants proposed in § 3.4.3 (figure 4-6, solid line). This agreement supports the conjecture that asymptotic (i.e., $x > x_c$) $\mathrm{d}\langle\sigma_y^2\rangle/\mathrm{d}x$ is independent of Re_d. In contrast, a linear regression at $55 \leq x\phi/d \leq 72$ for $(\phi, Re_d) = (0.20, 84-89)$ does not yield a significant correlation ($R^2 = 0.56, n = 3$). Since $\langle\sigma_y^2\rangle(x)$ measurements are constant within standard error in this range, the weak correlation is most likely due to measurements not extending sufficiently far into the asymptotic regime. Finally, $\langle C_{ms}\rangle$ (or C_{ms}) corresponding to (ϕ, Re_d, x) at which measured $\mathrm{d}\langle\sigma_y^2\rangle/\mathrm{d}x$ (or $\mathrm{d}\sigma_y^2/\mathrm{d}x$) was identified above to have occurred at the same rate as asymptotic dispersion in fully turbulent flow are plotted in grey in figure 4-4. The empirical boundary $\langle C_{ms}\rangle = 2.5 \times 10^{-3}$ cm^{-1} (dashed) accurately segregates the ensemble-averaged time-averaged concentration profiles in the asymptotic regime from those in the pre-asymptotic regime.

The above discussion suggests that dispersion is not likely to reach its asymptotic limit in dense vegetation in the field. A rough extrapolation of our laboratory data suggests that, at $Re_d \leq 60$, solute introduced in dense ($\phi > 0.19$) arrays must flow through a distance larger than $x\phi/d = 100$ before its dispersion becomes asymptotic (figure 4-4). This value corresponds to $x = 30$ m, for example, in a random array with the same $d(= 3$ cm) and $\phi(\approx 0.1)$ as measured by Lightbody et al. (2008) in a constructed wetland ($Re_d = 30-40$). This is a non-negligible distance in many aquatic systems, e.g., constructed wetlands (Kadlec, 1994), mangrove swamps (Furukawa et al., 1997; Kobashi and Mazda, 2005), and salt marshes (Neumeier and Amos, 2006), where homogeneous vegetation conditions extend no more than about

200 m perpendicular to land, and in some systems (Kadlec, 1994; Neumeier and Amos, 2006) much less. In particular, constructed wetlands typically comprise multiple cells of variable dimensions, and the shortest cell may only extend $30 - 300$ m streamwise (Keefe et al., 2004; Hey et al., 1994; Lightbody et al., 2008; Martinez and Wise, 2003).

4.4 Conclusions

The lateral distribution of passive solute released continuously from a point source was measured at $x/d = 59$ to 370 and $Re_d = 48$ to 120 in random cylinder arrays of solid volume fraction $\phi = 0.20$ and 0.35, and the results were compared with measurements at $Re_d = 300 - 390$ reported in Ch. 3. Previous predictions for fully turbulent flow imply that asymptotic (large x) lateral dispersion, $K_{yy}/(\langle\overline{u}\rangle d)$, will not exhibit a strong dependence on Re_d at these ϕ (Ch. 3). Measured $\mathrm{d}\left\langle\sigma_y^2\right\rangle/\mathrm{d}x$ and $\mathrm{d}\sigma_y^2/\mathrm{d}x$ reached asymptotic rates predicted for fully turbulent flow at $(\phi, Re_d) = (0.20, 110-120)$ and $(0.35, 300-390)$ at large x, supporting this conjecture. While the contribution of turbulent diffusion to lateral dispersion is expected to be negligible at long distances in dense arrays, it is apparent from flow visualization that turbulence substantially enhances pore-scale mixing, which in turn accelerates the approach to asymptotic dispersion. This Re_d dependence explains why dispersion at lower Re_d ($<$ 100) did not reach the fully turbulent flow limit within the length and width of the laboratory array.

Further, results suggest that at the same Re_d, the pre-asymptotic regime extends farther downstream at $\phi = 0.35$, in terms of the number of cylinders spanned ($x\phi/d$), than at $\phi = 0.20$. Concentration profiles within the asymptotic dispersion regime deviated from a Gaussian distribution by less than $\langle C_{ms}\rangle = 2.5 \times 10^{-3}$ cm^{-1} in both previous (Ch. 3) and present experiments. Using this as an empirical criterion, we can evaluate from time-averaged profiles at a single streamwise location whether dispersion at that distance is pre-asymptotic or asymptotic. This method requires significantly less effort than obtaining measurements at multiple streamwise positions to evaluate $\mathrm{d}\langle\sigma_y^2\rangle/\mathrm{d}x$.

Chapter 5

Conclusions

This thesis presented laboratory measurements of mean drag, integral length scale of turbulence, turbulence intensity, and lateral dispersion in random cylinder arrays under conditions relevant to aquatic plant canopies. The most important results are summarized below.

Previously, measurements of drag reported in the literature for a random cylinder array were limited to $0 \leq Re_d \leq 100$ at $\phi \geq 0.05$ and $Re_d \geq O(1000)$ at $\phi < 0.05$. This thesis provides the first measurements of mean drag at large ϕ (≥ 0.091) at $O(30) \leq Re_d \leq O(700)$ that include both laminar and turbulent flows. Drag per unit cylinder length $\left\langle \overline{f_D} \right\rangle$, when normalized by the mean interstitial velocity $\langle \overline{u} \rangle$ and viscosity μ, increases linearly with Re_d at all ϕ and Re_d considered in the present experiments. The same dependence was previously observed in random cylinder arrays at lower Re_d (≤ 100) (Koch and Ladd, 1997) and in packed beds of spheres (e.g., Kececioglu and Jiang, 1994; Ergun, 1952). The corresponding drag coefficient C_D increases with increasing ϕ at $Re_d \leq O(700)$. Given Nepf (1999)'s report of the opposite ϕ dependence at $Re_d \geq O(1000)$, it can be inferred that the ϕ dependence of C_D changes at $Re_d \approx 1000$, which coincides with the anticipated transition from laminar to turbulent cylinder boundary layer [see further discussion below (§ 5.1)]. Finally, the inertial contribution to the drag coefficient C_D is an input parameter in the classic scaling for turbulence intensity which, with the present drag measurements, could be verified (see below).

The integral length scale of turbulence, which has traditionally been regarded to be of the order of the cylinder diameter d in cylinder arrays (Raupach and Shaw, 1982; Raupach et al., 1991; Nepf, 1999), is constrained by the interstitial pore size in dense arrays. We proposed and experimentally verified that the spatial average of the integral length scale in dense random arrays is equal to the average spacing between nearest-neighboring cylinders. Laboratory measurements confirmed that the mean turbulence intensity in fully turbulent flow is a function only of the form drag coefficient, the solid volume fraction, and the ratio of the integral length scale of the turbulent eddies and the cylinder diameter. These scaling of the integral length scale and the mean turbulence intensity are expected to apply to random arrays of cylinders of different geometries, with differences in the geometry manifesting in the form drag coefficient.

The lateral variance of the concentration of solute at a given distance, x, from a point source is Re_d-independent at sufficiently high Re_d at all ϕ. The Re_d above which variance is Re_d-independent varies with ϕ, and is generally higher at larger ϕ. This transition to Re_d independence is attributed to the onset of fully turbulent conditions. The present study has revealed for the first time that asymptotic dispersion in this high-Re_d regime exhibits three distinct regimes. In particular, the measurements reveal an intermediate regime in which the dispersion coefficient K_{yy} decreases with increasing cylinder density. A scale model was developed for turbulent diffusion which, when superposed with existing models for dispersion due to the spatially-heterogeneous velocity field that arises from the presence of the cylinders, accurately captures the observed dependence of dispersion on cylinder density. Model predictions imply that, in dense ($\phi > 0.19$) arrays where turbulent diffusion is negligible, $K_{yy}/(\langle\overline{u}\rangle d)$ does not depend strongly on Re_d. This conjecture was confirmed experimentally for selected ϕ and $Re_d > 100$.

Although turbulent diffusion does not contribute significantly to $K_{yy}/(\langle\overline{u}\rangle d)$ in these dense arrays, turbulence substantially enhances pore-scale mixing. In unsteady laminar and turbulent flows at $\phi = 0.20$ and 0.35, the pre-asymptotic dispersion regime extends farther downstream at lower Re_d, which is attributed to weaker pore-

scale mixing.

5.1 Directions for future research

During the course of the research reported in this thesis, several questions were raised that remain open or are currently being investigated by other students. Key topics are discussed below.

Drag at lower ($Re_d < 100$) **and higher** ($Re_d > 1000$) **Reynolds numbers** Surprisingly, measured drag $\left\langle \overline{f_D} \right\rangle / (\mu \langle \overline{u} \rangle)$ is accurately described by a single linear regression over all Re_d considered at each ϕ, even though flow visualization and solute concentration measurements suggest that experimental conditions coincided with the transitional flow regime, namely, between steady laminar and fully turbulent flow regimes. In particular, the data set at $\phi = 0.20$ appears to have extended from the steady laminar flow regime and into the fully turbulent regime. The constant linear dependence of drag across the transitional flow regime suggests that at each ϕ, a single linear function between drag and Re_d may be valid over a Re_d range wider than those considered in this thesis – specifically, as low as $Re_d = O(5)$, below which the Re_d-dependence is no longer linear (Koch and Ladd, 1997), and as high as $Re_d = O(1000)$, above which the cylinder boundary layer is no longer laminar. However, Kececioglu and Jiang (1994) have proposed, specifically for randomly packed beds of spheres for which $\left\langle \overline{f_D} \right\rangle / (\mu \langle \overline{u} \rangle)$ also varies linearly with Re_d, that the coefficients of the linear function (α_0, α_1) differ between viscous-inertial laminar (Forchheimer) and turbulent flow regimes. Other authors have observed a similar shift in coefficients at high Re_d, but in the absence of turbulence (Soleymani et al., 2007). It would be insightful to determine experimentally the exact range of Re_d over which a single linear function of Re_d can describe the drag in a random cylinder array (at constant $d,\ \phi$).

Data at higher $Re_d > 1000$ can also be used to determine if the ϕ dependence of C_D reverses, i.e., if C_D decreases with increasing ϕ, at $Re_d \geq O(1000)$. Recall

that a decreasing C_D was observed by Nepf (1999) for smaller $\phi = 0.006 - 0.06$ at all Re_d (> 1000) considered.

Dispersion in Stokes flow To my knowledge, lateral dispersion in Stokes flow through random cylinder arrays has not been measured in laboratory experiments or numerical simulations. Several models have been proposed in the literature for lateral dispersion in Stokes flow, specifically by Nepf (1999) [Eq. (3.19)], Koch and Brady (1986) [Eq. (3.20)], and Serra et al. (2004). For completeness, these models should be compared with experiment. In particular, Koch and Brady (1986)'s solution is expected to overestimate $K_{yy}/(\langle\overline{u}\rangle d)$ in Stokes flow by a factor of $1/\gamma_2 \approx 3.0$ and to diverge from experiment as ϕ approaches zero (Ch. 3). It would be useful to confirm the overestimation and to see at what ϕ the divergence occurs, from which we can evaluate the appropriateness of the adjustment we made to Eq. (3.20) to obtain a finite expression [Eq. (3.22)].

The transition from steady laminar to turbulent flow Very little has been reported about flow in random arrays at transitional Re_d, i.e., between steady laminar flow and turbulent flow. Indeed, the classification of a flow as laminar or turbulent is itself difficult, because the cylinders are distributed randomly and, consequently, local flow conditions vary spatially. Therefore, the onset of unsteadiness and turbulence is expected to occur gradually as Re_d is increased, with different regions of the array becoming unsteady and turbulent at different Re_d. Further, it seems possible at sufficiently high ϕ for several neighboring cylinders to be distributed in such a way that a (laminar) recirculation zone is maintained at all Re_d, even when the rest of the domain is turbulent. Physical reasoning and qualitative observations also suggest that certain phenomena observed at low ϕ may not occur at high ϕ. For example, as discussed in § 4.3.1, it seems likely that the close proximity and the random distribution of the cylinders would suppress periodic oscillation of near wakes and periodic vortex shedding in sufficiently dense arrays.

Finally, periodic oscillations differ fundamentally from turbulent motion, and it

would be interesting to investigate how periodic motion of the wake in unsteady laminar flow, at ϕ in which such a flow regime occurs, affects microscopic and macroscopic solute transport. These changes will be reflected in, e.g., x_c and $K_{yy}/(\langle\overline{u}\rangle d)$.

Discontinuities in the array Investigation of flow in a discontinuous cylinder array is an obvious extension of this thesis. To this end, previous studies (White, 2006; Lightbody, 2007) have already explored different configurations. In the field, plant canopies are restricted to finite horizontal area and their boundaries with open water are non-negligible in modeling the aquatic system. For example, field studies report that some species predominantly reside near the boundary between a salt marsh and open water (e.g., Peterson and Turner, 1994). Investigation of the flow near the interface between a confined cylinder array and an adjacent unobstructed region may yield important insights into biological activity in such regions. Also, transverse bands of deep zones, which are typically sparsely vegetated, are sometimes introduced in artificial treatment wetlands to promote contaminant removal (see Lightbody, 2007 for a summary of previous studies). The effects of discontinuity on solute transport must first be identified before the role of deep zones, which introduce not only a discontinuity in the array but also depth variation, can be fully understood.

The simplest configuration that can be considered is an "infinite" two-dimensional cylinder array with a gap in the middle (figure 5-1). Even for this configuration, a systematic investigation of flow and transport has not been undertaken, to my knowledge. Preliminary LDV measurements of the longitudinal component of the laterally-averaged velocity, turbulence intensity, and integral length scale of turbulence remained unchanged within experimental uncertainty as gap length was increased from $\Delta x_{gap}/\langle s_n\rangle_A = 0.2$ to 8.1 ± 0.4 (figure 3-2, $\phi = 0.20$, $Re_d = 430$ to 540) in a random array. Selected measurements have also been collected by various authors in the reversed system - where an array of finite length is placed in an otherwise unobstructed flow (e.g., Finelli, 2000). For

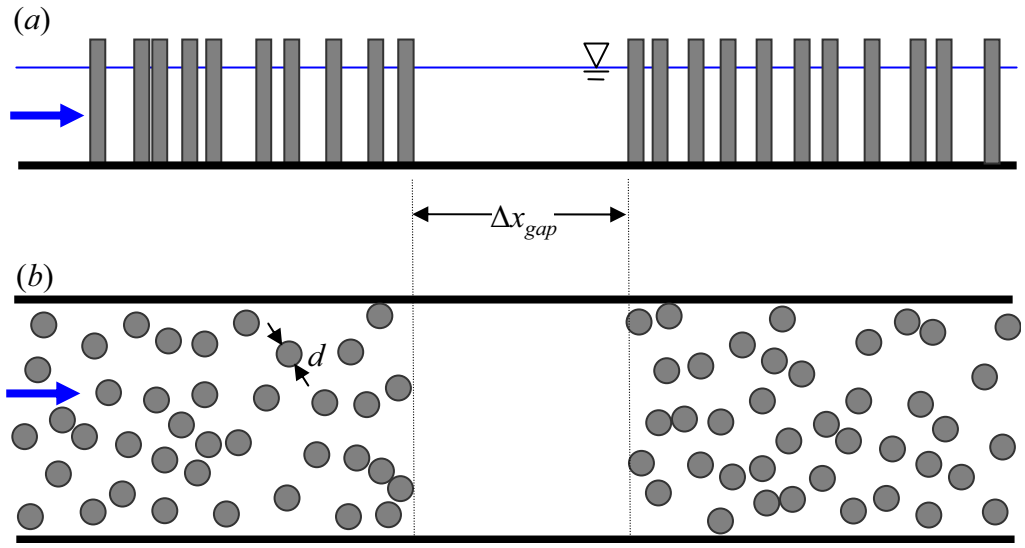

Figure 5-1: (a) Side and (b) plan view of an array of randomly-distributed emergent cylinders with a gap of width Δx_{gap} in the middle that spans the width of the array. Not to scale. The blue arrows indicate the direction of mean flow.

example, Nakajyo et al. (2007, $Re_d = 258$) observed that the turbulent kinetic energy remains relatively constant over the first $x = 2d$ downstream of an array of spheres, where d is the sphere diameter, then decays smoothly until it reaches background levels at approximately $x = 4d$ downstream of the array. Pluntke and Kozerski (2003) report, but do not explain, a distinct peak in bed shear stress at the downstream edge of an artificial plant canopy.

Research in streamwise-discontinuous arrays will complement research on discrete clusters of cylinders, where the spatial discontinuity is two-dimensional. Several studies report flow measurements in clusters of various shapes (Bennett, 2004; Ohmoto and Tanaka, 2007; Rominger, 2008, personal comm.).

Field measurements of plant canopy properties In the interest of reducing parameters, my dissertation research was restricted to flow around randomly-distributed cylinders. However, model predictions of $K_{yy}/(\langle\overline{u}\rangle d)$ is sensitive to nearest-neighbor separation of the cylinders, $\langle s_n \rangle_A$ (cf. Appendix E), which implies that solute transport will differ significantly in two arrays with a different cylinder configuration, even if ϕ is the same. To my knowledge, no field study

has recorded the *spatial distribution* of plant stems in a natural system; field reports typically only provide the ϕ or the leaf area index. This information will also be invaluable to researchers who conduct laboratory experiments using live plants, e.g., to measure plant drag, who must decide how to distribute the plants in their experimental facility to most closely mimic field conditions.

Flow and transport at the stem scale Epiphytic periphyton appears to be ubiquitous in natural aquatic systems (e.g., Neumeier and Ciavola, 2004). Moreover, Cornelisen and Thomas (2004) report that on average, 72% of the leaf surface in a seagrass bed was covered by epiphytes. Given such densities, it is reasonable to assume that the presence of epiphytes on plant stems will influence nutrient uptake where diffusion across the boundary layer is the rate-determining step in nutrient uptake (e.g., Thomas et al., 2000). Epiphytes introduce roughness to the plant surface, which may increase or decrease the thickness of the boundary layer by, e.g., dissipating ambient turbulence in its vicinity, or by contributing additional turbulence at the scale of individual epiphyte elements (Koch, 1994). Also, an isolated protrusion alters the local flow field by deflecting flow both perpendicular and parallel to the (plant) surface (e.g., Eckman and Nowell, 1984). Above some critical density of protrusions, "skimming flow" develops, where the ambient current flows over the external envelope of the protrusions instead of through it. A systematic laboratory investigation of how the force on and the flow signatures around a cylinder vary with the height, geometry, and density of attached roughness elements will yield insight into local flow experienced by plants, as well as the hydrodynamic significance of epiphytes to canopy-scale properties such as residence time, mean drag, net nutrient uptake, and net suspended particle removal.

Particle transport in plant canopies While an extensive collection of field studies that investigate the effect of vegetation on sediment transport exist, many are inconclusive. For example, Shi et al. (2000) found suspended sediment concentration to be lower within a salt marsh than in an adjacent mudflat with

no vegetation, and conclude that deposition was enhanced within the marsh. However, Neumeier and Ciavola (2004) report reduced sedimentation to the bed within a salt marsh compared to unvegetated regions. The apparent contradiction can be explained if the lower concentration is attributed to (i) sediment removal before the water enters the vegetated region or (ii) incoming flow preferentially flowing over the mudflat instead of through the salt marsh. Indeed, the latter is consistent with the lower flow velocity measured in the salt marsh. Therefore, the lower concentration observed by Shi et al. (2000) may merely have been a manifestation of reduced influx into the canopy, instead of enhanced sediment removal rate within the canopy.

The enhancement of suspended particle removal through deposition onto the exposed plant surface appears to have received little consideration in literature, despite laboratory (Pluntke and Kozerski, 2003) and field (Stumpf, 1983) measurements that demonstrate its importance. These works suggest that studies that only consider sedimentation to the bed may significantly underestimate net particle removal within a plant canopy. In the laboratory, we can prevent flow diversion and measure suspended sediment flux into and out of a model canopy, thereby isolating the various mechanisms that occur in real systems. Recently, López and García (1998) demonstrated numerically that the depth-integrated mass flux of suspended sediment is reduced in channels without horizontal flow diversion with submerged rigid vegetation, which they attribute to a reduction in bed shear stress.

In particular, predicting the occurrence of flow diversion is critical, as it also affects mean turbulence intensity. If all flow is forced through the canopy, the presence of plants will enhance mean turbulence intensity at high Reynolds number (Ch. 3). However, field studies often report lower turbulence intensity within a canopy compared to adjacent open water, which may be attributed to flow diversion and the associated reduction in mean flow velocity. A reduction in turbulence intensity promotes particulate deposition. Indeed, Gacia et al.

(1999) report much greater resuspension from a bare sand bed than from an adjacent seagrass bed.

Appendix A

Reynolds number-dependence of the lateral variance of the concentration distribution[a]

The variance of the time-averaged concentration profiles, σ_y^2, for selected (x, ϕ) are plotted against Re_d and $Re_{\langle s_n \rangle_A}$ in figures A-1 and A-2, respectively. Ensemble-averaged variance, $\langle \sigma_y^2 \rangle$, are presented where more than four measurements were collected for the same (x, Re_d, ϕ). At a given (x, ϕ), $\langle \sigma_y^2 \rangle$ increases rapidly with increasing Re_d at low Re_d and subsequently becomes approximately constant above a certain Re_d. For example, at $\phi = 0.20$, $\langle \sigma_y^2 \rangle$ increases rapidly from $Re_d \approx 30$ to $Re_d \approx 100$ and is constant above $Re_d \approx 200$. At $\phi = 0.031$, the Re_d-independent regime appears to start at a lower $Re_d \approx 110 - 120$. In contrast, at $\phi = 0.35$, a Re_d-independent regime was not observed at conditions considered in the present study ($Re_d < 400$). For example, data at $x = 90 - 94$ cm (green $\times$) are clearly smaller at $Re_d = 180$ than at $Re_d = 320$. These observations suggest that $\langle \sigma_y^2 \rangle$ becomes Re_d-independent above a critical Re_d that is, in general, larger at larger ϕ. $Re_{\langle s_n \rangle_A} > 74$ is a conservative empirical criterion that accurately captures only the Re_d-independent measurements across all ϕ (figure A-2, dashed line).

[a] A preliminary version of figures A-1 and A-2 appears in Tanino and Nepf, 2007, where a subset of the data were plotted against Re_s.

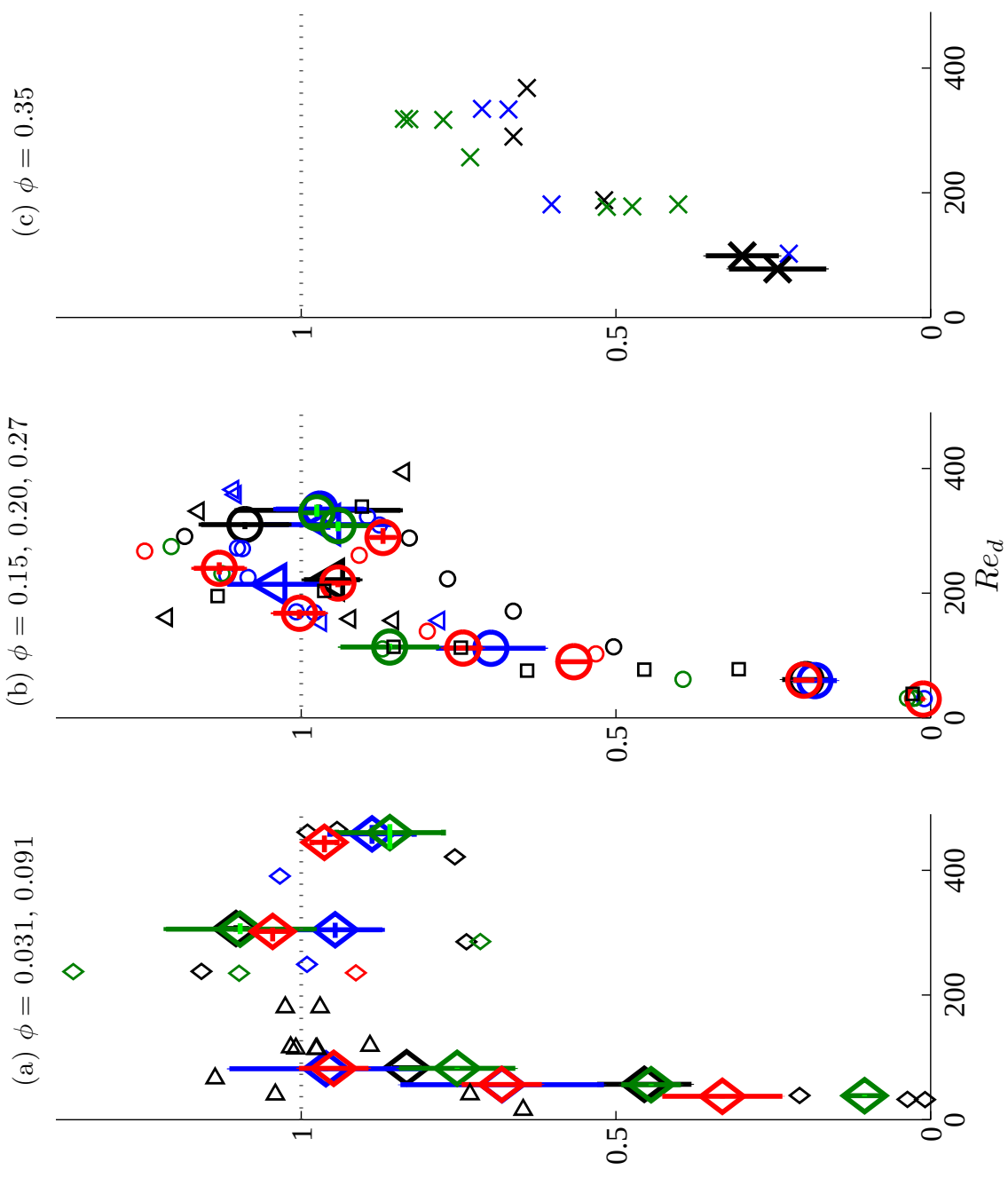
(a) $\phi = 0.031, 0.091$
(b) $\phi = 0.15, 0.20, 0.27$
(c) $\phi = 0.35$
1
0.5
0
0
200
400
Re_d

Figure A-1 *(facing page)*: Re_d dependence of the lateral variance of the concentration distribution, σ_y^2 as defined by Eqs. (4.1) and (4.2), at selected x for $\phi =$ (a) 0.031 ($\triangleright$), 0.091 ($\diamond$), (b) 0.15 (square), 0.20 ($\circ$), 0.27 (Δ), and (c) 0.35 ($\times$). σ_y^2 is normalized by the mean of σ_y^2 measurements at $Re_{\langle s_n \rangle_A} > 74$ at that (x, ϕ). For $\phi = 0.35$, for which data are not available at $Re_{\langle s_n \rangle_A} > 74$, σ_y^2 is normalized by the product of $\mathrm{d}\langle\sigma_y^2\rangle/\mathrm{d}x$ predicted for fully turbulent flow by Eq. (3.24), with scaling constants as proposed in Ch. 3, and x. For each ϕ, different marker colors indicate different x: $(\phi, x$ [cm]) = (0.091, 30-32) (black $\diamond$); (0.091, 50-53) (blue $\diamond$); (0.091, 59-62) (green $\diamond$); (0.091, 81-85) (red $\diamond$); (0.15, 140-142) (black square); (0.20, 50-53) (black $\circ$); (0.20, 96-100) (blue $\circ$); (0.20, 123-126) (green $\circ$); (0.20, 140-143) (red $\circ$); (0.27, 39-41) (black $\triangle$); (0.27, 69-71) (blue $\triangle$); (0.35, 38-41) (black $\times$); (0.35, 69-71) (blue $\times$); (0.35, 90-94) (green $\times$). There is a σ_y^2 measurement at (Re_d, normalized σ_y^2) = $(239, 1.7)$ for $(\phi, x$ [cm]) = $(0.091, 50-53)$ that is not visible. For readability, where there are four or more σ_y^2 measurements at the same (x, Re_d, ϕ), the measurements are represented by their mean. Each marker with a bold outline represents such an average; the horizontal and vertical bars indicate the range in Re_d over these replicate measurements and the standard error of the mean, respectively.

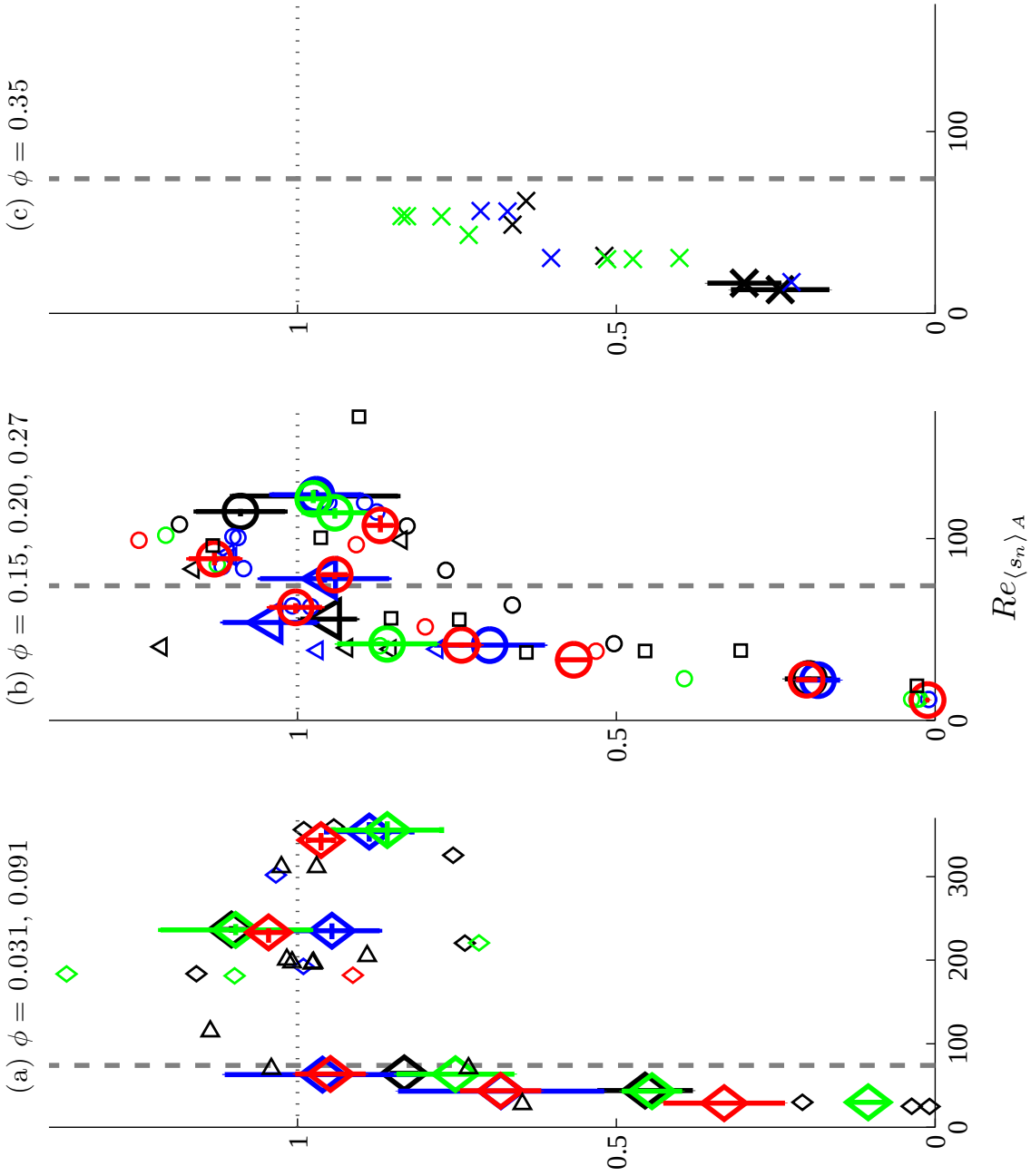

Figure A-2: $Re_{\langle s_n \rangle_A}$ dependence of σ_y^2, as defined by Eqs. (4.1) and (4.2), at selected x. Markers denote the same (ϕ, x) as in figure A-1. Above $Re_{\langle s_n \rangle_A} = 74$ (dashed line), $\langle \sigma_y^2 \rangle$ is approximately Re_d-independent.

Appendix B

Comparison of the longitudinal and lateral velocity fluctuations[a]

Three-dimensional ADV (SonTek, Inc.) measurements demonstrate that $\overline{v'^2} \approx \overline{u'^2}$. Specifically, $\sqrt{\overline{v'^2}}/\sqrt{\overline{u'^2}} = 0.97 \pm 0.14$ (s.d.), based on 428 measurements by White (2002, $\sqrt{\overline{u'^2}}$, $\sqrt{\overline{v'^2}}$ data provided by B. L. White, personal comm.) and 83 preliminary measurements from the present study (figure B-1).

[a]This material has been published in Tanino and Nepf, 2007. This material is based on work supported by the National Science Foundation grant EAR-0309188. Any opinions, conclusions, or recommendations expressed in this material are those of the authors and do not necessarily reflect the views of the National Science Foundation. The authors thank Brian L. White for providing unpublished ADV measurements from his Master's thesis (White, 2002).

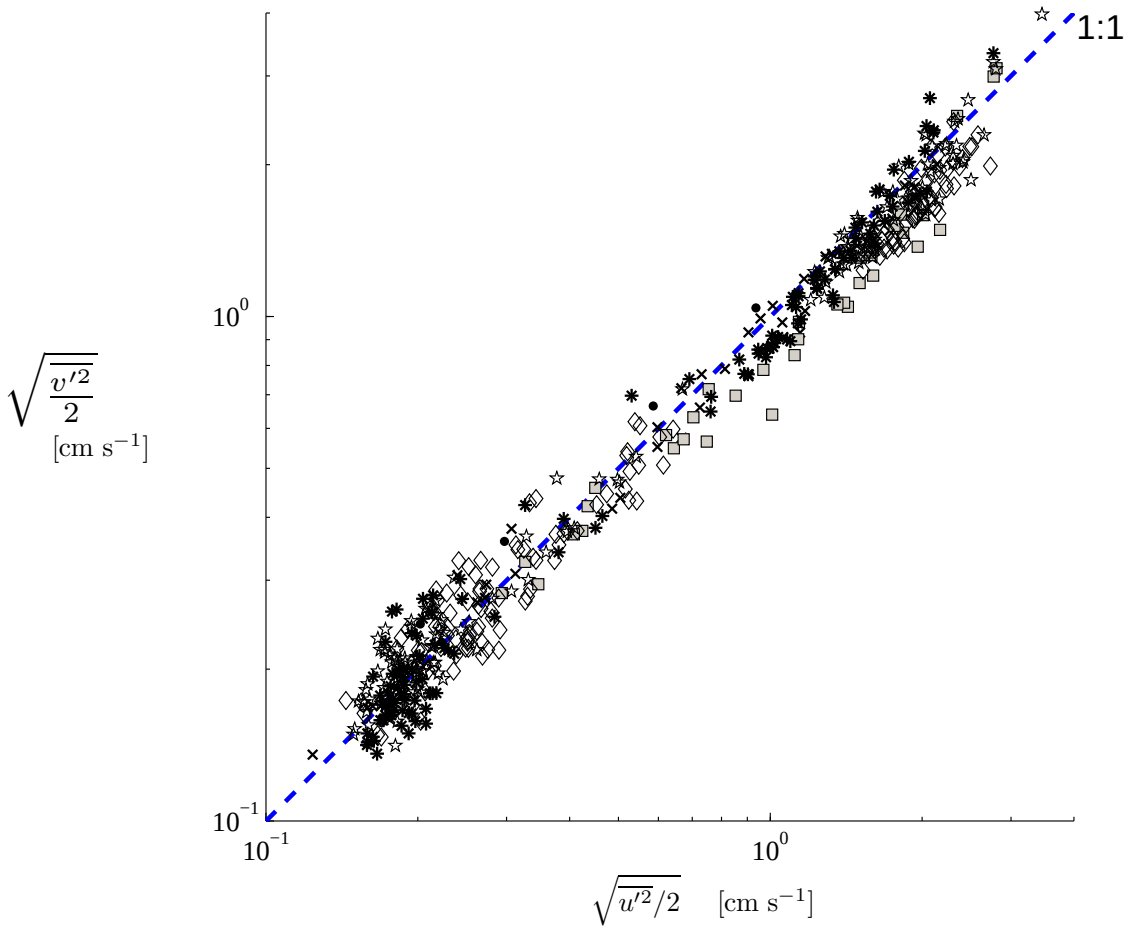

Figure B-1: Comparison of $\sqrt{\overline{u'^2}/2}$ and $\sqrt{\overline{v'^2}/2}$ calculated from ADV measurements by White (2002, $\sqrt{\overline{u'^2}}$, $\sqrt{\overline{v'^2}}$ data provided by B. L. White, personal comm.) at $\phi = 0.010$ ($*$), 0.020 ($\star$), and 0.063 ($\diamond$) and in the present study at $\phi = 0.031$ ($\cdot$), 0.091 (square), and 0.20 ($\times$). This figure is Tanino and Nepf, 2007, figure 3.

Appendix C

Comparison of the integral length scale of turbulence estimated from the power spectral density and from the autocorrelation function[a]

There are several standard techniques for estimating the integral length scale of turbulence from an Eulerian time record of turbulent fluctuations; for a summary, see, e.g., Barrett and Hollingsworth, 2001; Pearson et al., 2002; Burattini et al., 2005. One method is to approximate the integral length scale as the length scale associated with the peak in the frequency-weighted power spectrum [Eq. (3.28)]. A length scale may also be derived directly from the one-dimensional autocorrelation function [Eq. (3.29)]. The two definitions yield similar values when applied to our LDV measurements of $u'(t)$ (figure C-1).

[a]This material has been published in Tanino and Nepf, 2008c.

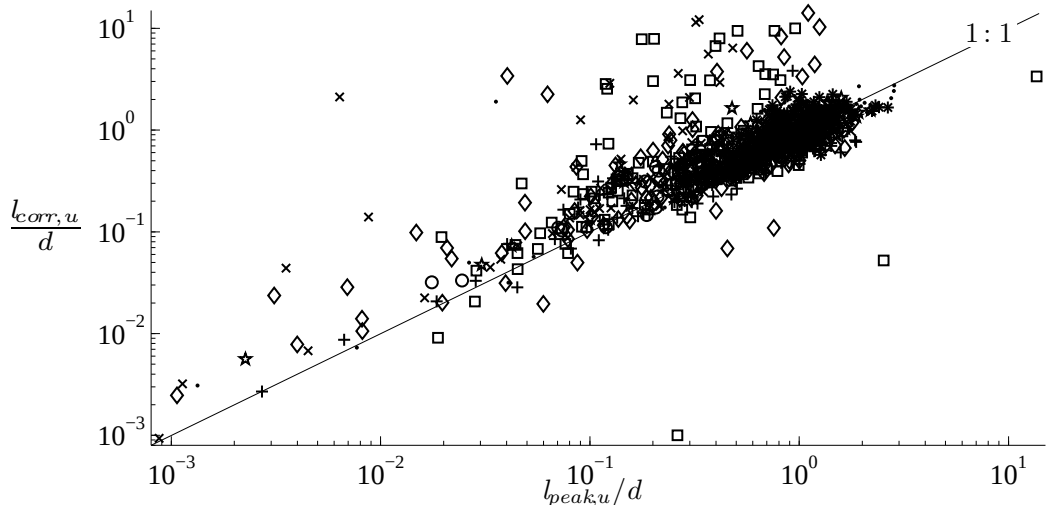

Figure C-1: Comparison of $l_{peak,u}$ [Eq. (3.28)] and $l_{corr,u}$ [Eq. (3.29)] determined from LDV measurements at $Re_{\langle s_n \rangle_A} > 105$ and $\phi = 0.010$ ($*$), 0.020 (star), 0.031 ($\cdot$), 0.060 ($\diamondsuit$), 0.091 ($+$), 0.15 (square), 0.20 ($\times$), and 0.35 ($\circ$).

Appendix D

Mean Nearest Neighbor Separation and Related Parameters in a Random Array[a]

Consider an array of N circular holes of diameter d randomly distributed in a board of horizontal area A, with corresponding hole volume fraction $\phi = (\pi/4)d^2N/A$. This array is created by generating uniformly distributed random coordinates for the hole centers. If a random coordinate is sufficiently far from previously assigned holes, that coordinate is assigned as a hole center and the appropriate area around it is marked as occupied. The process is repeated until N hole centers are assigned. Let N_c be the number of random coordinates that has to be generated to assign the N hole centers.

To derive an analytical expression for N_c, consider the generation of the i^{th} random coordinate. At this point, $(i-1)$ coordinates have been generated, out of which, on average, $(i-1)N/N_c$ would have been assigned as a hole center. Then, the total area "invalidated" by previously assigned holes is approximately $(i-1)(N/N_c)A_h$, where A_h is the area around a hole center in which another hole center cannot be assigned (referred to as the "invalid" area around a hole center). Note that this ap-

[a] A condensed version of this chapter has been published as Appendix A of Tanino and Nepf, 2008c. David Gonzalez-Rodriguez contributed the approach employed in the theoretical analysis presented in this Appendix.

proximation assumes that the invalid areas do not overlap, and is only appropriate at small ϕ. This approximation tends to overestimate N_c. Then, the probability that the i^{th} random coordinate is generated in an invalid area is $(i-1)(N/N_c)A_h/A$. Then, the total number of generated random coordinates that must be neglected, $N_c - N(\geq 0)$, is

$$N_c - N = \sum_{i=1}^{N_c} \frac{(i-1)(N/N_c)A_h}{A}. \tag{D.1}$$

Solving for N_c yields

$$\frac{N_c}{N} = \frac{1-(2\phi/N)A_h/(\pi d^2)}{1-2\phi A_h/(\pi d^2)}. \tag{D.2}$$

Note that this solution correctly collapses to unity when $A_h = 0$, i.e., when the holes are points. Theoretically, the invalid area around a hole center is a circle of radius d. Then, $A_h = \pi d^2$.

The generation of random coordinates within a small region of the array satisfies the two conditions of a Poisson process.[b] First, the expected number of random coordinates generated per unit area is constant at $\lambda > 0$, where

$$\lambda \equiv \frac{N_c}{A} = \frac{\phi}{(\pi/4)d^2}\frac{N_c}{N}. \tag{D.3}$$

Second, the number of hole centers in two non-overlapping areas within a small region of the array can be assumed independent. Then, the number of random coordinates generated in a circular area a has a Poisson distribution with parameter λa (Devore, 2000, pp. 136–137). Also, the circular area concentric with a random coordinate and spanning to its nearest random coordinate has an exponential probability distribution function (p.d.f.) (Bertsekas and Tsitsiklis, 2002; Devore, 2000, pp.174-175):

$$f_0(a;\lambda) = \begin{cases} \lambda e^{-\lambda a}, & a \geq 0 \\ 0, & a < 0 \end{cases}. \tag{D.4}$$

[b] A Poisson process is commonly associated with the occurrence of a particular event over time. Here, each random coordinate represents a single event occurring at some particular point in two dimensional space. Here, instead of time, we consider radial area, a, from an arbitrary origin in the region. Note that we consider hole center coordinates and not holes, because the events cannot have a finite volume.

In the array, each assigned hole occupies a finite circular area of radius $d/2$, and the smallest possible distance between non-overlapping hole centers is d. Then, the p.d.f. of the circular area concentric with a hole center and spanning to its nearest neighbor hole center, A_n, is truncated at $a = A_L$:

$$f(a;\lambda) = \frac{1}{\beta}\begin{cases} \lambda \mathrm{e}^{-\lambda a}, & a \geq A_L \\ 0, & a < A_L \end{cases}, \tag{D.5}$$

where

$$\beta = \int_{A_L}^{\infty} \lambda \mathrm{e}^{-\lambda a} \mathrm{d}a = \mathrm{e}^{-\lambda A_L} \tag{D.6}$$

and $A_L = \pi d^2$. A change of variables yields the p.d.f. for the center-to-center distance between nearest neighbors, s_{nc}, in terms of the p.d.f. for $A_n (= \pi {s_{nc}}^2)$:

$$f(r;\lambda) = f(a;\lambda)\frac{\mathrm{d}a}{\mathrm{d}r} = 2\pi r f(a;\lambda), \tag{D.7}$$

where r is the radial distance from a hole center, i.e., $a = \pi r^2$. Although A_L and A_h are equal here, the two parameters are not interchangeable, as will be shown in § D.1. A_L is, by definition of Eq. (D.5), a circular area that defines the smallest a for which $f(a;\lambda)$ is non-zero. In contrast, A_h does not assume a geometry for the invalid area around an assigned hole.

The above distributions describe the value measured by taking an array of randomly distributed hole centers, selecting one hole center, and finding its nearest neighbor and the corresponding s_{nc} and A_n. Additional values would be measured by repeating these steps in different, independent arrays. This process is different from identifying the nearest neighbor of, and measuring the corresponding s_{nc} and A_n for, each hole center in a single array, where measurements are dependent. This difference arises because if i is the nearest neighbor of hole j, then i must have a nearest neighbor no farther than the distance to j. Clearly, a similar dependence does not exist between measurements taken in different arrays. While the two random variables have different distributions, their mean is the same. Thus, $\int_{-\infty}^{\infty} r f(r) \mathrm{d}r$ and $\int_{-\infty}^{\infty} a f(a) \mathrm{d}a$ yield the correct mean distance $\langle s_{nc} \rangle_A$ and mean radial area $\langle A_n \rangle_A$ to

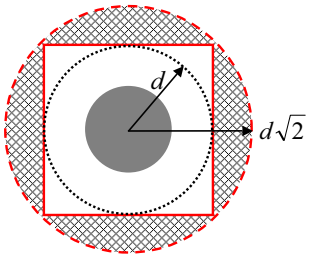

Figure D-1: Definition of invalid area around an assigned hole center. Physically, the area invalidated by the finite volume of the hole (solid circle) is the dotted circle, radius d. However, a $2d \times 2d$ square around a hole center was defined as invalid space in the numerical code used to assign the hole coordinates in the PVC sheets used in the laboratory experiments. The dashed circle marks the circle that circumscribes this square region.

the nearest neighboring hole center. From Eqs. (D.5), (D.6), and (D.7), the expected value for s_{nc} and ${s_{nc}}^2$ are

$$\frac{\langle s_{nc} \rangle_A}{d} = \sqrt{\frac{A_L}{\pi d^2}} + \frac{1 - \mathrm{erf}(\sqrt{\lambda A_L})}{2\sqrt{\lambda d^2}\mathrm{e}^{-\lambda A_L}} \tag{D.8}$$

and

$$\frac{\langle {s_{nc}}^2 \rangle_A}{d^2} \equiv \frac{\langle A_n \rangle_A}{\pi d^2} = \frac{A_L}{\pi d^2} + \frac{1}{\lambda \pi d^2}. \tag{D.9}$$

Applying $A_L, A_h = \pi d^2$, Eq. (D.2), and Eq. (D.3) to Eqs. (D.8) and (D.9) yields

$$\frac{\langle s_{nc} \rangle_A}{d} \approx 1 + \frac{\sqrt{\pi}}{2}\sqrt{\frac{1-2\phi}{4\phi}}\frac{\left[1 - \mathrm{erf}\left(\sqrt{4\phi/(1-2\phi)}\right)\right]}{\mathrm{e}^{-4\phi/(1-2\phi)}} \tag{D.10}$$

and

$$\frac{\langle {s_{nc}}^2 \rangle_A}{d^2} \approx \frac{1+2\phi}{4\phi}. \tag{D.11}$$

D.1 Invalid area defined as a $2d \times 2d$ square

In creating the PVC sheets used in this study, a $2d \times 2d$ square circumscribing each assigned hole was invalidated instead of a concentric circle of radius d (figure D-1).

Here, $A_h = (2d)^2$ instead of $A_h = \pi d^2$, and Eq. (D.2) yields

$$\frac{N_c}{N} = \frac{1 - 2d^2/A}{1 - (8/\pi)\phi} \approx \frac{1}{1 - (8/\pi)\phi}. \tag{D.12}$$

In the present laboratory experiments, $d^2/A = 1.4\times10^{-4}$ and the above approximation is valid. Note that the restriction to insure a positive N_c/N is $\phi < \pi/8$. The shape of the invalidated area is irrelevant to the calculation of N_c/N. The corresponding λ is determined by substituting Eq. (D.12) into Eq. (D.3).

The p.d.f. is $f(a;\lambda) = 0$ in the region $r < d$ and of the same form as $a \geq A_L$ in Eq. (D.5) in the region $r \geq d\sqrt{2}$. Between these two concentric circles, i.e. $d \leq r < d\sqrt{2}$, $f = 0$ inside the $2d \times 2d$ square. Accordingly, in this region Eq. (D.5) must be weighted by the ratio of the area that is outside the invalid square (shaded area in figure D-1) and the total area. Consider a circle of radius r, such that $d \leq r < d\sqrt{2}$. The total perimeter of the circle is $2\pi r$, of which $8(r \arccos(d/r))$ remains outside of the square. The ratio, $4\arccos(d/r)/\pi$, correctly becomes zero at $r = d$ and 1 at $r = d\sqrt{2}$. The p.d.f. is

$$f(a;\lambda) = \frac{1}{\beta}\begin{cases} \lambda \mathrm{e}^{-\lambda a}, & a \geq \pi(d\sqrt{2})^2 \\ \lambda \mathrm{e}^{-\lambda a}\frac{4}{\pi}\arccos\left(d\sqrt{\frac{\pi}{a}}\right), & \pi d^2 \leq a < \pi(d\sqrt{2})^2 \\ 0, & a < \pi d^2 \end{cases}, \tag{D.13}$$

where

$$\beta = \int_{\pi(d\sqrt{2})^2}^{\infty} \lambda \mathrm{e}^{-\lambda a}\mathrm{d}a + \int_{\pi d^2}^{\pi(d\sqrt{2})^2} \lambda \mathrm{e}^{-\lambda a}\frac{4}{\pi}\arccos\left(d\sqrt{\frac{\pi}{a}}\right)\mathrm{d}a. \tag{D.14}$$

Because the second integral in Eq. (D.14) cannot be solved analytically, an approximate method is required. One possible approach is to define an equivalent circle of radius r_e with the same contribution to $\langle s_{nc}\rangle_A$ (figure D-1). r_e must satisfy:

$$\int_0^{r_e} r f(a)\ \mathrm{d}a = \int_{y=-d}^{d}\int_{x=-d}^{d} \sqrt{x^2+y^2} f(a)\ \mathrm{d}x\ \mathrm{d}y. \tag{D.15}$$

To simplify the computation, we approximate $f(a) = 1$, which reduces Eq. (D.15) to

$$\frac{r_e}{d} = \left\{ \frac{2}{\pi} \left[\sqrt{2} + \ln(1+\sqrt{2}) \right] \right\}^{1/3}. \tag{D.16}$$

Note that $1 < r_e/d < \sqrt{2}$, as expected. Now, the invalid area has been transformed from a $2d \times 2d$ square to a circle of radius r_e concentric to a hole center. The corresponding p.d.f. is the same as Eq. (D.5), but with

$$A_L = \pi {r_e}^2 = \pi d^2 \left\{ \frac{2}{\pi} \left[\sqrt{2} + \ln(1+\sqrt{2}) \right] \right\}^{2/3}. \tag{D.17}$$

Substituting λ and Eq. (D.17) into Eqs. (D.8) and (D.9) yields

$$\begin{aligned} \frac{\langle s_{nc} \rangle_A}{d} \approx & \left\{ \frac{2}{\pi} \left[\sqrt{2} + \ln(1+\sqrt{2}) \right] \right\}^{1/3} \\ & + \frac{1 - \operatorname{erf}\left(\sqrt{\frac{4\phi}{1-(8/\pi)\phi}} \left\{ \frac{2}{\pi} \left[\sqrt{2} + \ln(1+\sqrt{2}) \right] \right\}^{2/3} \right)}{2\mathrm{e}^{-4\phi/[1-(8/\pi)\phi]\left\{(2/\pi)\left[\sqrt{2}+\ln(1+\sqrt{2})\right]\right\}^{2/3}}} \sqrt{\pi} \sqrt{\frac{1-(8/\pi)\phi}{4\phi}} \end{aligned} \tag{D.18}$$

and

$$\frac{\langle {s_{nc}}^2 \rangle_A}{d^2} \approx \frac{1-(8/\pi)\phi}{4\phi} + \left\{ \frac{2}{\pi} \left[\sqrt{2} + \ln(1+\sqrt{2}) \right] \right\}^{2/3}. \tag{D.19}$$

For reference, the above solutions for $\langle s_{nc} \rangle_A / d$ and $\langle {s_{nc}}^2 \rangle_A / d^2$ are plotted in figure D-2.

D.1.1 Other relevant parameters

Previously, the mean of all s_{nc}/d and ${s_{nc}}^2/d^2$ were determined. Repeating the calculation with $A_L = \pi {r^*}^2$, where $r^* \geq r_e$ is an arbitrary distance, yields the conditional mean only of $s_{nc} > r^*$ in the random array. Applying λ and the redefined A_L to Eqs. (D.8) and (D.9) yields

$$\frac{\langle s_{nc} \rangle_{s_{nc} > r^*}}{d} = \frac{r^*}{d} + \frac{\sqrt{\pi}}{4} \frac{1 - \operatorname{erf}\left\{ 2r^*/d \sqrt{\phi/[1-(8/\pi)\phi]} \right\}}{\sqrt{\phi/[1-(8/\pi)\phi]}\mathrm{e}^{-(r^*/d)^2 4\phi/[1-(8/\pi)\phi]}} \tag{D.20}$$

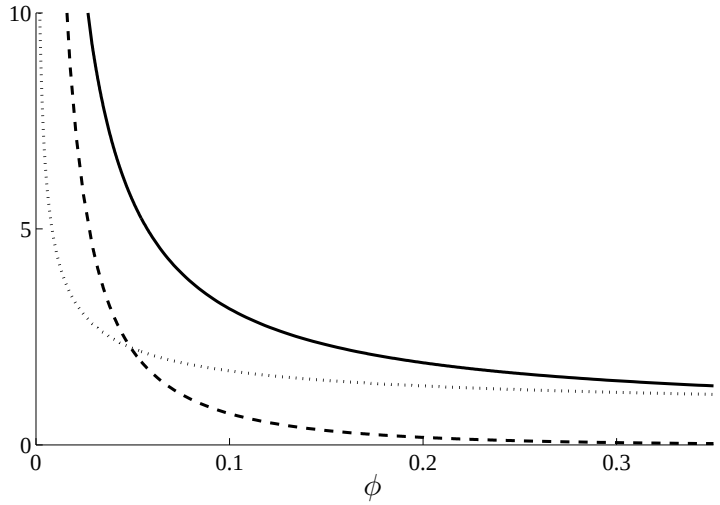

Figure D-2: $\langle s_{nc}\rangle_A/d$ (dotted line), $\langle {s_{nc}}^2\rangle_A/d^2$ (solid line), and $\langle s_n^2\rangle_A/d^2$ (dashed line) as predicted by Eqs. (D.18), (D.19), and (D.22) for the laboratory array (PVC sheets).

and

$$\frac{\langle {s_{nc}}^2\rangle_{s_{nc}>r^*}}{d^2} = \left(\frac{r^*}{d}\right)^2 + \frac{1-(8/\pi)\phi}{4\phi}. \tag{D.21}$$

The hole surface-to-surface spacing is related to the center-to-center spacing as $s_n = s_{nc} - d$. Then, by definition,

$$\frac{\langle {s_{nc}}^2\rangle_A}{d^2} = \frac{\langle {s_n}^2\rangle_A}{d^2} + 2\frac{\langle s_{nc}\rangle_A}{d} - 1, \tag{D.22}$$

and $\langle {s_n}^2\rangle_{s_{nc}>r^*}/d^2$ can be determined by applying Eqs. (D.20) and (D.21) to Eq. (D.22). For reference, Eqs. (D.20) and (D.21) are plotted in figure D-3 for $r^* = 2d$.

The probability that a cylinder in the random array has its nearest neighbor farther than $r = r^*$ is

$$P_{s_{nc}>r^*} \equiv P(\pi {r^*}^2 < a < \infty) = \int_{\pi {r^*}^2}^{\infty} f(a;\lambda)\ \mathrm{d}a = \frac{\mathrm{e}^{-\lambda\pi {r^*}^2}}{\mathrm{e}^{-\lambda A_L}}, \tag{D.23}$$

where $f(a;\lambda)$ is defined by Eq. (D.5). A_L is given by Eq. (D.17). Similarly, the probability that a cylinder has its nearest neighbor within $r = 5d$ is

$$P_{s_{nc}<5d} \equiv P(0 < a < \pi(5d)^2) = 1 - \frac{\mathrm{e}^{-25\lambda\pi d^2}}{\mathrm{e}^{-\lambda A_L}}. \tag{D.24}$$

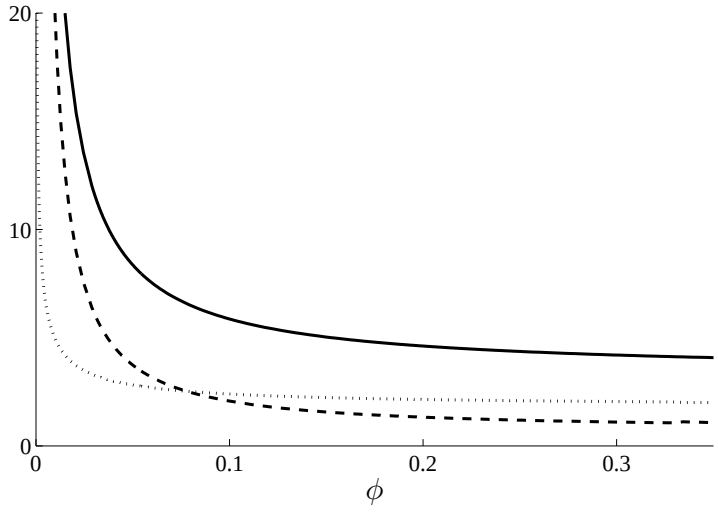

Figure D-3: $\langle s_{nc} \rangle_{s_{nc}>2d}/d$ (dotted line), $\langle {s_{nc}}^2 \rangle_{s_{nc}>2d}/d^2$ (solid line), and $\langle s_n^2 \rangle_{s_{nc}>2d}/d^2$ (dashed line) as predicted by Eqs. (D.20), (D.21) and (D.22). $r^* = 2d$.

For reference, Eq. (D.23) for $r^* = 2d$ and Eq. (D.24) are plotted in figure D-4.

D.2 Significance of hole generation order

Finally, note that the above formulation underpredicts the observed A_n at large ϕ, because it does not account for the overlapping of holes other than the reference hole (hole A in figure D-5). Consider the situation illustrated in figure D-5, where the random coordinates are generated in the order A, B, and C. Coordinate A is, by assumption, assigned as a hole center. The coordinate closest to A is coordinate C, which is at distance r_0 from A. It is the distribution of this distance that the theory Eq. (D.5) describes. However, coordinate B, which is at radial distance r_1 from the test hole center, is generated first. Because coordinates B and C are within d of each other, coordinate C would be discarded and the closest assigned hole center to A would be B, at distance r_1 ($\geq r_0$).

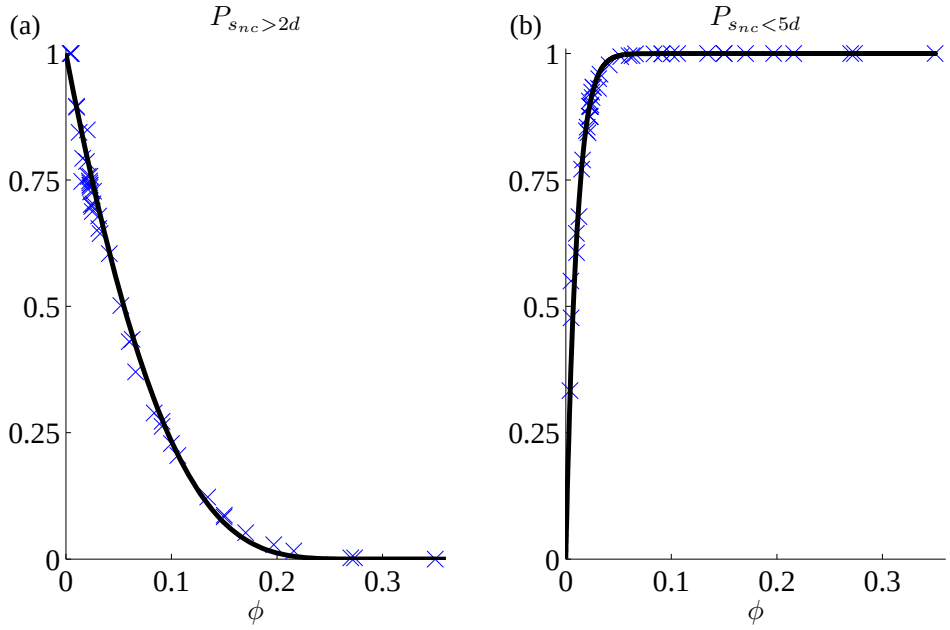

Figure D-4: (a) $P_{s_{nc}>2d}$ and (b) $P_{s_{nc}<5d}$ as predicted by Eqs. (D.23) and (D.24), respectively (solid lines). Each $\times$ represents the value that was obtained by counting the holes with nearest neighbors in the range (a) $\pi(2d)^2 < a < \infty$ and (b) $0 < a < \pi(5d)^2$ in four simulated 28 in $\times$ 15.75 in boards.

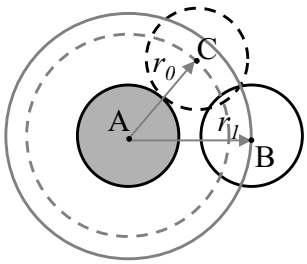

Figure D-5: Sketch of two random coordinates (B, C) generated near random coordinate A where a hole is already assigned (solid circle).

Appendix E

Permeability of random cylinder arrays[a]

The permeability, $k_\perp$, of sparse arrays can be described by Spielman and Goren (1968)'s analytical solution:

$$\frac{d^2}{k_\perp} = 8\phi \left[\frac{1}{4}\frac{d^2}{k_\perp} + \frac{d}{k_\perp^{1/2}} \frac{K_1\Big\{(d/2)k_\perp^{-1/2}\Big\}}{K_0\Big\{(d/2)k_\perp^{-1/2}\Big\}} \right], \tag{E.1}$$

where K_j is the modified Bessel function of order j of the second kind. Koch and Ladd (1997) show that Spielman and Goren (1968)'s solution accurately describes numerical simulation results at low ϕ, but rapidly deviates as ϕ increases beyond $\phi \approx 0.25$. Interestingly, $k_\perp \approx \langle s_n \rangle_A{}^2$, where $k_\perp$ is described by Eq. (E.1) and $\langle s_n \rangle_A$ is described by Eq. (D.10) (figure E-1). The difference between $(d/\langle s_n \rangle_A)^2$ and $d^2/k_\perp$ is less than 10% of $d^2/k_\perp$ in the range $\phi > 0.006$. Incidentally, Koch and Brady (1986)'s expression for $k_\perp$ is incorrect. Specifically, their expression does not agree with Spielman and Goren (1968)'s analytical solution, of which it is supposed to be an approximation. Moreover, it does not agree with numerical data presented by Koch and Ladd (1997, figure 21).

To the authors' knowledge, an analytical solution that describes $k_\perp$ in the range

[a]This chapter is Appendix B of Tanino and Nepf, 2008c, with minor modifications and two additional figures.

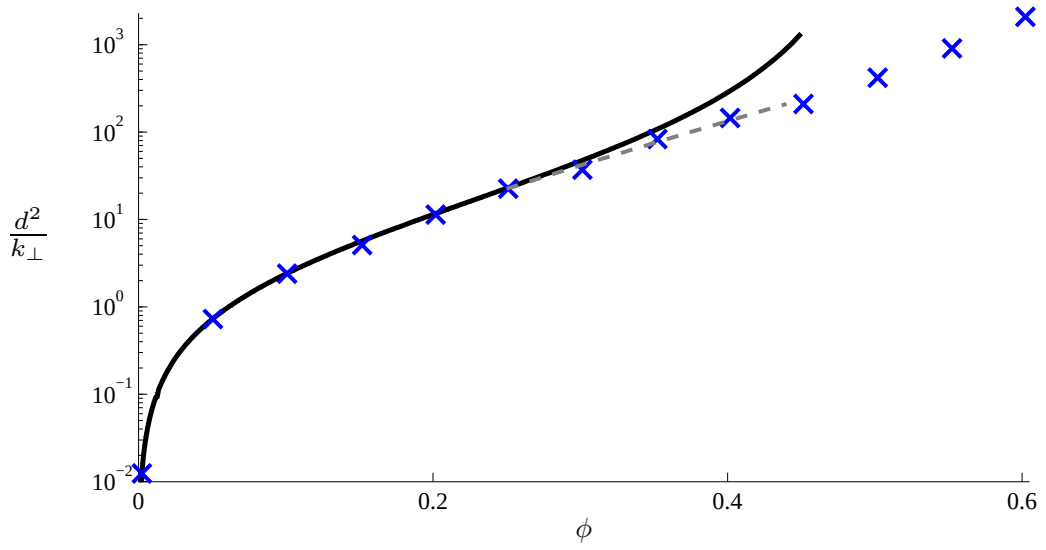

Figure E-1: $d^2/k_\perp$ [Eq. (3.21)]: Spielman and Goren (1968)'s analytical solution [Eq. (E.1); solid line] and numerical simulation results at $Re_d = 0$ extracted from Koch and Ladd, 1997, figure 21 ($\times$). $(d/\langle s_n \rangle_A)^2$ [Eq. (D.10); dotted line] is also plotted, but it cannot be distinguished from Eq. (E.1) at this resolution. Dashed line is Eq. (E.3).

$0.3 \leq \phi \leq 0.4$ has not been developed. Least-squares fitting a function of the form $\log_{10}\left\{\left\langle \overline{f_D} \right\rangle / (\mu \langle \overline{u} \rangle)\right\} = B_0 + B_1 \phi$ to numerical data in the range $\phi = 0.25 - 0.44$ in Koch and Ladd, 1997, figure 21 yields ($R = 0.99, n = 17$)

$$\frac{\left\langle \overline{f_D} \right\rangle}{\mu \langle \overline{u} \rangle} = 10^{0.94 \pm 0.04 + (3.2 \pm 0.1)\phi}. \tag{E.2}$$

The corresponding expression for $k_\perp$ is, from Eq. (3.21),

$$\frac{d^2}{k_\perp} = \frac{4\phi}{\pi(1-\phi)} 10^{0.94 \pm 0.04 + (3.2 \pm 0.1)\phi}. \tag{E.3}$$

Note that Eqs. (E.1) and (E.3) coincide at $\phi = 0.24$ ($d/\langle s_n \rangle_A = 4.4$). Following the above discussion, $k_\perp$ can be predicted from Eq. (E.1) for $d/\langle s_n \rangle_A \leq 4.4$ and from Eq. (E.3) for $d/\langle s_n \rangle_A > 4.4$.

Finally, recall from Appendix D.1 that our arrays are not exactly random. $k_\perp$ in our laboratory experiments are predicted from Eqs. (E.1) and (E.3) by matching

$d/\langle s_n \rangle_A$, i.e., ϕ in the two expressions is not the actual ϕ of our array, but ϕ of an exactly random array that has the same $d/\langle s_n \rangle_A$ (figure E-2).

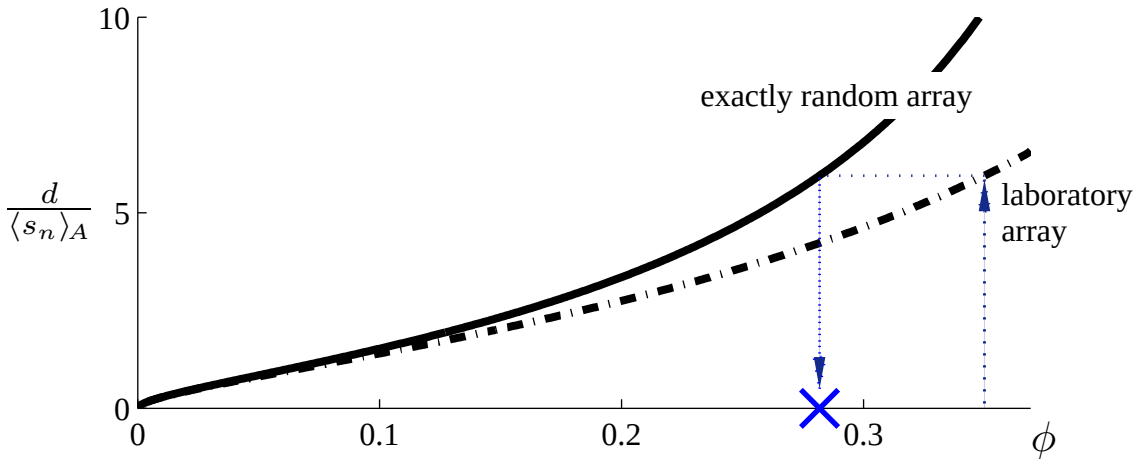

Figure E-2: $d/\langle s_n \rangle_A$ in the laboratory array constructed in PVC sheets (dash-dotted line) as predicted by Eq. (D.18) and for an exactly random array (solid line) as predicted by Eq. (D.10). An exactly random array with the same $d/\langle s_n \rangle_A$ as a $\phi = 0.35$ laboratory array has a $\phi = 0.28$ ($\times$).

Appendix F

Uncertainty of the gradient of a linear regression

The uncertainty in the gradient of a line of regression is estimated according to Taylor (1997, Ch. 8). Consider the line $y = B_0 + B_1 x$ that best fits n data points (x_k, y_k), $k = 1, 2, ..., n$ in the least-squares sense. The uncertainty in B_1 is defined as [Taylor, 1997, Eqs. (8.12), (8.15), (8.17)]

$$\sqrt{\frac{1}{n-2}\sum_{k=1}^{n}\left[y_k - (B_0 + B_1 x_k)\right]^2}\sqrt{\frac{n}{n\sum_{k=1}^{n} x_k^2 - \left(\sum_{k=1}^{n} x_k\right)^2}}. \tag{F.1}$$

For example, consider the mean turbulence intensity, $\langle\sqrt{k_t}/U_p\rangle$, and the normalized asymptotic dispersion coefficient, $K_{yy}/(\langle\overline{u}\rangle d)$, at each ϕ, which are calculated as the gradient of the line of regression of $\sqrt{k_t}$ on U_p and of σ_y^2 on x normalized by $2d$, respectively. The uncertainty in $\left\langle\sqrt{k_t}/U_p\right\rangle$ and $\mathrm{d}\sigma_y^2/\mathrm{d}x$ are calculated as Eq. (F.1). The uncertainty in $K_{yy}/(\langle\overline{u}\rangle d)$ is simply the uncertainty in $\mathrm{d}\sigma_y^2/\mathrm{d}x$ divided by $2d$.

Appendix G

Cylinder drag: additional comments

In this appendix, two topics related to cylinder drag are discussed. In § G.1, $\left\langle \overline{f_D} \right\rangle$ in periodic arrays are compared with $\left\langle \overline{f_D} \right\rangle$ in random arrays. In § G.2, the maximum Re_d at which the vertical position of the interface between the two layers of a lock-exchange flow varies linearly with streamwise distance is predicted from $\left\langle \overline{f_D} \right\rangle$. The predictions are compared with the empirical criterion proposed by Tanino et al. (2005).

G.1 Comparison with a periodic cylinder array

In figure G-1, $\left\langle \overline{f_D} \right\rangle / (\mu \langle \overline{u} \rangle)$ in square arrays (Koch and Ladd, 1997) are compared with $\left\langle \overline{f_D} \right\rangle / (\mu \langle \overline{u} \rangle)$ in random arrays. Because $\left\langle \overline{f_D} \right\rangle / (\mu \langle \overline{u} \rangle)$ varies with array orientation, only the maximum and minimum $\left\langle \overline{f_D} \right\rangle / (\mu \langle \overline{u} \rangle)$ are represented here for the two $\phi = 0.2$ and 0.4 that Koch and Ladd (1997) considered. $\left\langle \overline{f_D} \right\rangle / (\mu \langle \overline{u} \rangle)$ at a given Re_d is smaller in a square array than in a random array for all orientations, and highlights the sensitivity of drag, and presumably turbulence intensity [cf. Eq. (3.14)], to the exact configuration of the cylinders. The sensitivity of these properties imply that researchers who use real plants in flume experiments should reproduce the configuration of the plants, if their intent is to create experimental flow conditions that resemble those in the field.

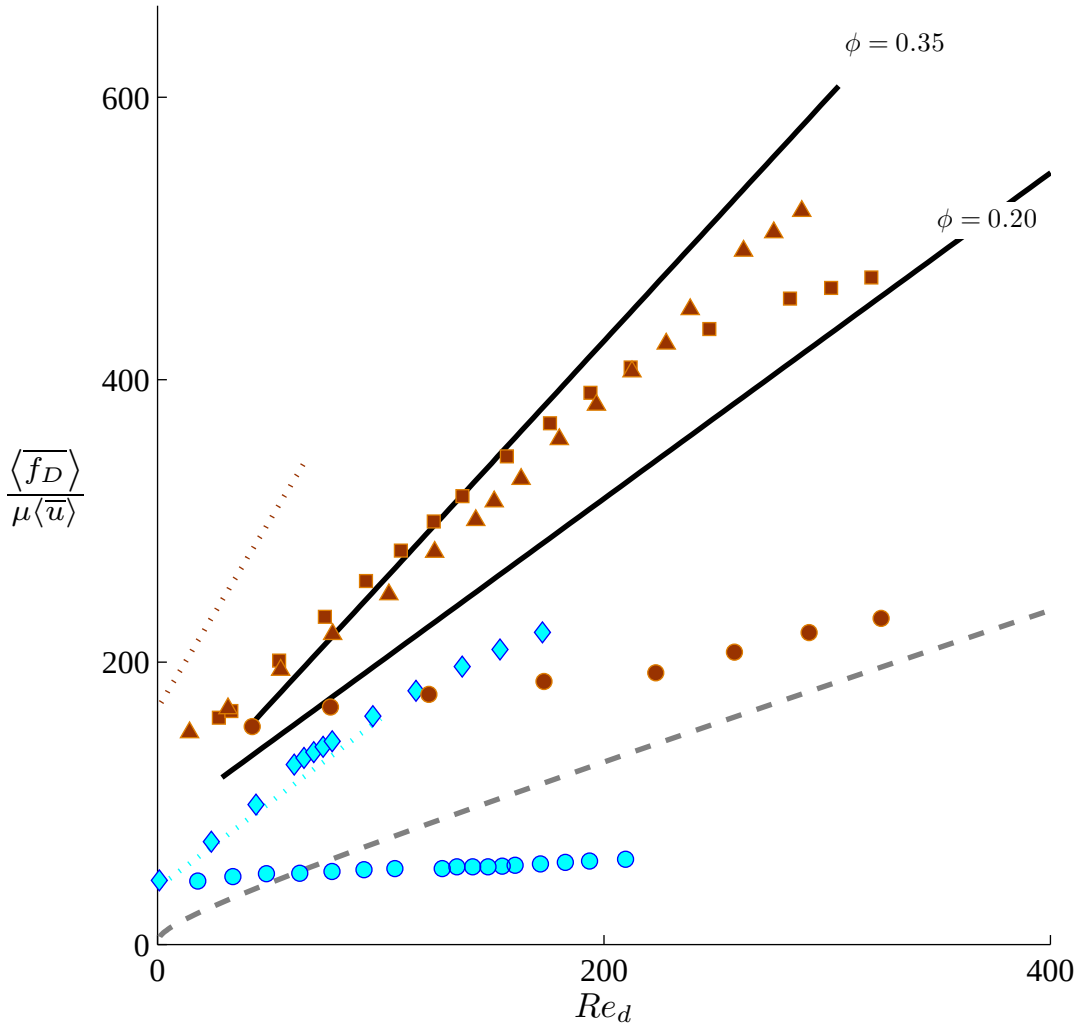

Figure G-1: Selected $\left\langle \overline{f_D} \right\rangle / (\mu \langle \overline{u} \rangle)$ in the form of Eq. (2.6), with fitted coefficients based on laboratory experiments in Ch. 2 (solid line) and Koch and Ladd (1997)'s numerical simulations at $\phi = 0.2$ (cyan dotted) and 0.4 (brown dotted) in random arrays (cf. Table 2.2). The isolated cylinder solution [Eq. (2.9)] is also included (dashed). $\left\langle \overline{f_D} \right\rangle / (\mu \langle \overline{u} \rangle)$ for a square array was extracted from Koch and Ladd (1997, figures 11, 16) for $\phi = 0.2$ (solid cyan) and $\phi = 0.4$ (solid brown); different markers denote different orientations of the drag relative to the principle axes of the array.

G.2 Criterion for the liner-interface regime of a lock-exchange flow

The similarity solution for lock-exchange flows propagating through cylinder arrays, for which (i) the Navier-Stokes equation in the streamwise direction [Eq. (2.2)] can be reduced to a balance between the pressure gradient and drag only and (ii) $\left\langle \overline{f_D} \right\rangle / (\mu \langle \overline{u} \rangle)$ is independent of Re_d, predicts that the depth of the interface between the two fluid layers varies linearly with streamwise distance (Tanino et al., 2005). Note that this second condition is equivalent to the drag coefficient

$$C_D \equiv \frac{\left\langle \overline{f_D} \right\rangle}{\mu \langle \overline{u} \rangle} \frac{2}{Re_d} \tag{G.1}$$

being inversely proportional to $|\langle \overline{u} \rangle|$. Tanino et al. (2005) observed a linear interface in lock-exchange flows propagating at $Re_{d,toe}$ of up to 60, where $Re_{d,toe}$ is the Reynolds number based on the speed of the toe of the interface. Then, it follows from condition (ii) above that $\left\langle \overline{f_D} \right\rangle / (\mu \langle \overline{u} \rangle)$ remains independent of Re_d up to $Re_d \approx 60$.

Where $\left\langle \overline{f_D} \right\rangle / (\mu \langle \overline{u} \rangle)$ takes on the form given by Eq. (2.6),

$$\frac{\left\langle \overline{f_D} \right\rangle}{\mu \left\langle \overline{u} \right\rangle} = \alpha_0(\phi) + \alpha_1(\phi) Re_d, \tag{G.2}$$

a Re_d-independent $\left\langle \overline{f_D} \right\rangle / (\mu \langle \overline{u} \rangle)$ requires

$$Re_d \ll \frac{\alpha_0}{\alpha_1}. \tag{G.3}$$

Koch and Ladd (1997)'s numerical simulations and present laboratory experiments reported in Ch. 2 yield $\alpha_0/\alpha_1 = O(10 - 80)$ (Table 2.2), and Eq. (G.3) predicts a threshold one order of magnitude smaller than the $Re_d \approx 60$ threshold identified by Tanino et al. (2005). The disagreement may be attributed to two factors. First, cylinders were not randomly-distributed in the lock-exchange experiments. Koch and Ladd (1997)'s simulations suggest that α_0/α_1 is larger in a square array than in a

random array[a] (figure G-1), which in turn suggests that deviations from a random distribution tends to increase the maximum Re_d for which Eq. (G.3) is satisfied. Second, the criterion $Re_{d,toe} = 60$ itself is expected to be an overestimate of the threshold of the linear interface regime. This is because $Re_{d,toe}$ is defined at the toe of the propagating front, where the front speed is highest, but even interfaces that were classified as linear deviated from a linear profile close to the toe (Tanino et al., 2005).

From the evolution of lock-exchange flows exhibiting a linear interface ($0.034 < \phi < 0.062$, $Re_{d,toe} < 52$), Tanino et al. (2005) estimated that $C_D \approx 2\alpha_0/Re_d = (310 \pm 90)/Re_d$. It is noted that the corresponding $\alpha_0 = 160 \pm 50$ is one order of magnitude larger than α_0 estimated directly from drag measurements (figure 2-5). In Koch and Ladd (1997)'s simulations, α_0 in square arrays are comparable to that in random arrays (figure G-1), which suggests that differences in cylinder configuration between Tanino et al., 2005 and the present experiments do not account for the disagreement. The reason for the disagreement remains an open question.

[a] α_0/α_1 for a square array were obtained from Koch and Ladd (1997)'s simulations by performing a linear regression over $0 < Re_d < 62$ and $0 < Re_d < 180$ for $\phi = 0.2$ and 0.4, respectively. It is noted that $\langle\overline{f_D}\rangle/(\mu\langle\overline{u}\rangle)$ is not exactly proportional to Re_d in square arrays (Koch and Ladd, 1997). Nevertheless, the linear regressions yield a significant correlation, indicating that over the range of Re_d considered, $\langle\overline{f_D}\rangle/(\mu\langle\overline{u}\rangle)$ can be approximated as increasing linearly with Re_d. Estimated α_0/α_1 for $\phi = 0.2$ and 0.4 varies with the array orientation over the range $31 - 270$ and $87 - 450$, respectively, in Koch and Ladd (1997)'s simulations.

Appendix H

Lateral dispersion at transitional Reynolds number: intermediate cylinder densities ($\phi < 0.19$)

In Ch. 4, we considered lateral dispersion at transitional Re_d, i.e., below fully turbulent conditions, in dense arrays, for which our theory predicts that turbulent diffusion makes a negligible (specifically, $< 10\%$) contribution to the asymptotic macroscopic dispersion coefficient K_{yy} (figure 3-15). In this appendix, we consider arrays of intermediate ϕ, for which our model predicts that both turbulent diffusion and dispersion associated with the time-averaged, spatially-heterogeneous velocity field contribute significantly to K_{yy} in fully turbulent flow. As discussed in § 4.1, our model predicts that this regime extends up to $\phi \approx 0.19$. Also, this intermediate regime only extends down to a certain ϕ, below which the flow resembles an open-channel flow and the spatial heterogeneity in the velocity field no longer contributes significantly to $K_{yy}/(\langle\overline{u}\rangle d)$. Our model predicts that this contribution is less than 10% at $\phi < 0.035$ [Eq. (3.23)] or at $\phi < 0.0025$ [Eq. (3.24)], depending on the model used to describe the contribution from the time-averaged velocity field. The exact ϕ at which the lower limit of this intermediate ϕ regime occurs is not relevant to the present discussion.

The Re_d dependence of $K_{yy}/(\langle\overline{u}\rangle d)$ in this intermediate ϕ regime is expected to be complex. First, the time-averaged velocity field, and therefore its contribution to

asymptotic dispersion, is expected to depend strongly on Re_d. For example, Hill et al. (2001) report that the spatial variance of the transverse components of velocity normalized by $\langle\overline{u}\rangle^2$ decreased by 63% between Stokes flow and steady flow at $Re_d = 59.5$ in their numerical simulations of an array of randomly-distributed spheres $\phi = 0.0960$. However, to our knowledge, the Re_d dependence of the time-averaged velocity field in unsteady laminar and turbulent flow has not been examined systematically, and it is unclear how its contribution to $K_{yy}/(\langle\overline{u}\rangle d)$ changes with Re_d. This investigation is beyond the scope of this project. Second, at intermediate ϕ, the interstitial pores may be sufficiently large for cylinder wakes to exhibit an unsteady laminar regime and oscillate periodically like isolated cylinder wakes. It seems likely that such periodic oscillations will enhance both pore-scale mixing and macroscopic lateral dispersion of the time-averaged solute concentration field. To our knowledge, the contribution of the periodic motion of wakes to net dispersion has not been described in the literature. Nevertheless, the effect is likely to be complex, since the amplitude and frequency of the periodic motion presumably varies gradually as Re_d is increased across the unsteady laminar regime as in an isolated cylinder wake. Finally, as stated above, the contribution from the time-averaged velocity field, whose Re_d dependence is not obvious, remains significant even after the onset of turbulence. Based on the observed reduction in the normalized spatial variance of the transverse velocity components as mentioned above, Hill et al. (2001) conjecture that transverse dispersion, expressed in the form of $K_{yy}/(\langle\overline{u}\rangle d)$, will decrease as Re_d increases beyond Stokes flow. The same qualitative trend is expected in random cylinder arrays. However, how dispersion varies as Re_d is increased beyond steady laminar flow is not obvious.

Below, LIF measurements of the time-averaged lateral concentration distribution of solute released continuously from a point source in $\phi = 0.091$ and 0.15 are discussed. For the experimental procedure, refer to § 3.3. ${\sigma_y}^2$ and C_{ms} were computed as Eqs. (4.1) - (4.3).

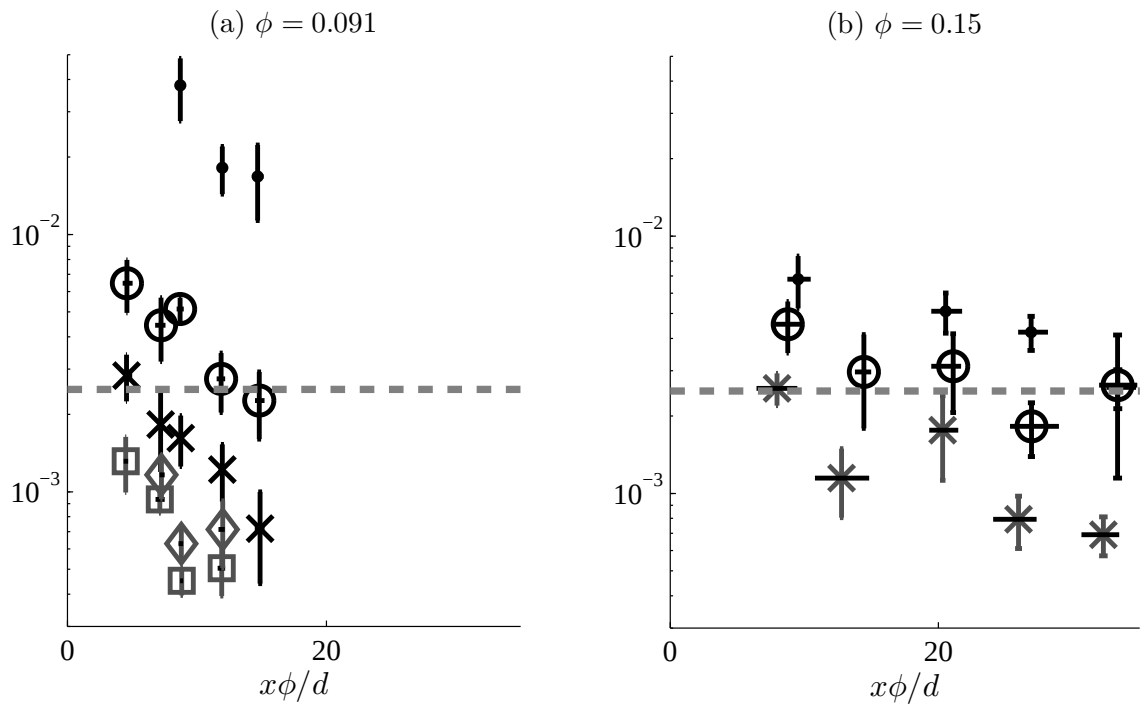

Figure H-1: $\langle C_{ms} \rangle$ [cm^{-1}] at (a) $\phi = 0.091$, $Re_d = 37-40$ ($\cdot$), $55-59$ ($\circ$), $82-85$ ($\times$), $300-320$ (square), and $430-480$ ($\diamond$) and at (b) $\phi = 0.15$, $Re_d = 75-79$ ($\cdot$), $110-120$ ($\circ$), and $190-210$ ($\times$). Each of these markers represents an average of four or more runs; horizontal bars indicate the range in x and vertical bars indicate the standard error of the mean. Markers in grey denote $Re_{\langle s_n \rangle_A} > 74$, which corresponds to $Re_d > 96$ and > 150 for $\phi = 0.091$ and 0.15, respectively. $\langle C_{ms} \rangle = 2.5 \times 10^{-3}$ cm^{-1} (dashed) is the empirical boundary proposed in Ch. 4 to segregate time-averaged concentration profiles of plumes undergoing asymptotic dispersion from those that are in the pre-asymptotic regime.

H.1 Deviation of the time-averaged concentration distribution from a Gaussian distribution

At each ϕ, $\langle C_{ms} \rangle$ exhibits the same two trends identified in § 4.3.2 for $\phi = 0.20$ and 0.35 (figure H-1). First, $\langle C_{ms} \rangle$ decreases as x increases at each Re_d. Second, $\langle C_{ms} \rangle$ decreases as Re_d increases for all x considered. However, note that the second trend only holds for moderate Re_d ($\leq 82-85$) at $\phi = 0.091$: $\langle C_{ms} \rangle$ at $Re_d = 300-320$ (square) and $430-480$ ($\diamond$) are constant within standard error of the measurements. This is consistent with $\langle \sigma_y^2 \rangle$ being strongly Re_d-dependent at $Re_d < 100$ and being

approximately constant at $Re_d > 200$ (Appendix A). The Re_d independence of both $\langle\sigma_y^2\rangle$ and $\langle C_{ms}\rangle$ in the high Re_d regime suggest that the concentration distribution itself is Re_d-independent in that regime.

Recall that a sharp reduction in $\langle C_{ms}\rangle$ was observed at $\phi = 0.20$ and 0.35 at a Re_d that coincided with the transition from steady to unsteady laminar flow (§ 4.3.2). A similar sharp reduction is observed at $\phi = 0.091$ between $Re_d = 37 - 40$ ($\cdot$) and $55 - 59$ ($\circ$), which suggests that the transition from steady laminar to unsteady flow occurs between the two Re_d, i.e., $40 < Re_d < 55$, at $\phi = 0.091$. At $\phi = 0.15$, the onset of unsteadiness occurs below $Re_d \leq 70$ (figure 3-5) and, accordingly, $\langle C_{ms}\rangle$ does not dramatically change within the range of Re_d (≥ 77) considered for $\phi = 0.15$ [figure H-1(b)].

Figure H-1 suggests that at similar $x\phi/d$ and Re_d, $\langle C_{ms}\rangle$ is larger at $\phi = 0.15$ than 0.091. Recall that the same trend was observed between $\phi = 0.20$ and 0.35 (figure 4-4). In fully turbulent flow, this trend is anticipated by the scaling Eq. (4.5).

H.2 Variance of the time-averaged concentration profile

Measurements of the ensemble-averaged variance of time-averaged lateral concentration profiles $\left(\langle\sigma_y^2\rangle\right)$ are presented in figures H-2 and H-3 for $\phi = 0.091$ and 0.15, respectively. A subset of measurements at high Re_d reported in Ch. 3 are also included. Also presented are least-squares fit to $\langle\sigma_y^2(x)\rangle$ measurements that are classified as being in the asymptotic (large x) dispersion regime by the empirical criterion $\langle C_{ms}\rangle = 2.5 \times 10^{-3}$ cm^{-1} that was proposed in Ch. 4.

The Re_d dependence of $\langle\sigma_y^2(x)\rangle$ is qualitatively similar to other ϕ (Appendix A): $\langle\sigma_y^2(x)\rangle$ at a given x decreases as Re_d decreases below $Re_d = 82 - 85$ at $\phi = 0.091$ and below $Re_d = 190 - 210$ at $\phi = 0.15$, and remains approximately constant from $Re_d = 300 - 320$ to $430 - 480$ at $\phi = 0.091$. Not enough data are available at high Re_d to confirm the Re_d-independent $\langle\sigma_y^2(x)\rangle$ regime for $\phi = 0.15$. Note that the

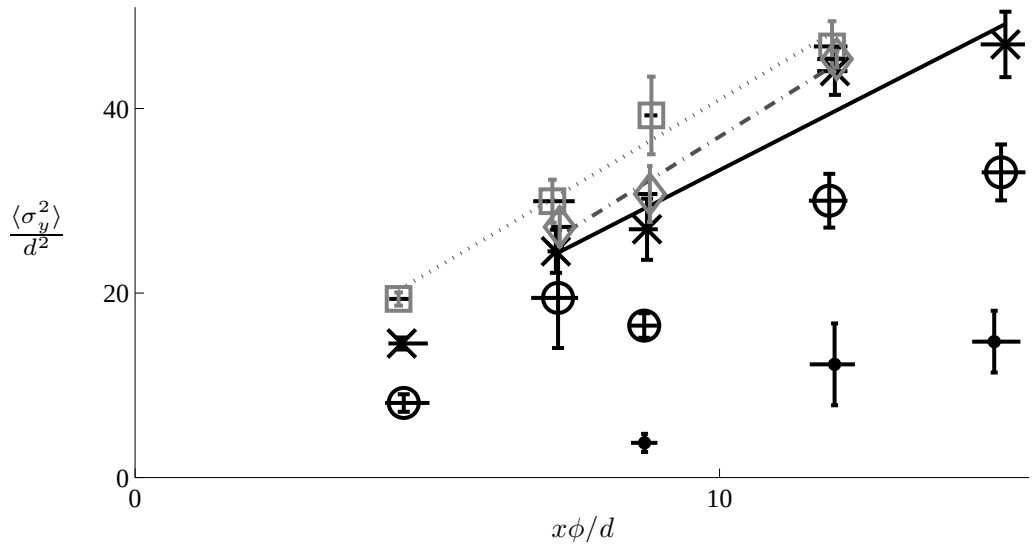

Figure H-2: Evolution of the ensemble-averaged variance with streamwise distance at $Re_d = 37 - 40$ ($\bullet$), 55 - 59 ($\circ$), 82 - 85 ($\times$), 300 - 320 (square), and 430 - 480 ($\diamond$) at $\phi = 0.091$. Each marker represents an average of four or more runs; horizontal bars indicate the range in x and vertical bars indicate the standard error of the mean. Grey markers denote $Re_{\langle s_n\rangle_A} > 74$. Solid line is the least-squares fit to $\langle\sigma_y^2\rangle$ for $Re_d = 82 - 85$, $x\phi/d > 7$: $\mathrm{d}\langle\sigma_y^2\rangle/\mathrm{d}x = 0.19 \pm 0.04$ cm ($R^2 = 0.93, n = 4$). Dotted line is the least-squares fit to $\langle\sigma_y^2\rangle$ for $Re_d = 300 - 320$: $\mathrm{d}\langle\sigma_y^2\rangle/\mathrm{d}x = 0.22 \pm 0.02$ cm ($R^2 = 0.98, n = 4$). Dash-dotted line is the least-squares fit to $\langle\sigma_y^2\rangle$ for $Re_d = 430 - 480$: $\mathrm{d}\langle\sigma_y^2\rangle/\mathrm{d}x = 0.23 \pm 0.03$ cm ($R^2 = 0.98, n = 3$).

observed Re_d dependence is consistent with the proposed threshold, $Re_{\langle s_n\rangle_A} > 74$, for the Re_d-independent $\langle\sigma_y^2(x)\rangle$ regime (Appendix A).

At $\phi = 0.091$, the asymptotic $\mathrm{d}\langle\sigma_y^2\rangle/\mathrm{d}x$, hence $K_{yy}/(\langle\overline{u}\rangle d)$, is equal within uncertainty for $Re_{\langle s_n\rangle_A} > 74$, i.e., at $Re_d = 300 - 320$ (dotted) and $430 - 480$ (dash-dotted). Asymptotic $\mathrm{d}\langle\sigma_y^2\rangle/\mathrm{d}x$ at $Re_d = 82 - 85$ (solid line), which is below this threshold, also agrees within uncertainty with the $Re_{\langle s_n\rangle_A} > 74$ limit. $\langle C_{ms}\rangle$ values suggest that dispersion remained pre-asymptotic over the range of x that were considered at all other Re_d at $\phi = 0.091$ and at all Re_d except $Re_d = 190 - 210$ at $\phi = 0.15$. Additional measurements at larger x are necessary to quantify asymptotic $\mathrm{d}\langle\sigma_y^2\rangle/\mathrm{d}x$, and to examine its dependence on Re_d, at transitional flow regimes.

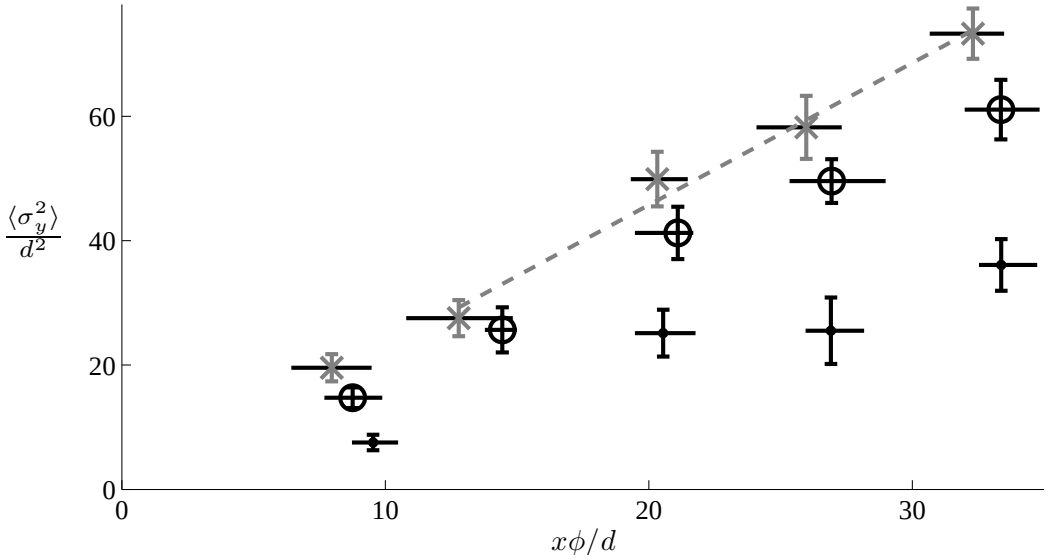

Figure H-3: Evolution of the ensemble-averaged variance with streamwise distance at $Re_d = 75 - 79$ ($\bullet$), 110 - 120 ($\circ$), and $190 - 210$ ($\times$) at $\phi = 0.15$. Each marker represents an average of four or more runs; horizontal bars indicate the range in x and vertical bars indicate the standard error of the mean. Grey markers denote $Re_{\langle s_n\rangle_A} > 74$. Dashed line is the least-squares fit to $\langle\sigma_y^2\rangle$ for $Re_d = 190 - 210$: $\mathrm{d}\langle\sigma_y^2\rangle/\mathrm{d}x = 0.22 \pm 0.02$ cm ($R^2 = 0.99, n = 4$).

Appendix I

Spatial variance of the time-averaged velocity field

In this appendix, we consider the dependence of $\langle \overline{u}''^2 \rangle / \langle \overline{u} \rangle^2$ on ϕ and Re_d. The procedure for computing this value from the velocity time records is described in § 3.3.1.

Figure I-1 presents laboratory measurements of $\langle \overline{u}''^2 \rangle / \langle \overline{u} \rangle^2$ as a function of Re_d. Also presented are $\langle \overline{u}''^2 \rangle / \langle \overline{u} \rangle^2$ estimated from lateral transects of $\overline{u}$ provided by White (2002, personal comm.).[a] As Re_d is increased at $\phi = 0.010, 0.091, 0.20$, and 0.35, $\langle \overline{u}''^2 \rangle / \langle \overline{u} \rangle^2$ decreases rapidly at low Re_d and is constant within experimental uncertainty at $Re_d > 200$. At other ϕ, variations across Re_d fluctuate and salient trends cannot be identified.

There is substantial disagreement between measurements by White (2002), which were collected using ADV, and the present data, with the former generally being smaller than the latter. The disagreement is largest at the largest ϕ ($= 0.063, \diamond$) for which a comparison can be made. A possible explanation for the disagreement is sampling bias in the ADV measurements. Because ADV probes, which must be submerged in water, have a substantial horizontal footprint, it is likely that White (2002) selected the sampling locations to avoid regions of high local cylinder density

[a] It is noted that the ordinate axis of White and Nepf, 2003, figure 6 is incorrectly labeled as σ_u^{*2}, where it should be σ_u^*.

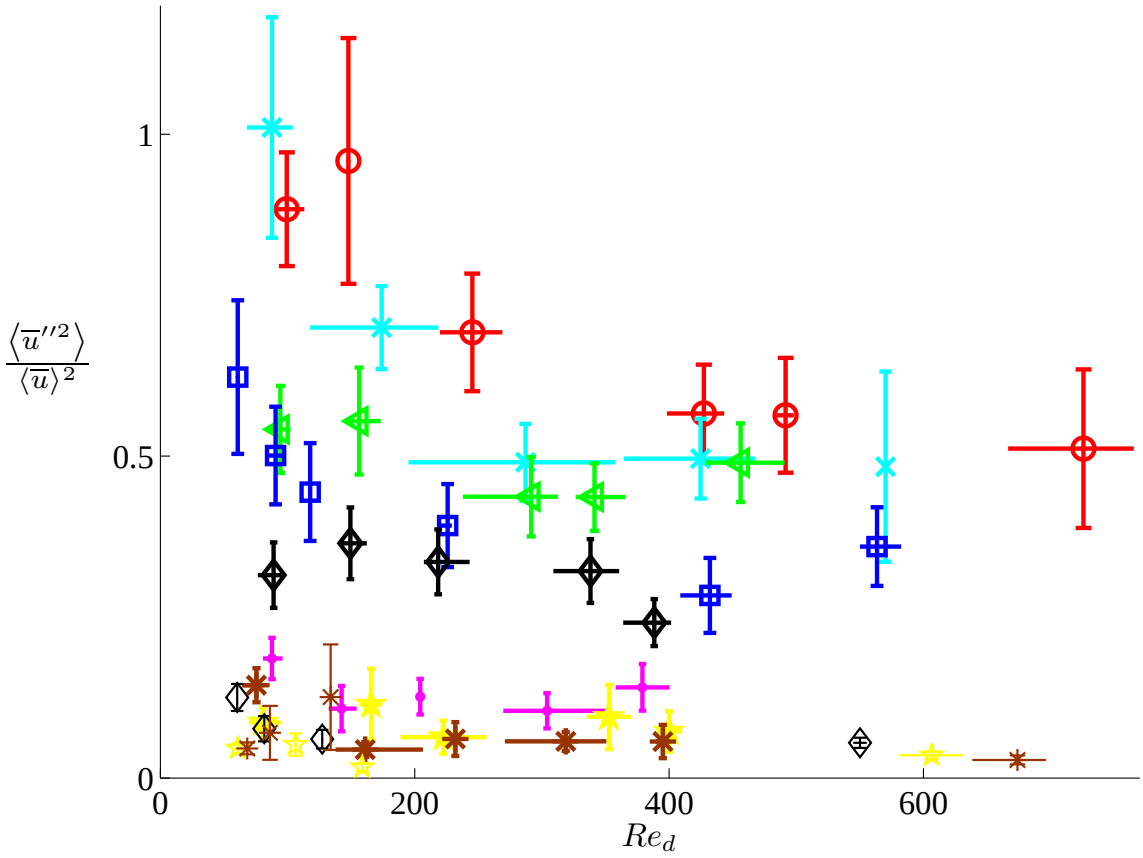

Figure I-1: The normalized spatial variance of the time-averaged velocity, $\langle \overline{u}''^2 \rangle / \langle \overline{u} \rangle^2$, estimated from LDV measurements at $\phi = 0.010$ ($*$), 0.020 ($\star$), 0.031 ($\cdot$), 0.060 ($\diamond$), 0.091 (square), 0.15 ($\triangleleft$), 0.20 ($\times$), 0.35 ($\circ$); $\langle \overline{u} \rangle$ was approximated by its cross-sectional average. Values for high Re_d were obtained from velocity records analyzed in § 3.4.2. Also plotted are values estimated from lateral transects of $\overline{u}$ provided by B. L. White (personal comm.) at $\phi = 0.010$ (thin $*$), 0.020 (thin $\star$), 0.063 (thin $\diamond$); Re_d for these data were computed by assuming $\nu = 0.01$ cm^2 s^{-1} and approximating $\langle \overline{u} \rangle$ by the mean of the $\overline{u}$ measured along a given lateral transect. Vertical bars represent the standard error of the mean. Horizontal bars reflect the range in Re_d [or in $\langle \overline{u} \rangle$ for White (2002)'s data] across all time records that contributed to that data point.

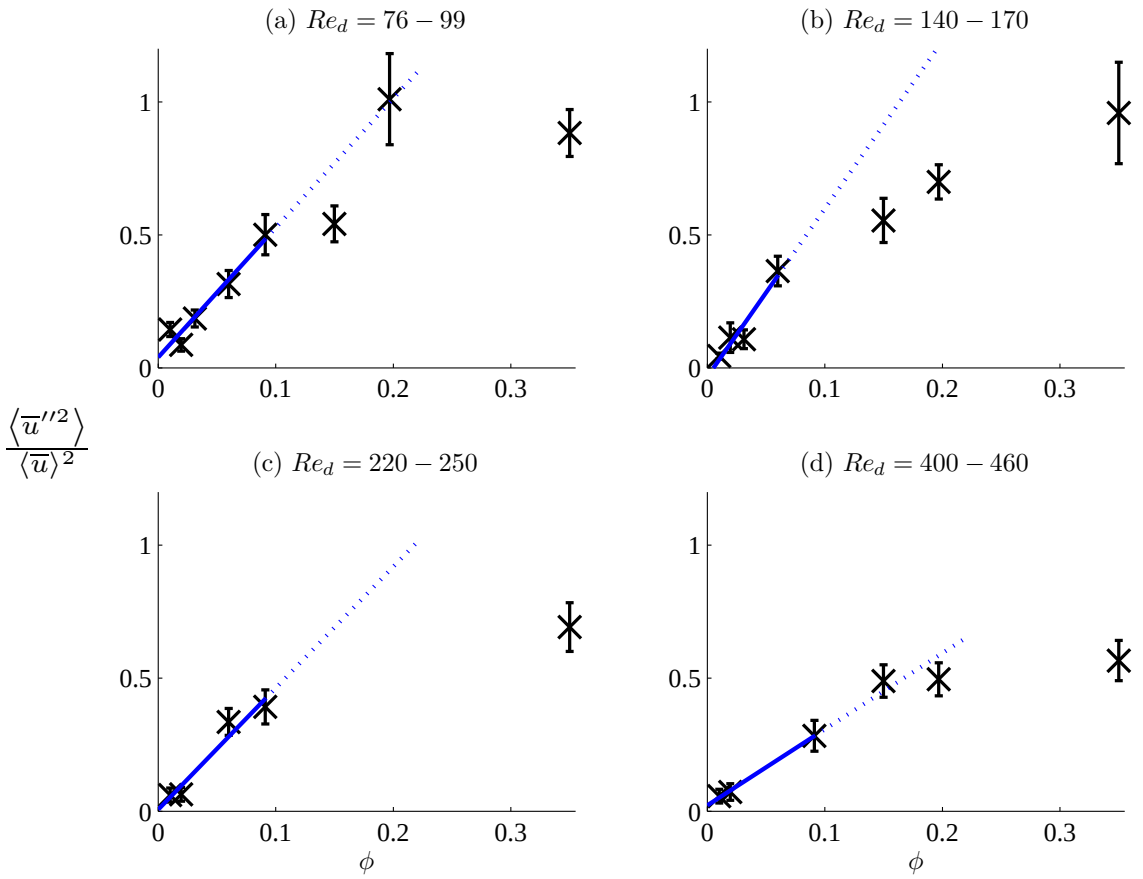

Figure I-2: The ϕ dependence of $\langle \overline{u}''^2 \rangle / \langle \overline{u} \rangle^2$. Vertical bars indicate the standard error of the mean. The range in Re_d for each subplot represents the range over all time records that are represented in that plot; it is not an indication of the experimental uncertainty in Re_d. The solid line in each subplot is the least-squares fit to data at $\phi < 0.1$; $R =$ (a) 0.97 ($n = 5$); (b) 0.96 ($n = 4$); (c) 0.97 ($n = 4$); (d) 1.0 ($n = 3$). The axes are identical in each subplot.

for the high $\phi = 0.063$ measurements. Since spatial variations in the velocity are due to the presence of the cylinders, this would have resulted in an underestimation of $\langle \overline{u}''^2 \rangle / \langle \overline{u} \rangle^2$.

In figure I-2, $\langle \overline{u}''^2 \rangle / \langle \overline{u} \rangle^2$ at selected Re_d are plotted against ϕ. Recall that α_1 can be described by a single linear function of ϕ over the entire range of ϕ considered, namely $0.091 \leq \phi \leq 0.35$ [Eq. (2.15)]. Dimensional analysis [Eq. (2.5)] then suggests that $\langle \overline{u}''^2 \rangle / \langle \overline{u} \rangle^2 \propto \phi$. LDV measurements of $\langle \overline{u}''^2 \rangle / \langle \overline{u} \rangle^2$ exhibit a linear dependence on ϕ at small ϕ (< 0.1) (figure I-2, solid line). However, $\langle \overline{u}''^2 \rangle / \langle \overline{u} \rangle^2$ increases more slowly with ϕ at larger ϕ (> 0.1). It is not clear from figure I-2 if $\langle \overline{u}''^2 \rangle / \langle \overline{u} \rangle^2$ (i)

increases linearly with ϕ at $\phi > 0.1$, but with a smaller gradient than at $\phi < 0.1$, or (ii) adopts a weaker, non-linear dependence on ϕ. The latter is inconsistent with Eq. (2.15), and would imply that Eq. (2.5) is incorrect. The former is consistent with the linear ϕ dependence exhibited by α_1. However, it also implies that α_1 depends linearly on ϕ with a larger gradient at $\phi < 0.1$ than at $\phi > 0.1$. While laboratory measurements were not collected at $\phi < 0.1$, an inspection of drag measurements in the literature suggests that a single linear function of ϕ, namely Eq. (2.15), applies to all $0 < \phi \leq 0.35$ [figure 2-4(a)], suggesting that Eq. (2.5) is incomplete or is only valid at limited ϕ.

Previously, White and Nepf (2003) proposed that

$$\frac{\langle \overline{u}''^2 \rangle}{\langle \overline{u} \rangle^2} \sim C_D^{3/2} \sqrt{\phi} \tag{I.1}$$

in sparse arrays, where $\phi < 0.1, C_D\phi \ll \pi/8$. They show that measured $\langle \overline{u}''^2 \rangle / \langle \overline{u} \rangle^2$ at $\phi = 0.063, 60 \leq Re_d \leq 550$ decrease with Re_d, which is consistent with the Re_d dependence of C_D. However, they did not compare their measurements quantitatively, perhaps because values for C_D in random arrays had not been experimentally confirmed in the literature. Following Ch. 2, $C_D(\phi, Re_d)$ can now be predicted by Eq. (2.7), with coefficients α_0 and α_1 as measured in the present experiments (Table 2.2; $0.091 \leq \phi \leq 0.35$). For smaller ϕ (< 0.091), for which measurements could not be collected due to experimental constraints, α_0 and α_1 can be predicted by Eqs. (2.16) and (2.15), respectively.

$\langle \overline{u}''^2 \rangle / \langle \overline{u} \rangle^2$ estimated from velocity time records collected in the present study agree with this proposed dependence at small ϕ (≤ 0.091) (figure I-3). In contrast, the dependence of White (2002)'s measurements on $C_D^{3/2}\sqrt{\phi}$ is unclear, because most of the data fall within a small range of $0.1 < C_D^{3/2}\sqrt{\phi} < 0.2$.

Although Eq. (I.1) was derived for $\phi < 0.1$, the Re_d dependence of $\langle \overline{u}''^2 \rangle / \langle \overline{u} \rangle^2$ at a given ϕ at all Re_d considered at $\phi = 0.20$ ($\times$) and at $Re_d > 150$ at $\phi = 0.35$ ($\circ$) is still accurately described by $C_D^{3/2}$, but with a different scaling constant than at

$0.020 \leq \phi \leq 0.091$:

$$\frac{\langle \overline{u}''^2 \rangle}{\langle \overline{u} \rangle^2} \propto C_D^{3/2} \sqrt{\phi} \begin{cases} (0.60 \pm 0.04), & 0.020 \leq \phi \leq 0.091 \\ (0.28 \pm 0.02), & \phi = 0.20 \\ (0.27 \pm 0.02), & \phi = 0.35 \end{cases} . \tag{I.2}$$

However, $\langle \overline{u}''^2 \rangle / \langle \overline{u} \rangle^2$ at $\phi = 0.20$ and 0.35 are similar in magnitude at different $C_D^{3/2}\sqrt{\phi}$, which indicates that the ϕ dependence is no longer captured exactly by $C_D^{3/2}\sqrt{\phi}$ at large ϕ (≥ 0.20).

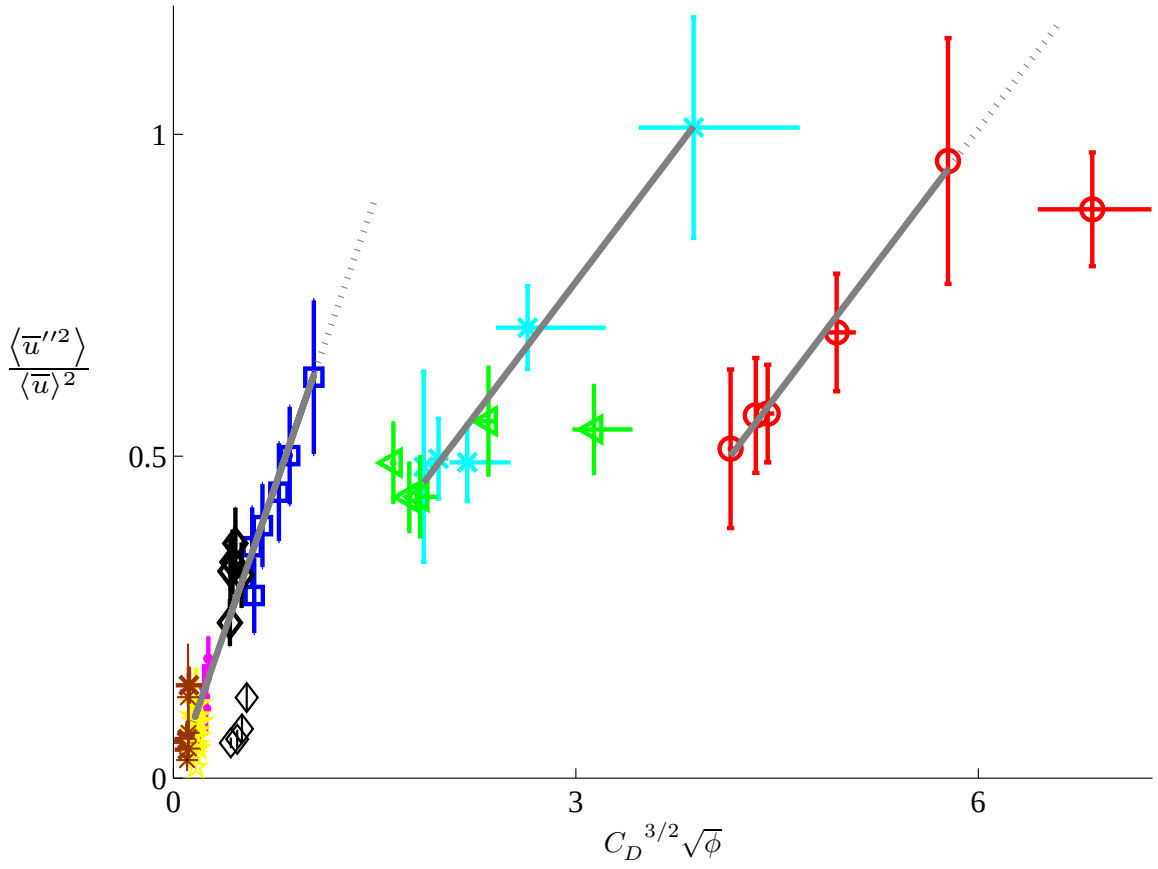

Figure I-3: Comparison of the spatial variance of the time-averaged velocity with the ϕ and Re_d dependence proposed by White and Nepf (2003): $\langle \overline{u}''^2 \rangle / \langle \overline{u} \rangle^2 \sim C_D{}^{3/2}\sqrt{\phi}$. $C_D(\phi, Re_d)$ is given by Eq. (2.7), with coefficients α_0 and α_1 as determined from the present experiments (Table 2.2) for $\phi \geq 0.091$ and as predicted by Eqs. (2.16) and (2.15) for $\phi < 0.091$. Markers are as defined in figure I-1. Solid lines are the least-squares fits to present measurements: $\langle \overline{u}''^2 \rangle / \langle \overline{u} \rangle^2 = (-0.0019 \pm 0.017) + (0.60 \pm 0.04) C_D{}^{3/2}\sqrt{\phi}$, $R = 0.97, n = 21, 0.020 \leq \phi \leq 0.091$; $\langle \overline{u}''^2 \rangle / \langle \overline{u} \rangle^2 = (-0.055 \pm 0.064) + (0.28 \pm 0.02) C_D{}^{3/2}\sqrt{\phi}$, $R = 0.99, n = 5, \phi = 0.20$; $\langle \overline{u}''^2 \rangle / \langle \overline{u} \rangle^2 = (-0.64 \pm 0.07) + (0.27 \pm 0.02) C_D{}^{3/2}\sqrt{\phi}$, $R = 1.00, n = 5, \phi = 0.35, Re_d > 150$.

Appendix J

Operation of the laboratory flume and pump used in the laser-induced fluorescence experiments

All LIF measurements and a subset of the mean drag measurements were collected in a single recirculating Plexiglas flume. Figure J-1 is a schematic of the flume. The working section is a 284 cm-long, 40 cm-wide, and 43 cm-deep channel with a rectangular cross-section. The recirculating flow is driven by a pump that is connected to the two stilling basins via a pipe. A maximum volumetric flow rate of 60 GPM was achieved in a test run with no obstructions in the working section ($\left\langle \overline{H} \right\rangle = 15$ cm). The pump draws fluid from the downstream stilling basin. The pump outlet is connected to two pipes, of which one connects directly to the downstream setting basin and the other to the upstream basin. By adjusting the valves ($\times$) on the two pipes, the desired portion of the outflow from the pump can be diverted back to the downstream stilling basin. This setup allows the flow rate through the working section to be reduced without reducing the pump rate, which is convenient if very low flow rates are desired. Volumetric flow rates as low as 2.8 GPM were achieved in the LIF

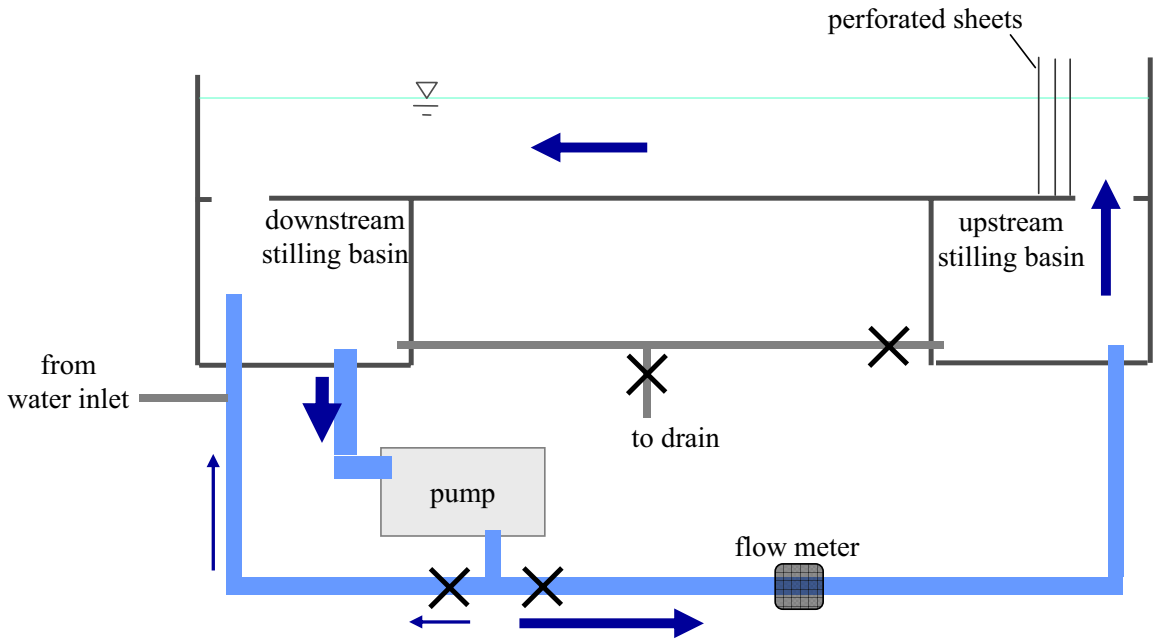

Figure J-1: The Plexiglas laboratory flume used in all LIF experiments and the mean drag experiments at $\phi \geq 0.15$. The valves ($\times$) can be adjusted independently. Arrows indicate the direction of flow. Not to scale.

experiments with this method. An in-line flow meter measures the volumetric flow rate of the flow entering the upstream stilling basin, which is exactly the flow rate through the working section of the flume. The flow enters the upstream stilling basin through a perforated manifold that extends across most of the width of the flume. This manifold helps create a uniform flow. Perforated aluminium sheets and coconut fiber may be positioned immediately downstream of the exit of the upstream stilling basin to further smoothen the flow before it enters the working section. At the downstream end, slots are also available to insert weirs or perforated sheets. In the present experiments, perforated sheets were inserted to prevent objects (e.g., dowels) from falling or being transported by the flow into the downstream stilling basin.

To operate the pump, turn on the power disconnect switch located immediately above the controller for the pump, then press the button labeled "FWD" on the controller for the pump. The rate of the pump is adjusted with the arrow-shaped buttons. To stop the pump, press the button labeled "STOP", then turn off the power disconnect. The screen will display "LOW VOLTAGE" briefly, then fade.

Water can be added or removed from the flume while the pump is operating.

It is not possible to access the inner walls of the stilling basins, and the flume is not equipped with an in-line filtration system. Consequently, particulate material should not be added to the flume if LIF experiments are planned. For example, it is not practical to alternate between particle image velocimetry, ADV, or LDV experiments and LIF experiments, because the removal of seeding material from the flume is very time-consuming (§ 3.3.2). Note also that the wooden dowels used to create the cylinder array release a lot of fine, opaque particles when they are first introduced in water. These particles interfere with both LDV and LIF measurements. It is recommended that the dowels be flushed with water before they are placed in the flume, where possible.

Bibliography

Acharya, R. C., Valocchi, A. J., Werth, C. J., and Willingham, T. W. (2007). Pore-scale simulation of dispersion and reaction along a transverse mixing zone in two-dimensional porous media. *Water Resour. Res.*, 43(10), doi:10.1029/2007WR005969.

Ayaz, F. and Pedley, T. J. (1999). Flow through and particle interception by an infinite array of closely-spaced circular cylinders. *Eur. J. Mech. B/Fluids*, 18(2):173 – 196.

Barrett, M. J. and Hollingsworth, D. K. (2001). On the calculation of length scales for turbulent heat transfer correlation. *Transactions of the ASME*, 123:878 – 883, doi:10.1115/1.1391277.

Bear, J. (1979). *Hydraulics of Groundwater*. McGraw-Hill Inc., New York.

Bennett, S. J. (2004). *Effects of emergent riparian vegetation on spatially averaged and turbulent flow within an experimental channel*, volume 8 of *Water Science and Application*, pages 29 – 41. American Geophysical Union, Washington, D.C.

Bertsekas, D. P. and Tsitsiklis, J. N. (2002). *Introduction to Probability*. Athena Scientific, Belmont, MA.

Bijeljic, B. and Blunt, M. J. (2007). Pore-scale modeling of transverse dispersion in porous media. *Water Resour. Res.*, 43(W12S11), doi:10.1029/2006WR005700.

Blevins, R. D. (2005). Forces on and stability of a cylinder in a wake. *J. Offshore Mech. Arct.*, 127:39 – 45, doi:10.1115/1.1854697.

Burattini, P., Lavoie, P., and Antonia, R. A. (2005). On the normalized turbulent energy dissipation rate. *Phys. Fluids*, 17:098103–1 – 098103–4, doi:10.1063/1.2055529.

Burke, R. W. and Stolzenbach, K. D. (1983). Free surface flow through salt marsh grass. MIT Sea Grant College Program Report MITSG 83-16, Massachusetts Institute of Technology, Cambridge.

Cornelisen, C. D. and Thomas, F. I. M. (2004). Ammonium and nitrate uptake by leaves of the seagrass *Thalassia testudinum*: impact of hydrodynamic regime and epiphyte cover on uptake roots. *J. Marine Syst.*, 49:177 – 194, doi:10.1016/j.jmarsys.2003.05.008.

Corrsin, S. (1974). Limitations of gradient transport models in random walks and in turbulence. *Adv. Geophys.*, 18A:25 – 60.

Davidson, M. J., Mylne, K. R., Jones, C. D., Phillips, J. C., Perkins, R. J., Fung, J. C. H., and Hunt, J. C. R. (1995). Plume dispersion through large groups of obstacles - a field investigation. *Atmos. Environ.*, 29(22):3245 – 3256.

Devore, J. L. (2000). *Probabilty and Statistics For Engineering and the Sciences*. Duxbury Thomson Learning, Pacific Grove, California, 5th edition.

Dullien, F. A. L. (1979). *Porous Media. Fluid Transport and Pore Structure*. Academic Press, Inc., New York.

Eckman, J. E. and Nowell, A. R. M. (1984). Boundary skin friction and sediment transport about an animal-tube mimic. *Sedimentology*, 31:851–862.

Ergun, S. (1952). Fluid flow through packed columns. *Chem. Eng. Prog.*, 48(2):89 – 94.

Finelli, C. M. (2000). Velocity and concentration distributions in turbulent odor plumes in the presence of vegetation mimics: a flume study. *Mar. Ecol. Prog. Ser.*, 207:297–309.

Finnigan, J. (2000). Turbulence in plant canopies. *Annu. Rev. Fluid Mech.*, 32:519–571.

Finnigan, J. J. (1985). Turbulent transport in flexible plant canopies. In Hutchison, B. A. and Hicks, B. B., editors, *The Forest-Atmosphere Interaction*, pages 443–480. D. Reidel Publishing Company, Dordrecht, Holland.

Fischer, H. B., List, E. J., Koh, R. C. Y., Imberger, J., and Brooks, N. H. (1979). *Mixing in Inland and Coastal Waters*. Academic Press, New York.

Fried, J. J. and Combarnous, M. A. (1971). Dispersion in porous media. In Chow, V. T., editor, *Advances in Hydroscience*, volume 7, pages 170 – 282. Academic Press, Inc., New York.

Furukawa, K., Wolanski, E., and Mueller, H. (1997). Currents and sediment transport in mangrove forests. *Estuar. Coast. Shelf. S.*, 44(3):301–310, doi:10.1006/ecss.1996.0120.

Gacia, E., Granata, T. C., and Duarte, C. M. (1999). An approach to measurement of particle flux and sediment retention within seagrass (*Posidonia oceanica*) meadows. *Aquat. Bot.*, 65:255 – 268.

Gerrard, J. H. (1978). The wakes of cylindrical bluff bodies at low Reynolds number. *Philos. Tr. R. Soc. S.-A*, 288:351–382.

Hackert, C. L., Ellzey, J. L., Ezekoye, O. A., and Hall, M. J. (1996). Transverse dispersion at high Peclet numbers in short porous media. *Exp. Fluids*, 21:286 – 290.

Hall, M. J. and Hiatt, J. P. (1996). Measurements of pore scale flows within and exiting ceramic foams. *Exp. Fluids*, 20:433 – 440.

Han, N.-W., Bhakta, J., and Carbonell, R. G. (1985). Longitudinal and lateral dispersion in packed beds: Effect of column length and particle size distribution. *AIChE J.*, 31(2):277 – 288.

Hey, D. L., Kenimer, A. L., and Barrett, K. R. (1994). Water quality improvement by four experimental wetlands. *Ecol. Eng.*, 3:381–397.

Hill, R. J. and Koch, D. L. (2002). Moderate-Reynolds-number flow in a wall-bounded porous medium. *J. Fluid Mech.*, 453:315–344, doi:10.1017/S002211200100684X.

Hill, R. J., Koch, D. L., and Ladd, A. J. (2001). Moderate-Reynolds-number flows in ordered and random arrays of spheres. *J. Fluid Mech.*, 448:243–278, doi:10.1017/S0022112001005936.

Hodges, K. C. and La Mer, V. K. (1948). Solvent effects on the quenching of the fluorescence of uranin by aniline. *J. Am. Chem. Soc.*, 70(2):722–726, doi:10.1021/ja01182a085.

James, C. S., Birkhead, A. L., Jordanova, A. A., and O'Sullivan, J. J. (2004). Flow resistance of emergent vegetation. *J. Hydraul. Res.*, 42(4):390 – 398.

Jolls, K. R. and Hanratty, T. J. (1966). Transition to turbulence for flow through a dumped bed of spheres. *Chem. Eng. Sci.*, 21:1185 – 1190.

Kadlec, R. H. (1994). Detention and mixing in free water wetlands. *Ecol. Eng.*, 3:345–380.

Kaimal, J. C. and Finnigan, J. J. (1994). *Atmospheric Boundary Layer Flows. Their Structure and Measurement*. Oxford University Press, Inc., New York.

Kececioglu, I. and Jiang, Y. X. (1994). Flow through porous media of packed spheres saturated with water. *J. Fluid Eng. - T. ASME*, 116(1):164 – 170.

Keefe, S. H., Barber, L. B., Runkel, R. L., Ryan, J. N., McKnight, D. M., and Wass, R. D. (2004). Conservative and reactive solute transport in constructed wetlands. *Water Resour. Res.*, 40:W01201, doi:10.1029/2003WR002130.

Kiya, M., Tamura, H., and Arie, M. (1980). Vortex shedding from a circular cylinder in moderate-Reynolds-number shear flow. *J. Fluid Mech.*, 141:721 – 735.

Knight, R. L., Kadlec, R. H., and Ohlendorf, H. M. (1999). The use of treatment wetlands for petroleum industry effluents. *Environ. Sci. Technol.*, 33(7):973 – 980.

Kobashi, D. and Mazda, Y. (2005). Tidal flow in riverine-type mangroves. *Wetl. Ecol. Manag.*, 13(6):615 – 619, doi:10.1007/s11273-004-3481-4.

Koch, D. L. and Brady, J. F. (1985). Dispersion in fixed beds. *J. Fluid Mech.*, 154:399–427.

Koch, D. L. and Brady, J. F. (1986). The effective diffusivity of fibrous media. *AIChE J.*, 32(4):575 – 591.

Koch, D. L., Hill, R. J., and Sangani, A. S. (1998). Brinkman screening and the covariance of the fluid velocity in fixed beds. *Phys. Fluids*, 10(12):3035 – 3037.

Koch, D. L. and Ladd, A. J. C. (1997). Moderate Reynolds number flows through periodic and random arrays of aligned cylinders. *J. Fluid Mech.*, 349:31–66.

Koch, E. W. (1994). Hydrodynamics, diffusion-boundary layers and photosynthesis of the seagrasses *Thalassia testudinum* and *Cymodocea nodosa*. *Mar. Biol.*, 118:767–776.

Kundu, P. K. and Cohen, I. M. (2004). *Fluid Mechanics*. Elsevier Academic Press, San Diego, CA, 3rd edition.

Lam, K., Li, J. Y., Chan, K. T., and So, R. M. C. (2003). Flow pattern and velocity field distribution of cross-flow around four cylinders in a square configuration at a low Reynolds number. *J. Fluid. Struct.*, 17:665 – 679.

Lee, J. K., Roig, L. C., Jenter, H. L., and Visser, H. M. (2004). Drag coefficients for modeling flow through emergent vegetation in the Florida Everglades. *Ecol. Eng.*, 22(4):237–248, doi:10.1016/j.ecoleng.2004.05.001.

Leonard, L. A. and Luther, M. E. (1995). Flow hydrodynamics in tidal marsh canopies. *Limnol. Oceanogr.*, 40(8):1474–1484.

Lienhard, J. H. (1966). Synopsis of lift, drag, and vortex frequency data for rigid circular cylinders. Bulletin 300, Washington State University, College of Engineering Research Division, Technical Extension Service, Washington.

Lightbody, A. F. (2007). *The Physical Role of Transverse Deep Zones in Improving Constructed Treatment Wetland Performance*. PhD thesis, Massachusetts Institute of Technology, Cambridge, MA.

Lightbody, A. F., Avener, M. E., and Nepf, H. M. (2008). Observations of short-circuiting flow paths within a free-surface wetland in Augusta, Georgia, U.S.A. *Limnol. Oceanogr.*, 53(3):1040–1053.

López, F. and García, M. (1998). Open-channel flow through simulated vegetation: Suspended sediment transport modeling. *Water Resour. Res.*, 34(9):2341 – 2352.

Maier, R. S., Kroll, D. M., Bernard, R. S., Howington, S. E., Peters, J. F., and Davis, H. T. (2000). Pore-scale simulation of dispersion. *Phys. Fluids*, 12(8):2065 – 2079.

Martinez, C. J. and Wise, W. R. (2003). Hydraulic analysis of Orlando Easterly Wetland. *J. Environ. Eng.*, 129(6):553–560, doi:10.1061/(ASCE)0733-9372(2003)129:6(553).

Masuoka, T. and Takatsu, Y. (1996). Turbulence model for flow through porous media. *Int. J. Heat Mass Tran.*, 39(13):2803 – 2809.

Mazda, Y., Wolanski, E., King, B., Sase, A., Ohtsuka, D., and Magi, M. (1997). Drag force due to vegetation in mangrove swamps. *Mangroves and Salt Marshes*, 1(3):193 – 199, doi:10.1023/A:1009949411068.

Meneghini, J. R., Saltara, F., Siqueira, C. L. R., and Ferrari Jr., J. A. (2001). Numerical simulation of flow interference between two circular cylinders in tandem and side-by-side arrangements. *J. Fluid. Struct.*, 15:327 – 350, doi:10.1006/jfls.2000.0343.

Mickley, H. S., Smith, K. A., and Korchak, E. I. (1965). Fluid flow in packed beds. *Chem. Eng. Sci.*, 20:237 – 246.

Nakajyo, S., Shigematsu, T., Takehara, K., and Tsujimoto, G. (2007). Turbulence measurements inside and around porous media using a PTV technique. In Di Silvio, G. and Lanzoni, S., editors, *Proceedings of the 32nd Congress of IAHR.*

Nepf, H. M. (1999). Drag, turbulence, and diffusion in flow through emergent vegetation. *Water Resour. Res.*, 35(2):479–489.

Nepf, H. M., Sullivan, J. A., and Zavistoski, R. A. (1997). A model for diffusion within emergent vegetation. *Limnol. Oceanogr.*, 42(8):1735–1745.

Neumeier, U. and Amos, C. L. (2006). The influence of vegetation on turbulence and flow velocities in European salt-marshes. *Sedimentology*, 53:259 – 277, doi:10.1111/j.1365-3091.2006.00772.x.

Neumeier, U. and Ciavola, P. (2004). Flow resistance and associated sedimentary processes in a *Spartina maritima* salt-marsh. *J. Coastal Res.*, 20(2):435–447.

Nikora, V. I. (2000). Comment on "Drag, turbulence, and diffusion in flow through emergent vegetation" by H. M. Nepf. *Water Resour. Res.*, 36(7):1985–1986.

Ohmoto, T. and Tanaka, T. (2007). Interaction between free surface oscillation and velocity fluctuations in open-channel flow with vegetation zone. In Di Silvio, G. and Lanzoni, S., editors, *Proceedings of the 32nd Congress of IAHR.*

Pearson, B. R., Krogstad, P.-A., and van de Water, W. (2002). Measurements of the turbulent energy dissipation rate. *Phys. Fluids*, 14(3):1288 – 1290, doi:10.1063/1.1445422.

Pereira, J. C. F., Malico, I., Hayashi, T. C., and Raposo, J. (2005). Experimental and numerical characterization of the transverse dispersion at the exit of a short ceramic foam inside a pipe. *Int. J. Heat Mass Tran.*, 48:1 – 14, doi:10.1016/j.ijheatmasstransfer.2004.08.001.

Peterson, G. W. and Turner, R. E. (1994). The value of salt marsh edge vs interior as a habitat for fish and decapod crustaceans in a Louisiana tidal marsh. *Estuaries*, 17(1B):235–262.

Petrasek, Z. and Schwille, P. (2008). Precise measurement of diffusion coefficients using scanning fluorescence correlation spectroscopy. *Biophys. J.*, 94:1437–1448.

Petryk, S. (1969). *Drag on cylinders in open channel flow.* PhD thesis, Colorado State University, Fort Collins, Colorado.

Pluntke, T. and Kozerski, H.-P. (2003). Particle trapping on leaves and on the bottom in simulated submerged plant stands. *Hydrobiologia*, 506-509:575–581.

Poggi, D., Katul, G. G., and Albertson, J. D. (2004). A note on the contribution of dispersive fluxes to momentum transfer within canopies. *Bound. Lay. Meteorol.*, 111(3):615 – 621, doi:10.1023/B:BOUN.0000016563.76874.47.

Rani, S. A., Pitts, B., and Stewart, P. S. (2005). Rapid diffusion of fluorescent tracers into *Staphylococcus epidermidis* biofilms visualized by time lapse microscopy. *Antimicrob. Agents Ch.*, 49(2):728–732, doi:10.1128/AAC.49.2.728-732.2005.

Raupach, M. R., Antonia, R. A., and Rajagopalan, S. (1991). Rough-wall turbulent boundary layers. *Appl. Mech. Rev.*, 44(1):1 – 25.

Raupach, M. R. and Shaw, R. H. (1982). Averaging procedures for flow within vegetation canopies. *Bound. Lay. Meteorol.*, 22:79 – 90.

Schwarzenbach, R. P., Gschwend, P. M., and Imboden, D. M. (2003). *Environmental Organic Chemistry.* John Wiley & Sons, Inc., Hoboken, NJ, 2nd edition.

Serra, T., Fernando, H. J. S., and Rodriguez, R. V. (2004). Effects of emergent vegetation on lateral diffusion in wetlands. *Water Res.*, 38(1):139 – 147, doi:10.1016/j.watres.2003.09.009.

Shavit, U. and Brandon, T. (2001). Dispersion within emergent vegetation using PIV and concentration measurements. In *Proceedings of the 4th International Symposium on Particle Image Velocimetry.*

Shi, Z., Hamilton, L. J., and Wolanski, E. (2000). Near-bed currents and suspended sediment transport in saltmarsh canopies. *J. Coastal Res.*, 16(3):909–914.

Soleymani, A., Turunen, I., Yousefi, H., and Bastani, D. (2007). Numerical investigations of fluid flow and lateral fluid dispersion in bounded granular beds in a cylindrical coordinates system. *Chem. Eng. Technol.*, 30(10):1369 – 1375.

Spielman, L. and Goren, S. L. (1968). Model for predicting pressure drop and filtration efficiency in fibrous media. *Envir. Sci. Tech.*, 2(4):279 – 287.

Stapf, S., Packer, K. J., Graham, R. G., Thovert, J.-F., and Adler, P. M. (1998). Spatial correlations and dispersion for fluid transport through packed glass beads studied by pulsed field-gradient NMR. *Phys. Rev. E*, 58(5):6206 – 6221.

Stone, B. M. and Shen, H. T. (2002). Hydraulic resistance of flow in channels with cylindrical roughness. *J. Hydraul. Eng.*, 128(5):500 – 506, doi:10.1061/(ASCE)0733-9429(2002)128:5(500).

Stumpf, R. P. (1983). The process of sedimentation on the surface of a salt marsh. *Estuar. Coast. Shelf S.*, 17:495–508.

Sullivan, J. A. (1996). Effects of Marsh Grass on Diffusivity. Master's thesis, Massachusetts Institute of Technology, Cambridge, MA.

Tanino, Y. and Nepf, H. M. (2007). Experimental investigation of lateral dispersion in aquatic canopies. In Di Silvio, G. and Lanzoni, S., editors, *Proceedings of the 32nd Congress of IAHR.*

Tanino, Y. and Nepf, H. M. (2008a). Laboratory investigation of lateral dispersion within dense arrays of randomly distributed cylinders at transitional Reynolds number. *Phys. Fluids*, submitted.

Tanino, Y. and Nepf, H. M. (2008b). Laboratory investigation of mean drag in a random array of rigid, emergent cylinders. *J. Hydraul. Eng.*, 134(1):34–41, doi:10.1061/(ASCE)0733-9429(2008)134:1(34).

Tanino, Y. and Nepf, H. M. (2008c). Lateral dispersion in random cylinder arrays at high Reynolds number. *J. Fluid Mech.*, 600:339 – 371, doi:10.1017/S0022112008000505.

Tanino, Y., Nepf, H. M., and Kulis, P. S. (2005). Gravity currents in aquatic canopies. *Water Resour. Res.*, 41:W12402, doi:10.1029/2005WR004216.

Taylor, G. I. (1922). Diffusion by continuous movements. *Proc. London Math. Soc.*, s2-20(1):196 – 212, doi:10.1112/plms/s2-20.1.196.

Taylor, J. R. (1997). *An Introduction to Error Analysis. The study of uncertainties in physical mesurements.* University Science Books, Sausalito, California, 2nd edition.

Tennekes, H. and Lumley, J. L. (1972). *A First Course in Turbulence.* The MIT Press, Cambridge, MA.

Thomas, F. I. M., Cornelisen, C. D., and Zande, J. M. (2000). Effects of water velocity and canopy morphology on ammonium uptake by seagrass communities. *Ecology*, 81(10):2704 – 2713.

Tsujimoto, T., Shimizu, Y., Kitamura, T., and Okada, T. (1992). Turbulent open-channel flow over bed covered by rigid vegetation. *J. Hydrosci. Hydraul. Eng.*, 10(2):13 – 25.

Tummers, M. J. and Passchier, D. M. (2001). Spectral analysis of biased LDA data. *Meas. Sci. Technol.*, 12:1641 – 1650, doi:10.1088/0957-0233/12/10/304.

Valiela, I., Teal, J. M., and Deuser, W. G. (1978). The nature of growth forms in the salt marsh grass *Spartina alterniflora*. *Am. Nat.*, 112(985):461–470.

White, B. L. (2002). Transport in random cylinder arrays: A model for aquatic canopies. Master's thesis, Massachusetts Institute of Technology, Cambridge, MA.

White, B. L. (2006). *Momentum and Mass Transport by Coherent Structures in a Shallow Vegetated Shear Flow*. PhD thesis, Massachusetts Institute of Technology, Cambridge, MA.

White, B. L. and Nepf, H. M. (2003). Scalar transport in random cylinder arrays at moderate Reynolds number. *J. Fluid Mech.*, 487:43–79, doi:10.1017/S0022112003004579.

White, F. M. (1991). *Viscous Fluid Flow*. McGraw-Hill, New York, 2nd edition.

Williamson, C. H. K. (1985). Evolution of a single wake behind a pair of bluff bodies. *J. Fluid Mech.*, 159:1–18.

Wu, F.-C., Shen, H. W., and Chou, Y.-J. (1999). Variation of roughness coefficients for unsubmerged and submerged vegetation. *J. Hydraul. Eng.*, 125(9):934 – 942.

Yevseyev, A. R., Nakoryakov, V. E., and Romanov, N. N. (1991). Experimental investigation of a turbulent filtration flow. *Int. J. Multiphase Flow*, 17(1):103–118.

Zavistoski, R. A. (1994). Hydrodynamic effects of surface piercing plants. Master's thesis, Massachusetts Institute of Technology, Cambridge, MA.

Zdravkovich, M. M. and Pridden, D. L. (1977). Interference between two circular cylinders; series of unexpected discontinuities. *J. Ind. Aerodynam.*, 2:255 – 270.

Zhang, H. J. and Zhou, Y. (2001). Effect of unequal cylinder spacing on vortex streets behind three side-by-side cylinders. *Phys. Fluids*, 13(12):3675 – 3686, doi:10.1063/1.1412245.